Developing and Using Atomic Force Microscopy to Investigate Mechanisms of Tumour Metastasis

by

Jacob George Albon

A thesis presented for the degree of

Doctor of Philosophy

Department of Physics and Astronomy

University of Sheffield

Declaration

The work described in this thesis was undertaken at the University of Sheffield between October 2010 and September 2014 under the supervision of Prof. Jamie Hobbs and Prof. Nicola Brown. Unless stated, it is the work of the author and has not been submitted in whole or part for any other degree at this or any other institute.

Signed:

Jacob George Albon

September 2014

Abstract

Mortality in breast cancer is increasingly linked to metastasis to bone, which is currently incurable and the mechanisms involved in this process are not fully understood. By using atomic force microscopy to extract the mechanical and adhesive properties of metastatic breast cancer cells under near physiological conditions the aim of the work presented in this thesis is to develop the methods used to extract these properties as well as enhance understanding of tumour metastasis.

The biomechanical properties of three human breast cell lines with varying metastatic potential have been investigated through atomic force microscopy based indentation, using three separate analytical models. The indentation studies were used to reveal mechanical properties of living cells which can be attributed to cellular structures such as the cytoskeleton, cell membrane, cytoplasm and numerous intracellular organelles. This is the first study to compare three contact mechanical models on these cells. The results demonstrate that benign MCF-10A breast cells are less deformable than the invasive MCF-7 and metastatic MDA-MB-231 breast cancer cell lines. Force maps have also revealed elastic heterogeneity across the cell surface of all three cell lines which appears to correlate with intracellular structures. The results demonstrate that whole cell mapping has the potential to investigate cell mechanics using a variety of approaches.

The biomechanical properties of sub-populations of the MDA-MB-231 cell line were also investigated. Sub-populations of cancer cells which were shown to display 'stem-cell-like' properties and 'normal' cancer cells which did not were identified using a number of *in vitro* techniques and selected for AFM indentation experiments via fluorescence microscopy. The results indicated no significant difference between the measured mechanical properties of the 'stem-like' and 'normal' cancer cells.

Adhesive interactions between metastatic MDA-MB-231 cells and 'osteoblast-like' Saos-2 cells were then characterised using an AFM based single cell force spectroscopy (SCFS) protocol. The detachment force required to separate the two cell types was measured for untreated, zoledronic acid treated and anti-N-cadherin treated cells. The results showed that both treatments significantly reduced the detachment force. This result is important in understanding the mechanisms by which adjuvant zoledronic acid therapy may reduce bone resorption and metastases in patients with advanced breast cancer.

Acknowledgements

This thesis would have not been possible without the help, support and encouragement of many people who I would like to thank here.

Firstly I would like to thank my two supervisors Jamie Hobbs and Nicola Brown. They have been very supportive throughout and have helped guide me through this work. The faith that Jamie showed in me in offering me this PhD position over four years ago has been a constant source of motivation throughout this work. At the start of this work I had a very steep learning curve in terms of the biological content of the project and I would like to thank Nicola for her support and guidance with this aspect of the work. I would also like to thank her partner Gerald Meininger for his advice and lengthy discussions on biological applications of AFM which have helped me over the years.

I would like to thank everybody that has worked with me in the physics department over the last four years particularly: Nic Mullin, Rik Bailey, Ross Carter, Nusrat Rafiq, Elisa Laera, Paul Chapman, Johnny Burns, Stephen Jackson, Lamiaa Alharbe, Ana Morales and Amy Hall. I would particularly like to thank Nic Mullin for his continued support. His technical knowledge of AFM is outstanding and discussions with Nic have helped me solve many of the problems I have faced over the last five years.

I would also like to thank everybody I have worked with in the Microcirculation

Research Group in Oncology over the last four years: Kim Reeves, Sapna Lunj, Jack Hurrell, Gemma Foulds and the many technical support staff who order all the consumables and keep the labs running of which there are too many to mention. I would particularly like to thank Kim Reeves for training me in all areas of tissue culture and providing constant support throughout the last four years. I would like to thank Sue Newton and Kay Hopkinson for their technical support with the Flow cytometry work presented in this thesis and I would also like to thank all the staff in the physics workshop who helped me develop parts of the AFM, in particular Paul and Simon for their help constructing the acoustic isolation chamber for the AFM and the base plate for the extended Z-stage used for my adhesion experiments.

I would like to thank my family for their continued support throughout the last four years. I am particularly grateful for the support my parents, Sue and George, have given me financially and emotionally during the last four years and I couldn't have done any of this without them. I would also like to thank my girlfriend Anneka for her continued support throughout. I could not have managed the last four years without her.

I would also like to thank EPSRC for funding my PhD and the Institute of Physics and Department of Medicine Dentistry and Health at The University of Sheffield for funding towards travel to conferences.

Contents

Chapter 1

Overview

1.1 Aims and Objectives

The main aims of this thesis were to develop existing AFM procedures to investigate mechanisms of breast cancer metastasis. Initially this meant developing indentation type AFM techniques and analysis to characterise a range of breast cell lines of varying malignancies to try to understand the biomechanical changes cancer cells undergo as their malignancy increases. It was hoped that a correlation in mechanical properties with biological data would prove to be a method for identifying more aggressive cancer cells from benign cells. Mechanical mapping of entire cell surfaces was to be performed initially to assess whether any mechanical heterogeneity existed over the surface of living cells to determine what method would be used to characterise the different breast cell lines.

The second objective of this work was to develop an experimental setup in which the adhesive interactions between two different cells could be quantified using AFM. A form of single cell force spectroscopy (SCFS) was to be developed along with an experimental protocol and methods of analysis to investigate the

mechanical contact between two different cell types. Specifically the interaction between metastatic breast cancer cells and cells known to interact with these cancerous cells at the site of a secondary tumour were to be investigated to gain an insight into the cellular signalling involved in metastasis.

1.2 Thesis Outline

Chapter 2 of this thesis is an introduction to cancer and covers a description of the process of carcinogenesis and highlights a number of areas in cancer progression which are currently under intense biological research before going into more detail about the metastatic step in the pathogenesis of cancer. Breast cancer is then introduced and the topic of metastasis relating to this specific form of cancer is discussed before an overview of atomic force microscopy (AFM) and a description of the different modes of this form of scanning probe microscopy which were to be used and developed throughout this work. A third section of this chapter reviews the use of AFM for biological applications, in particular mechanical measurements on living cells and the contact models used to extract mechanical properties from the data.

Chapter 3 is a chapter describing the main experimental methods involved in this work from the description of the breast cell lines used and how the cells were cultured to how the mechanical contact models were implemented to analyse the AFM indentation data using the AFM software as well as the development of techniques to image living cells in liquid using the AFM imaging modes.

Chapter 4 covers the development of force mapping routines and indentation experiments used to characterise the mechanical properties of three different breast cell lines and highlights the development of force mapping in conjunction with

fluorescence microscopy to understand what the characterisation information is revealing.

Chapter 5 involves the biological characterisation of 'stem-like' breast cancer cells using a number of *in vitro* biological assays and the combination of these protocols with the AFM experimental and analytical procedures developed in chapter 4 to compare the mechanical properties of 'stem-like' breast cancer cells with 'normal' breast cancer cells.

Chapter 6 covers the development of a SCFS routine using AFM which is then used to investigate adhesion interactions between metastatic breast cancer cells and cells known to be involved in the tumour micro-environment at the site of metastases in bone.

Chapter 7 then discusses and concludes the experimental procedures developed and the findings from each of the experimental chapters described in this outline and highlights future work in this specific field of biological physics.

Chapter 2

Introduction

2.1 Introduction to Cancer

Cancer affects almost all multicellular organisms on this planet and has been known to man since its earliest recordings dating back to ancient Egyptian times[1]. The oldest recorded description of cancer is found in the Edwin Smith Papyrus which was written in approximately 3000 BC. It is, however, the discovery by German microscopist Johannes Müller, in 1836, which laid the foundations for the modern classification of cancer, diagnosis, therapy and cancer research. He recognized the cellular nature of various morbid growths with the aid of a microscope. He also stated that cancer is cellular and that the cellular form resembles that of the tissues from which the cancerous growth springs [2].

2.1.1 The Hallmarks of Cancer

Cancer is the name for a group of diseases in which cells proliferate uncontrollably. The process of carcinogenesis is very complex and has been defined using a number of hallmarks or specific traits that are capabilities acquired by cells dur-

ing their transition from normal to tumourigenic and eventually malignant cells [3], see figure 2.1. One of these hallmarks is the ability of cancer cells to sustain proliferative signalling. This arises from an initial genetic instability. Oncogenes are genes which gain function when mutated, whereas tumour suppressor genes lose function when mutated. A mutation in either of these two types of gene can be the initial step in the generation of a cancer cell, by affecting the regulatory mechanisms that control the delicate balance between cell proliferation and apoptosis (programmed cell death) [4]. Further genetic mutations allow cells to evade growth suppressors and proliferate uncontrollably [5], which is by definition, a tumour. Normal cells grow and divide a limited number of times before there becomes a point at which they are unable to proliferate further, with the exception of stem cells. The cells then reach an irreversible state known as senescence where the cells remain viable but are unable to proliferate further. Another hallmark of cancer cells is their ability to somehow escape this senescence and are able to continually proliferate [6]. A tumour is benign if there is no spread, only local growth occurs and it does not have morphological features of in-situ disease. In-situ tumours that develop in the epithelium have the abnormal morphological appearance of cancer, but are non-invasive at that time. Cancerous tumours are malignant tumours that develop in the epithelium that have the ability to invade and destroy their underlying mesenchyme; the collective term for the supporting tissues beneath the basement membrane.

Normal tissue homeostasis can be ensured via contact inhibition [7]. This is where the contact between cells in a densely populated area suppresses further cell proliferation. This suppression is removed in tumour cells by loss of cell adhesion molecules such as E-cadherin allowing the tumour cells to escape their initial environment [8, 9]. The tumour suppressor gene TGF-β is known for its

anti-proliferative properties, but these are evaded by cancer cells once contact inhibition is lost. The cells are then able to migrate through their surrounding tissue. TGF-β is believed to be involved in a process known as epithelial to mesenchymal transition (EMT) which is an important process in cell development but is also thought to be involved in the pathogenesis of cancer and promotes tumour malignancy [10]. The process of EMT is thought to involve a number of factors which influence the morphology and invasive capabilities of the tumour cells. One of these factors is the gain of N-cadherin expression, which is an adhesion receptor known for its role in mesenchymal cell migration [11].

As the malignant tumour proliferates, cells towards the centre become starved of oxygen and begin to die (hypoxia) [12]. These necrotic cells release pro-inflammatory signals which can recruit cells from the immune system. The cells must adapt in order to support their metabolic needs and survive and so signals from the cancer cells or immune cells stimulate the growth of blood vessels from the host vascular network into the developing tumour mass, which allows further proliferation and growth of the primary tumour. This process is known as angiogenesis [13]. The role of recruited immune cells and normal tissue in the process of carcinogenesis is a relatively new area of research. As these cells are not thought to be cancerous themselves, when referring to specific sites during the progression of a cancer the term 'tumour micro-environment' is often phrased. Once the primary tumour is established some tumour cells gain the ability to disseminate from the primary tumour via the blood vessels or the lymphatics and form secondary tumours in a distant site in a process known as metastasis. This is yet another hallmark of cancer along with all the other traits that have been described in this brief introduction into the complexity of the pathogenesis of cancer [3]. By highlighting these hallmarks it makes it easier to see the diverse range of research

Figure 2.1: This image depicts ten hallmark capabilities of cancer [3]. These hallmarks highlight areas of active research into the mechanisms behind each stage of the pathogenesis of cancer.

areas that are needed to understand the process of carcinogenesis. Each stage or hallmark described here represents a very active area of research into the complexity of cancer. The main area focused upon in this thesis is cancer metastasis, in particular breast cancer metastasis.

2.1.2 Metastasis

Metastasis was thought to be a late event in carcinogenesis and is inefficient in that most cells are destroyed before reaching a secondary site [14]. There is however recent evidence to suggest that metastasis may occur much earlier in the development of a cancer than expected and could possibly occur after only a few epithelial genetic alterations [15]. It is estimated that on average more than 10^6 tumour cells per gram of tumour intravasate into the circulation daily [16, 17] with only a minute fraction of these believed to possess the ability to form secondary tumours. The cells that survive the metastatic cascade must have acquired specific traits which allow them to migrate initially from the primary tumour, invade and survive in the blood and lymphatic vessels [18] and recent metabolic studies have also shown that mitochondrial function may play an important role in metastasis [19]. Intravasation is the process by which the tumour cells invade and penetrate the blood/lymphatic vessels. They achieve this by digesting the membrane with proteases [20]. For metastasis to occur, cell-cell interactions must be modulated. Alterations, through the EMT process, to the expression of cell adhesion molecules (CAMs) that bind cells together allow cells to escape from the primary tumour. Cadherins are a sub-group of CAMs which hold epithelial cells together and as previously mentioned the expression of E-cadherin is often lost in the development of epithelial cancers [3]. Cells that have intravasated into the circulation can then travel along the blood/lymphatic vessels to other parts

of the body where they are able to attach to the endothelium at specific sites and escape the vessels by the dissolution of the membrane (extravasation). Metastases have been shown to spread to specific sites [21], which supports the 'seed and soil' theory proposed by Paget [22] in which it is thought that to have the ability to establish a secondary tumour at a distant site, the tumour cells need to be 'suited' to the micro-environment at that secondary site for a metastasis to be formed. Cell adhesion molecules play an important role in why cells metastasise to the sites that they do whilst the local properties of the endothelial cells such as function and extracellular matrix composition also help determine the specific sites of metastasis [23]. Once a circulating tumour cell has extravasated into a distant site these metastatic cells can then migrate within the secondary site and grow. They can, however, also lie dormant, undetected for years before they form secondary tumours [21] as depicted in figure 2.2. Why this happens it is not fully understood but it is thought to be due to the tumour cell's ability to interact with its tumour micro-environment and establish the specific factors it requires for growth and further invasiveness at that site. Once secondary tumours have established themselves they are very difficult to treat and are a significant cause of morbidity in cancer. In fact tumour metastasis is the leading cause of cancer death [24]. An increased understanding of the biological and mechanical processes involved in cancer metastasis can only be positive as we try to understand this process and develop prognostic and therapeutic regimes to stop metastasis.

2.1.3 Breast Cancer

Breast cancer is the most common form of cancer in the UK and is the second biggest cause of cancer death in women. There are almost 50,000 cases of breast cancer diagnosed in the UK each year with the disease claiming around 12,000 lives

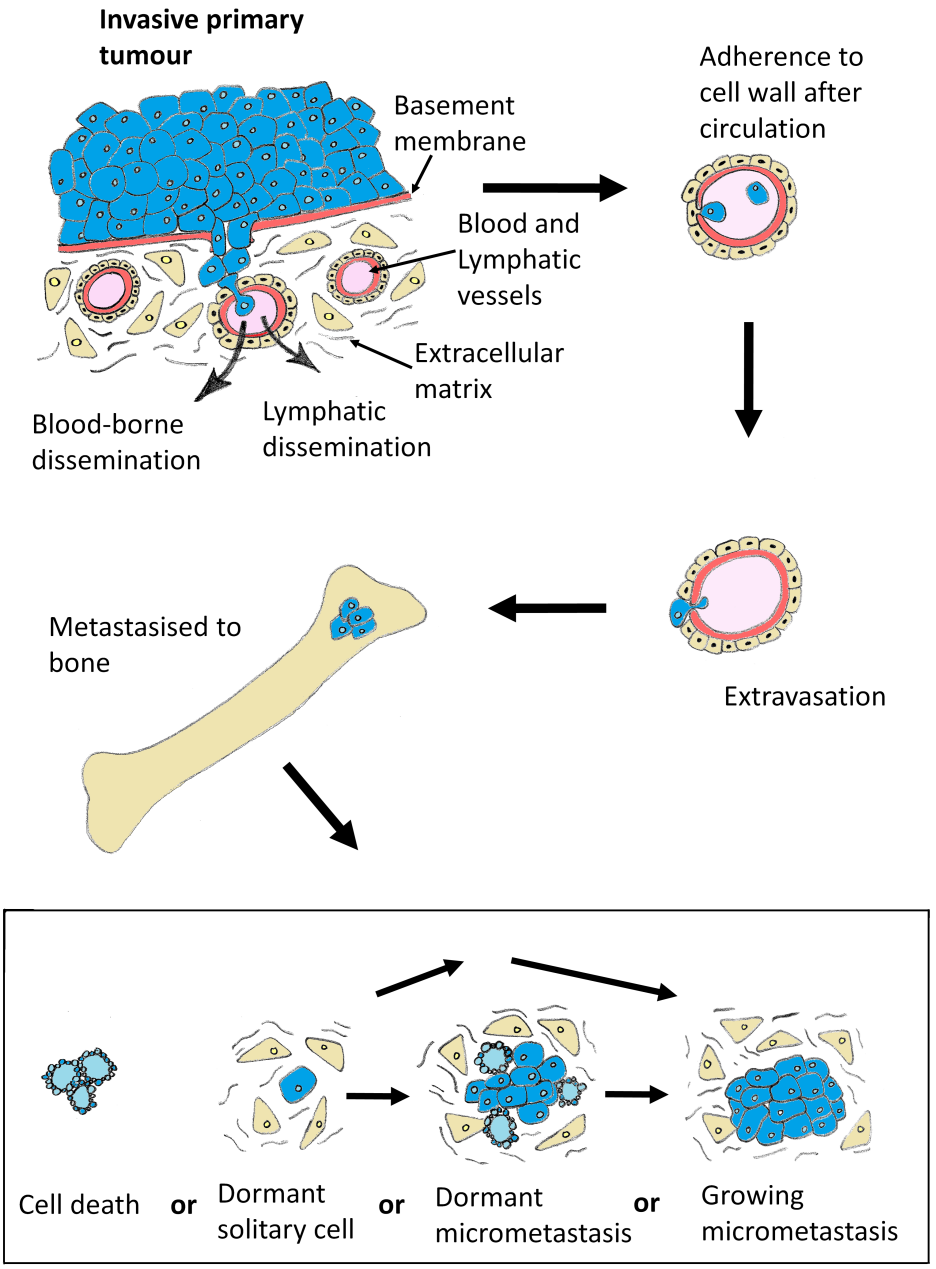

Figure 2.2: A schematic illustration depicting the process of metastasis from initial dissemination into the vasculature to the colonisation of distant sites.

annually [25]. The current lifetime risk of developing breast cancer is one in every eight women [26]. Breast cancers are epithelial cancers derived most commonly from the milk ducts or lobules supplying them in the breast.

Due to more effective methods used in screening and cancer detection (MRI etc) and improvements in treatments, survival rates for women with breast cancer are constantly improving. Women diagnosed with breast cancer are now twice as likely to survive their disease for at least ten years, than those diagnosed forty years ago (CR UK). Breast cancer survival rates are, however, better the earlier the cancer is diagnosed (CR UK) as there is decreased metastatic spread. Once the cancer has metastasised to secondary sites it is increasingly difficult to cure the disease. Breast cancer predominantly metastasises to bone and is the cause of significant morbidity and mortality. In the case of breast cancers, 65% - 75% of patients at autopsy with advanced breast cancer show signs of bone metastasis [27, 28]. Improved strategies to inhibit the growth of metastases are therefore a logical approach for cancer prevention and treatment.

Although many things govern the process of metastasis, one area which requires further investigation is the extravasation and intravasation of tumour cells which is regulated in part by cell adhesion mechanisms. One approach is to investigate the adhesion molecules and crosstalk between the metastatic cells and extracellular matrix (ECM), at the secondary site, involved in the attachment of the cell to the vasculature. Cadherins are a family of CAMs and as previously mentioned ensure cells are bound together. Another family of CAMs are Integrins. They are receptors that mediate the adhesion between the tumour cell and the ECM. They are expressed on both the tumour cell and the ECM and form adhesions between the two with their corresponding ligands [29, 23]. One integrin that is critical in the metastasis of breast cancer cells to bone is $\alpha v\beta 3$. Over-expression of $\alpha v\beta 3$

leads to increased tumour cell adhesion, migration and invasion to bone [29]. The immunoglobulin super family of cell adhesion molecules (IgSF CAMs) are also a family of CAMs. Two such examples of these are CD24 and CD44 which have been used as prospective cancer stem cell markers [30].

The aims of this work were to investigate the mechanisms of breast cancer metastasis using atomic force microscopy (AFM). This was to be approached in a number of ways. The first method was to characterise the mechanical properties of metastatic breast cancer cells to see how they differed from non-metastatic cells as it was hypothesised that to intravasate and extravasate these metastatic cells must have favourable mechanical properties to allow them to undergo these processes. The second important area of breast cancer metastasis which was to be investigated in this work was the interaction between breast cancer cells and the tumour micro-environment at a secondary site, which is predominantly bone as mentioned earlier in this section. This was to be done via single cell force spectroscopy using AFM.

2.2 Atomic Force Microscopy

The atomic force microscope (AFM) is a member of the family of scanning probe microscopes and was invented by Binnig et al. in the mid 1980s [31]. It was a development of the scanning tunnelling microscope (STM) and allowed topographical imaging of both conducting and insulating surfaces with near atomic resolution.

2.2.1 Contact Mode AFM

As with all SPMs the AFM has two fundamental components, the probe and the scanner. The probe for an AFM is a sharp tip at the free end of a cantilever, which is usually made from silicon. The scanner is made from a piezoelectric ceramic. This allows precise control over the tip since the piezoelectric material deforms when a voltage is applied. The voltage is proportional to the deformation of the piezoelectric material which is designed to allow full control over the position of the tip and the distance between the tip and surface. When the probe is brought very close to the surface of the sample which is being investigated, interactions between the sample and the tip occur. The magnitude of these interactions is directly linked to the distance between the tip and the sample surface. These interactions cause the cantilever to bend and a laser and position sensitive photodiode are used to detect the cantilever deflection as shown in figure 2.3. Whilst raster scanning across the surface of a sample the force between the tip and sample is held constant by a feedback loop which controls the height of the z-piezo. The height position of the z-piezo is then plotted to produce a topographic image of the sample. The speed of the scanning is limited by the response time of the feedback loop which is controlled by high and low frequency gains. If gains are set too high the cantilever can go into feedback oscillation. The measured deflection of the cantilever corresponds to the magnitude of the interaction between the tip and the surface which corresponds to a specific signal. This signal is known as the detector signal. A reference value is established to give the detector signal meaning. This reference value is called the deflection setpoint. When the probe is scanned across the surface of the sample being investigated the scanner follows a precise raster pattern. The probe tracks the surface of the sample and in doing so changes the detector signal corresponding to the tip-surface distance. The difference between

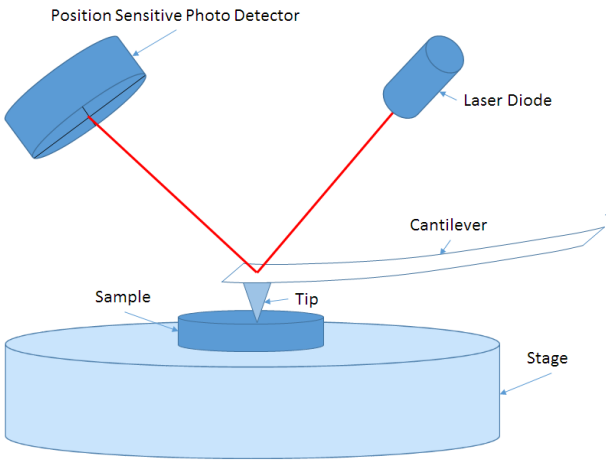

Figure 2.3: Schematic diagram of a typical AFM setup.

the detector signal and the deflection setpoint is the error signal. The Z feedback loop constantly compares the setpoint and the detector signal during scanning. If they are not equal it moves the scanner either closer to or further away from the sample by changing the voltage applied to the piezoelectric material. Although this feedback allows high precision scanning of irregular surfaces, it increases the time it takes to scan the sample [32].

2.2.2 Intermittent Contact Mode AFM

Two of the main operating modes of AFM are contact and intermittent contact mode. In intermittent contact mode the cantilever is oscillated just below its resonant frequency. When the oscillating cantilever is brought near the sample surface the interaction with the sample causes the amplitude of the oscillating cantilever to decrease. To control the interaction of the tip with the sample a feedback loop is used, similar to contact mode, but in this instance it is used to maintain a constant oscillation amplitude. As the sample is raster scanned with the oscillating tip the z-piezo moves up and down using this feedback loop maintaining

a constant cantilever amplitude, known as the amplitude setpoint. The position of the z-piezo is again used to produce a topographic image of the sample. The amplitude setpoint is typically adjusted so that the tip of the cantilever is just in contact with the sample being investigated at the end of its oscillation. The amplitude setpoint minus the actual measured amplitude produces an error signal. The error signal is then sent to a controller which produces a signal to correct the z-piezo position to regain the desired oscillation amplitude. Gain controls are again used to control the frequency of this feedback loop. The main advantage of using intermittent contact mode compared with contact mode is that it reduces the damage to the sample as the intermittent contact reduces the lateral forces applied to the sample during imaging and sufficient oscillation amplitudes also prevent the tip from being trapped by adhesive meniscus forces. Intermittent contact mode can also be used in conjunction with phase imaging in which the phase difference between the drive signal oscillating the cantilever and the output signal from the oscillating cantilever is monitored. Variations in this phase can give qualitative information about the viscoelastic properties of a sample as well as adhesive and frictional properties. For quantitative measurements of a samples mechanical properties force spectroscopy is commonly used.

2.2.3 Force Measurements

Beyond the two general contact and intermittent contact modes for imaging samples the AFM can be used to extract quantitative data from the indentation of a sample. It can do this by taking force measurements of a sample. In a force measurement the sample is brought into contact with the cantilever tip or a microsphere attached to a cantilever. In some AFM setups the holder in which the cantilever is fixed is moved by a piezoelectric translator, alternatively the stage

on which the sample is attached is moved by the piezoelectric translator. The force measurement description is unchanged for either setup. The cantilever deflection is monitored as the tip and sample are brought into contact. The resulting data gives the cantilever deflection versus the position of the z-piezo normal to the sample surface. To obtain force versus distance information from the force measurement data the spring constant of the cantilever must be known. This is done by calibrating the cantilever.

Firstly the deflection sensitivity of the cantilever is calculated by indenting an incompressible surface such as a glass slide or mica. This is to measure the voltage response of the position sensitive photo diode as a function of z scanner displacement. If we know the spring constant of the cantilever in question it is

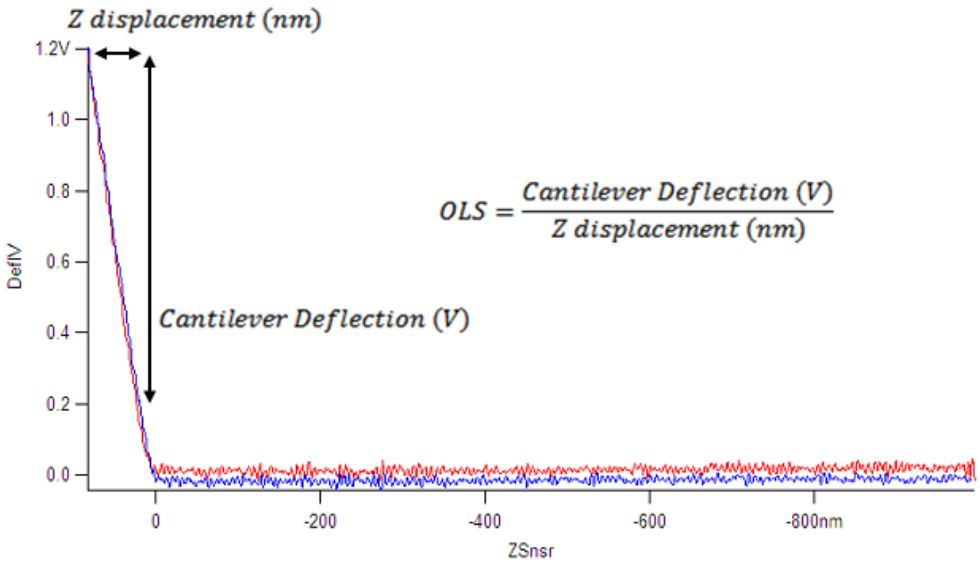

Figure 2.4: Force curve taken on a relatively hard surface showing the region on which the optical lever sensitivity is calculated.

possible to calculate the force being applied to the sample and therefore infer mechanical properties of the sample from such force-distance data. The most common method in calibrating a cantilever to calculate its spring constant is by

the thermal noise method [33]. For this method the cantilever is treated as a simple harmonic oscillator in equilibrium which can be described by the Hamiltonian:

$$H = \frac{p^2}{2m} + \frac{1}{2}m\omega_0^2 x^2, \tag{2.1}$$

where m is the mass of the oscillator, p it's momentum, ω_0 is the resonant angular frequency and x is the vertical displacement of the oscillator. By the equipartition theorem each quadratic term in the Hamiltonian has the average value of $\frac{1}{2}k_B T$ where k_B is Boltzmann's constant and T is absolute temperature. Therefore:

$$< \frac{1}{2}m\omega_0^2 x^2 >= \frac{1}{2}k_B T. \tag{2.2}$$

By substituting $\omega_0^2 = k/m$ into equation 2.2 the spring constant can be obtained by measuring the mean square displacement of the oscillator, or in this case the cantilever, as

$$k = \frac{k_B T}{< x^2 >}. \tag{2.3}$$

Thermal fluctuations of AFM cantilevers at room temperature are deemed small enough to approximate an AFM cantilever as a simple harmonic oscillator. The spring constant of the lever can then be calculated by measuring the power spectral density of the cantilever displacement which has a Lorentzian shape.

The power spectrum is then integrated to give the power of the cantilever fluctuations which is also equal to the mean square of the cantilever fluctuations. An estimate for the value of the cantilever spring constant is thus equal to:

$$k = \frac{k_B T}{P}. \tag{2.4}$$

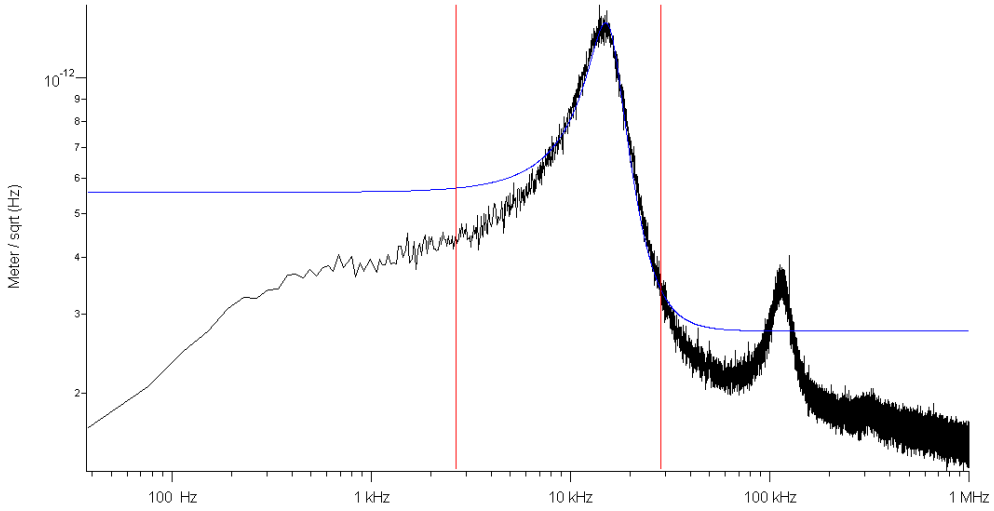

Figure 2.5: Thermal tune of a contact mode cantilever in liquid. The blue line is the Lorentzian fit to the first resonant peak.

where P is the area under the Lorentzian curve. The thermal tune method is the most common method for tuning AFM cantilevers as it is relatively straight forward to do and has little damaging effect on the tip of the cantilever. There are however certain corrections which can be applied to increase the accuracy of the calibration method. For example the position of the optical spot focused on the back of the cantilever can have an effect on the accuracy of the deflection sensitivity of the cantilever [34]. The angle of the cantilever can also have an effect on the accuracy of it's measured deflection sensitivity on an AFM setup with an optical lever detection scheme, as they most commonly have, since the slope of an end loaded cantilever is greater than that of a freely vibrating lever for the same deflection [35]. A correction factor is usually applied to the deflection sensitivity to account for this. These errors that can occur in the measurement of the deflection sensitivity can have a significant effect on the estimated spring constant of an AFM cantilever, which is why it is important to position the optical spot on the back of the cantilever carefully and not make any alterations during

AFM experiments or the lever must be calibrated again. The final accuracy of the measurement of the cantilever spring constant is typically about 5% which will contribute to the error in the mechanical properties extracted from a sample.

Once the spring constant of the cantilever is known the cantilever deflection, Z_c, versus the z-piezo movement, Z_p data can be converted into force-versus-distance data. The deflection of the cantilever multiplied by it's spring constant, k_c, gives the force:

$$F = k_c Z_c. \tag{2.5}$$

Adding the cantilever deflection, Z_c, to the z-piezo movement, Z_p, gives the tip-sample separation which is also known as distance, D:

$$D = Z_c + Z_p \tag{2.6}$$

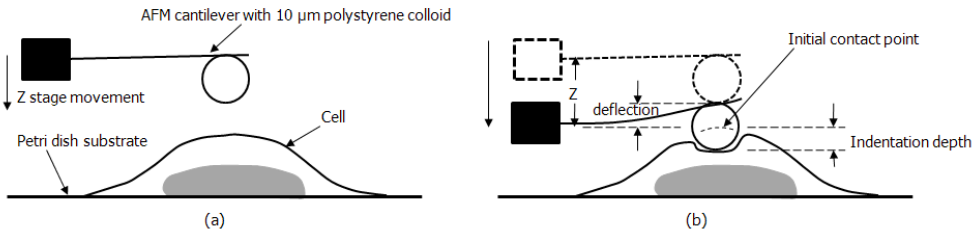

Figure 2.6: (a) Schematic diagram of a 10 μm polystyrene colloid attached to a v-shaped cantilever of nominal spring constant 0.01 N.m^{-1} about to indent an adherent living cell. (b) Schematic diagram displaying the relationship between cantilever deflection, z-stage position and indentation depth during indentation of an adherent living cell.

In the case of a very hard sample when the tip is in contact with the sample the magnitude of the cantilever deflection, Z_c, is equal to the magnitude of the z-piezo movement, Z_p. If the sample is deformable however the indentation, δ, of the sample has to also be considered as shown in figure 2.6. Since the force exerted

on the sample is equal to the spring constant of the lever, k_c, multiplied by the cantilever deflection, Z_c, as stated in equation 2.5, when the sample is deformable and there is an indentation, δ, then the equation becomes:

$$F = k_c(Z_c - \delta). \tag{2.7}$$

Equation 2.7 can then be used to convert the force-distance data into force-indentation data. Living cells are an example of a deformable sample. If the deflection sensitivity of the cantilever is known it can be subtracted from the force-distance data to give force-indentation data in the contact region of the force curve data. There are a number of mechanical contact models that can then be applied to such data to extract mechanical properties from the sample being indented. Below is a review of the contact models that will be used in this thesis to extract mechanical properties from force curve data acquired on living breast cancer cells.

2.2.4 Mechanical Models

For the case of small indentations ($\delta < Z_c$) of an elastic sample with little or no surface forces involved such as adhesion or repulsion the Hertz model can be applied to extract the elastic modulus from force-indentation data. The indentation approach curves are analysed using a modified Hertz equation to determine the Hertz model elastic modulus, E_{Hertz}, of a sample [36]. The model describes the contact of two elastic bodies. In the work presented in this thesis this describes the contact of an assumed infinitely hard spherical probe with a flat, incompressible cell surface, assumed to be a homogeneous elastic half-space with the normal contact between the probe and cell assumed to be frictionless, axisymmetric and without adhesion. These assumptions are not necessarily appropriate for living

cells, but the model results in a consistent and reproducible measurement related to cell elasticity as will be shown in chapter 4. Since this model does not take into account the sample viscoelasticity and calculated elasticities are rate dependent [37], this makes it imperative that all indentation studies are performed at the same loading rate to be comparable. The Hertz equation for contact with a spherical probe is:

$$F = \frac{4}{3} E_r R^{\frac{1}{2}} \delta^{\frac{3}{2}} \tag{2.8}$$

where F is the applied force, R is the radius of the spherical probe, δ is the depth of indentation and E_r is the reduced elastic modulus, which is related to the elastic modulus of the cell by:

$$\frac{1}{E_r} = \frac{(1 - v_{tip}^2)}{E_{tip}} + \frac{(1 - v_{cell}^2)}{E_{cell}} \tag{2.9}$$

where ν is the Poissons ratio and E_{cell} is the elastic modulus of the cell as determined by a specific model. The cell is assumed incompressible; therefore a Poissons ratio of 0.5 is used [37].

Indentation retract data can be analysed using the Oliver and Pharr method. This method was originally described for indentation type testing of hard elastic-plastic samples [38]. More recently this method has characterised the mechanical properties of articular cartilage [39, 40] and there are some studies determining the mechanical properties of cancer cells [41]. It is assumed that during the unloading portion of the force curve acquisition, the displacements recovered are predominantly elastic [42]. The unloading data is fitted using a power law equation:

$$P = \alpha (h - h_f)^m \tag{2.10}$$

where P is the indenter load, h is the indentation and α and m are power law fitting constants [38]. For a spherical indenter $m = 1.5$ [43]. From this fit the elastic unloading stiffness, $S = \frac{dP}{dh}$ can be calculated by differentiating 2.10 at maximum load and indentation. The Oliver Pharr model elastic modulus, E_{OP} of the cell can then be calculated from equation 2.9 and the following relationship:

$$E_r = \frac{\sqrt{\pi}}{2}\frac{S}{\sqrt{A}} \tag{2.11}$$

where A is the projected contact area of the indenter into the surface; which for the spherical colloid used in this instance equates to:

$$A = \pi a^2 \tag{2.12}$$

In this equation a is the radius of the contact which can be calculated geometrically from the expression:

$$a = \sqrt{2h_cR - h_c^2} \tag{2.13}$$

The contact depth, h_c is calculated from a relationship between the initial stiffness, S, the indenter load, P, and the indentation, h:

$$h_c = h - \frac{\varepsilon P}{S} \tag{2.14}$$

where ε is a geometric constant which has the value 0.75 for a spherical indenter [38] as shown schematically in figures 2.7 (a) and (b).

Other contact models used for extracting mechanical properties from force-indentation data include the Johnson-Kendall-Roberts (JKR) model [44] and the Derjaguin-Müller-Toporov (DMT) model [45]. Both these models take into account the adhesive interaction between the tip and sample during indentation,

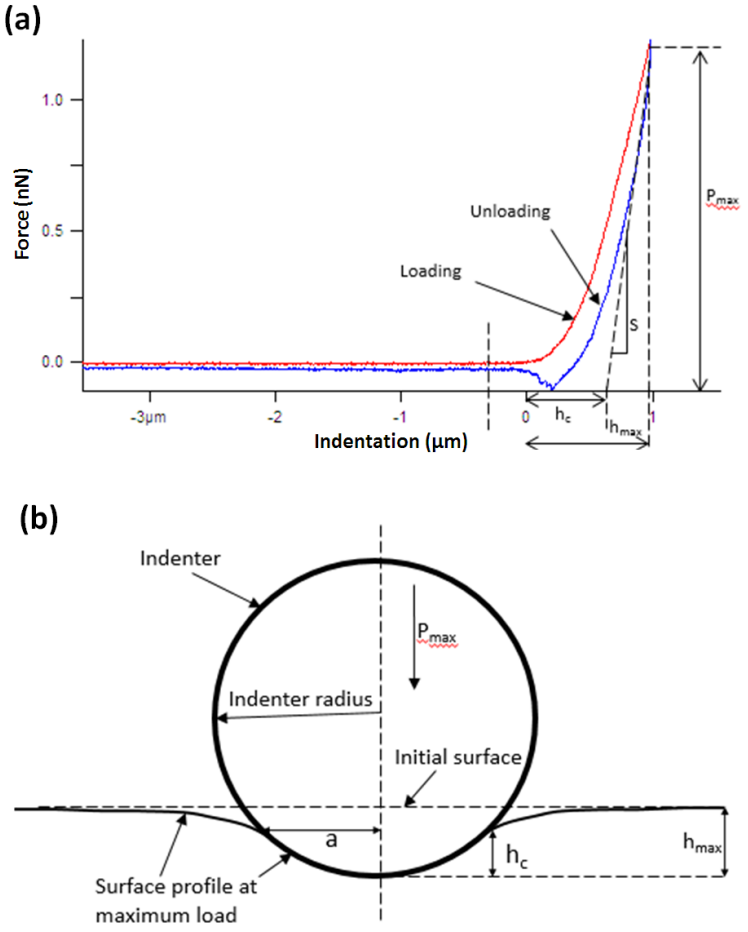

Figure 2.7: (a) Force-indentation curve data from indentation of a living cell showing the retract data which is used in the Oliver Pharr method. (b) Schematic diagram of the indentation using a colloidal probe containing parameters used in Oliver Pharr analysis.

whereas the Hertz model neglects the adhesion of the sample and so is applied to samples where the adhesion between tip and sample is minimal. The Hertz and Oliver Pharr models have been discussed in more detail since they are the models used in chapter 4 and chapter 5 of this thesis.

Although the Hertz and Oliver Pharr models measure the elastic properties of cells, neither take into account that biological materials exhibit both elastic and viscous properties. The time dependent response of biological materials may have important implications in the progression of diseases such as cancers [46]. The viscoelastic properties of cells can be extracted from the stress relaxation response to an applied strain using a Hertz contact model for viscoelasticity derived by Darling et al [47]. The model describes the viscoelastic response of a cell as a standard linear solid as shown in figure 2.8:

$$F(t) = \frac{4R^{\frac{1}{2}}\delta_0^{\frac{3}{2}}E_R}{3(1-\nu)}(1 + \frac{\tau_\sigma - \tau_\varepsilon}{\tau_\varepsilon}e^{\frac{-t}{\tau_\varepsilon}}) \tag{2.15}$$

where E_R is the relaxed modulus, δ_0 is the total sample deformation and τ_σ and τ_ε are the relaxation times under constant load and deformation respectively [46]. By fitting this equation to the stress relaxation data values for E_R, τ_σ and τ_ε can be extracted directly to calculate the apparent viscosity, μ_{cell}, of the cells:

$$\mu_{cell} = E_R(\tau_\sigma - \tau_\varepsilon) \tag{2.16}$$

The instantaneous, E_0, and Youngs moduli, E_Y, are then calculated using the following relationships:

$$E_0 = E_R(1 + \frac{\tau_\sigma - \tau_\varepsilon}{\tau_\varepsilon}) \tag{2.17}$$

and

$$E_Y = \frac{3}{2} E_R \tag{2.18}$$

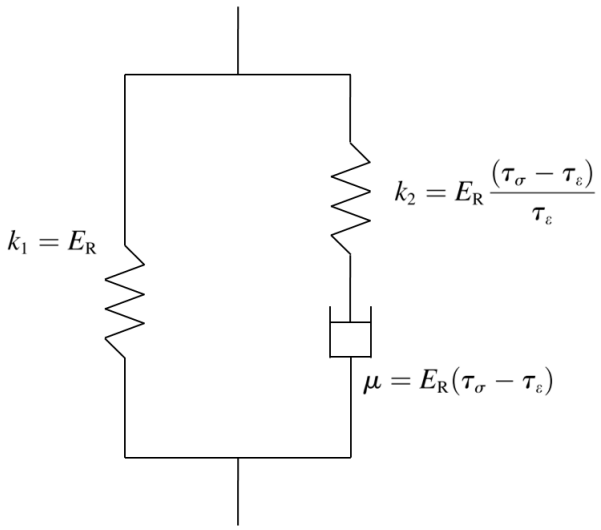

Figure 2.8: Schematic diagram of a standard linear solid.

There are a number of other methods to extract viscoelastic parameters of samples using AFM which include oscillating the tip during force spectroscopy experiments and fitting mechanical models to that oscillatory data to extract viscoelastic parameters [48, 49] or by fitting alternative models to stress relaxation data [50, 51], however these methods are generally difficult to extract physical parameters from the AFM data that can be attributed to the living cells due to the difficulty in associating model parameters to cellular structure. The simple viscoelastic model described above is an effective model to extract a good approximation of the viscous and elastic properties of the cells being investigated.

Single indentations of a sample will yield specific mechanical information about that point, however by taking force-indentation data at multiple points of a sample its mechanical properties can be 'mapped' over its entire surface. These 'force maps' can be acquired by indenting multiple points over a sample whilst also

raster scanning the probe over that sample [52] and can give information on the elastic heterogeneity of a sample. This force mapping method will be described in more detail in the experimental chapters as it plays an important role in the characterisation of breast cancer cells throughout this work.

2.3 Biological Applications of AFM

2.3.1 Early AFM Imaging of Biological Samples

The potential to investigate biological samples and systems with the AFM was realised early after it's invention due to the ability to operate the scanning probe microscope in a number of different aqueous environments. This form of high resolution microscopy coupled with the ability to investigate samples under near physiological conditions made it an important invention in the study of living cells especially. Early biological samples investigated using the AFM included following the polymerisation of fibrinogen [53], studying the dynamical properties of F-actin in living cells [54], the investigation of cellular membrane changes of living cells after viral infection [55], observing the activation of human platelets [56] and the study of DNA [57] to name but a few. By imaging biological samples in aqueous conditions it not only keeps the sample in it's natural state but also increases the resolution of the imaging by removing the capillary force and reducing Van der Waals forces experienced by the scanning probe in air [53].

It was not long before the potential of the AFM as a force sensor was being investigated to measure interaction forces between the probe and the sample. As well as measuring the force applied to a sample the AFM as a force probe has the ability to measure the adhesion between the probe and sample. Measurements of adhesion forces were performed on ligand-receptor pairs [58] resulting in the

quantisation of the unbinding forces of individual molecular pairs. This type of AFM is conducted by functionalising the AFM probe with either a ligand or a receptor and probing the corresponding receptor or ligand with the functionalised probe and measuring the force required to separate the two. This technique is known as single molecule force spectroscopy (SMFS) and the AFM is ideally suited for performing these measurements due to its high force sensitivity, however it is very time and cost intensive. Alternative approaches to using AFM for this type of measurement are micropipette aspiration and optical trapping techniques. The advantage AFM has over these alternative techniques is that they are complex to setup compared with AFM and they are limited to smaller detachment forces [59]. Adhesion measurements have also been performed on DNA [60] by the attachment of a DNA strand to a spherical probe and measuring the adhesion between this probe and another strand of DNA. The application of forces to soft samples to extract elastic properties was also pioneered soon after the invention of the AFM [61, 62]. Initial experiments by Tao and Lindsay and Weisenhorn *et al* looked at a range of samples including rubber, bone, cartilage and most importantly for this work, living cells. Viscoelastic measurements made on biological samples were also performed using force modulation mode [63] although providing quantitative analysis of viscoelastic parameters proved difficult.

2.3.2 Current Application of AFM in Biology

Over the past 20 years the field of biological AFM has developed to a point where the pioneering studies mentioned are now routine experiments that can be performed on commercially available AFMs. Adhesion measurements and elastic characterisation of 'soft' biological samples as well as high resolution imaging are now common place in an AFM laboratory environment. In Sheffield alone I

am surrounded by a diverse range of research using AFM into biological systems including parasitic adhesion interactions, plant guard cell mechanical characterisation, the investigation of antibiotic effects on *staphylococcus aureus* bacteria [64] and the study of nerve cell growth. A very good example of the advancement of AFM and its use in biology and how the AFM can visualise functioning biological mechanisms in a way other forms of microscopy cannot is the observation of myosin molecules translocating along actin filaments using high speed AFM imaging [65]. In this work myosin motor proteins can be seen 'walking' along an actin filament and are believed to be able to transport intracellular components using this method. Actin-myosin interaction is also known to be involved in cell polarity and motility via cytoskeletal restructuring [66]. This is an important example of how improving techniques in biological AFM are enhancing our understanding of living systems and processes. Cytoskeletal rearrangements are obviously also very important in the progression of cancer and any changes in such intracellular structure can potentially be studied using AFM. Mechanical mapping of cancer cell surfaces is one method which can be used to investigate this.

Using the AFM as a micro-indenter and applying a mechanical model such as the Hertz model to the acquired force-distance data a number of cell types have been characterised mechanically using the AFM over the past twenty years. Early studies by Radmacher looked at human platelets [67]. There is also mechanical data available for fibroblasts [68], normal and cancerous human bladder cancer cells [69], human corneal epithelial cells [70] and osteoblasts [71] to name but a few. A number of studies have focused on comparing the mechanical properties of benign and cancerous cells for particular cancers and have shown that benign cells are typically an order of magnitude 'stiffer' than their cancerous counterparts [41, 37, 69, 72, 73, 74, 75], which has lead to the hypothesis tested in this work

that a cells mechanical deformability may correlate with it's metastatic potential. This is the main hypothesis of chapters 4 and 5 and will be discussed in greater detail in these chapters.

Another AFM technique which is used in chapter 6 of this thesis is single cell force spectroscopy (SCFS). Similar to SMFS this technique is used to measure adhesion interactions between two surfaces, but instead of investigating specific ligand/receptor interactions and the unfolding of individual proteins an entire living cell is attached to the tip of the cantilever and it's interaction with another surface or cell is studied.

2.3.3 Single Cell Force Spectroscopy

AFM single cell force spectroscopy (SCFS) is a method in which the adhesive interaction between living cells and a substrate can be quantified with high force resolution and good control of contact conditions [59]. The protocol involves the attachment of a living cell to a cantilever and using this cell functionalised lever to probe a substrate of interest. In the interest of the work described in this thesis the substrate of interest is a confluent layer of cells known to interact with the cancer cell attached to the cantilever. The technique does however have its limitations. To perform such experiments the AFM setup should be able to fully separate the two cells being investigated [59]. Currently the maximum limit of z-piezo travel for commercial AFMs is about 100 μm. Most AFMs though have a maximum z-piezo range of approximately 12 μm which is not sufficient to fully separate two living cells from one another. This is a problem faced in this work and the experimental setup had to be developed and adapted to be able to conduct SCFS on the AFM used throughout these studies (Asylum MFP-3D), which is discussed in chapter 6. The experimental protocol and data capture are relatively time and cost intensive

for SCFS. To build up enough data to make statistically valid conclusions from the results requires a lot of time due to only one cell being attached to the cantilever at a time, which limits the contact time between cells [76]. The data collected from these interactions can be seen in a typical force-distance curve in figure 2.9. It can be seen on the retract (blue) data that there are a number of unbinding events occurring during the dissociation of two cells. One of the limitations of SCFS is the ability to interpret this complex data into meaningful information about the interaction between cells [77]. This is difficult because there are a number of non-specific interactions as well as specific interactions involved in cell-cell attachment. One way to investigate the effect of specific interactions is to treat the cells prior to or during the experiment to inhibit specific attachments to see how important certain cell adhesion molecules are in the adhesion between two cell types. This method will be used in chapter 6 to investigate the adhesion interaction between metastatic breast cancer cells and osteoblast-like cells to simulate the tumour micro-environment typically found in the bone at sites of secondary metastases. Current breast cancer therapeutics have also been applied to the cells to investigate what effect these treatments have on the adhesive interaction between these cells of interest. Both of these techniques can give important insights into not only the biomechanical properties of cell binding but also the biological signalling pathways triggered by such interactions.

SCFS is a very useful method in characterising the mechanical and biological interactions between different cell types and will be an important part of this thesis with the development of an AFM setup to perform such experiments to investigate cells involved in breast cancer metastasis. These experiments will be discussed in detail in chapter 6.

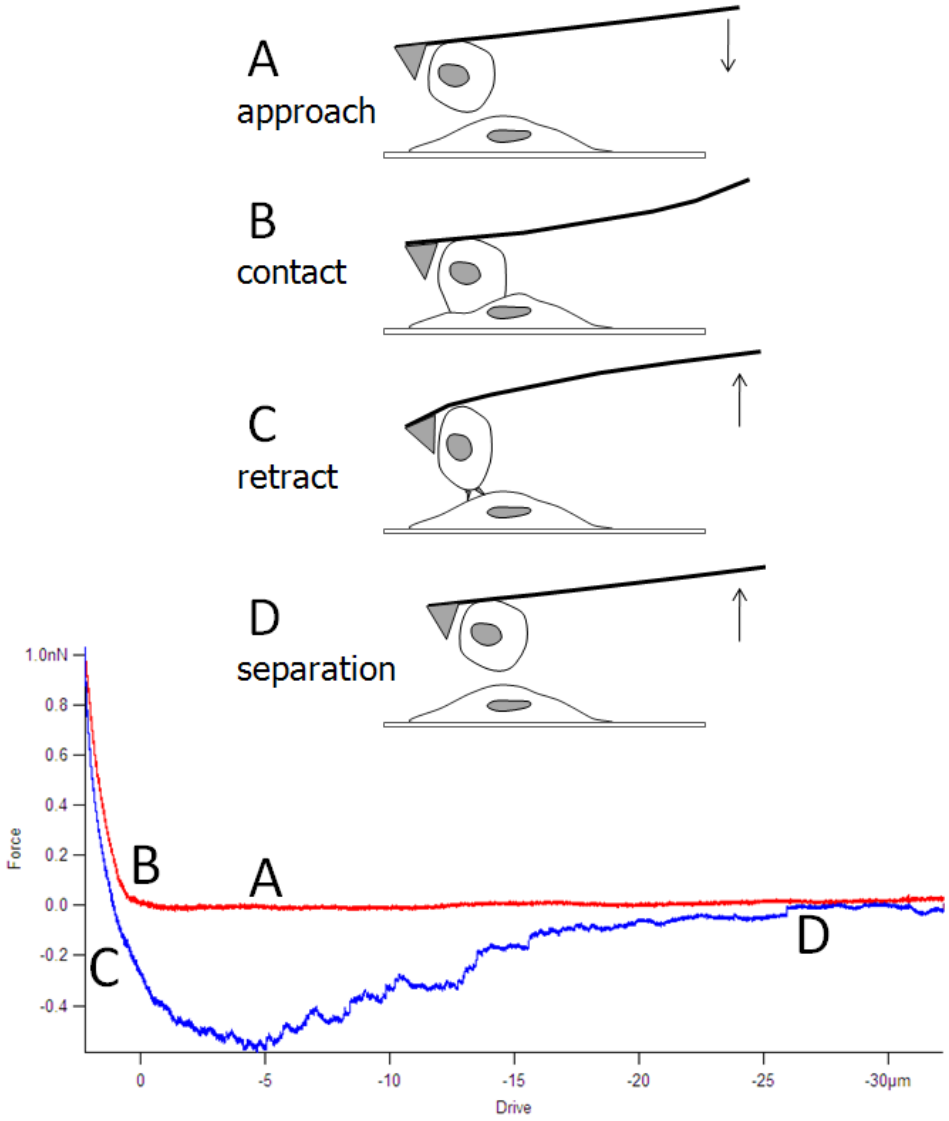

Figure 2.9: Schematic diagram of a sampling cycle for an experiment to measure the adhesion between two cells. Below is a corresponding force curve showing the unbinding events involved in separating a living cell attached to an AFM cantilever from another cell.

Chapter 3

Experimental Methods

3.1 Introduction

Throughout the work presented in this thesis a number of breast cell lines are used to study the mechanics of breast cancer metastasis. These breast cell lines are immortalised which means they have an unlimited self-replicating ability making them useful tools in modelling cancer *in vitro*. Cells can be immortalised in a number of ways including selection of cells able to undergo division after spontaneous or induced mutagenesis, deregulation of cell cycle constraints by the introduction of a virus to allow cells to continually proliferate or simply by the isolation of cancerous cells that are able to self-replicate without further interference. The latter is the origin of the first immortalised cell line which was the HeLa cell line, named after the lady from which the cells originated, Henrietta Lacks [78]. The MD Anderson series and Michigan Cancer Foundation series of cell lines were established in 1973 and 1978 respectively [79, 80] which are the origins of the breast cell lines used in these studies. There are many advantages of using immortalised cell lines in research which include unlimited self-replication when grown in simple growth

media which allows large numbers of cells to be grown for experiments to be replicated almost infinitely. They are financially and ethically a much easier way of modelling cancer *in vitro* when compared with primary samples which can be very difficult, especially in the UK, to get approval for use. The use of cell lines also allows contaminated samples to be destroyed and backup samples stored in liquid nitrogen can be thawed out and used to replace them. One major disadvantage of immortalised cell lines is the change in phenotype and genotype of such cells when cultured over a period of time. These changes are responsible for the biological variation reported in results from different laboratories using the same cell line as has been shown for the MCF-7 cell line [81]. This makes it very important to note the tissue bank from which the cells are from when making comparisons with the literature and also the passage number of the cells, that is the number of times the cells have been sub-cultivated. It is for this reason that cells used throughout this thesis were never used for more than a period of 20 passages. Cells were frozen down and stored in liquid nitrogen so that when samples reached a certain age they were destroyed and frozen down cells were thawed out for experimental use.

3.2 Cell Culture

3.2.1 Cell Culture

The breast cancer cell lines used needed to be sub-cultivated upto twice a week to allow them to continue to grow. Sub-cultivation was performed as follows. Working in a class II cabinet, the culture medium was aspirated from the cell flask and the cells were washed with 5 mL (for a T75 flask) of sterile phosphate buffered saline (PBS). The PBS was then removed and 5 mL of trypsin-EDTA was added to the flask before incubating the cells at 37°C and 5% CO_2 for 5 min.

Trypsin is a protease which detaches the adherent cells from the flask surface. Once the cells had become detached from the flask they were pipetted into a sterile tube and centrifuged for 5 min at 1000 rpm. The supernatant was then removed and the cell pellet was re-suspended in 2 mL of fresh media appropriate to the cell type being sub-cultivated. An appropriate volume of cell suspension was then added to a new flask containing 15 mL of fresh media and the flask(s) were then incubated at 37°C and 5% CO_2. This protocol was followed for each cell line used apart from the bone marrow endothelial (BME) cells. For BME cells the new flasks were incubated at 37 °C and 5% CO_2 with 2 mL of 50 mg.mL^{-1} fibronectin in PBS for one hour prior to sub-cultivation. This allowed the non-adherent BME cells to adhere to the flask surface. A description of the culture medium used for each cell line is stated in the following subsections of this chapter.

3.2.2 MCF-10A

The MCF-10A (ATCC, USA) cell line is an adherent, non-tumourigenic breast epithelial cell line originating from a 36 year Caucasian female patient. MCF-10A cells were cultured in Dulbeccos modified Eagles medium (DMEM) containing 1% penicillin/streptomycin, 1% fungizone, 10 mM Hepes, 5% horse serum, 0.01 mg.mL^{-1} insulin, 20 ng.mL^{-1} epidermal growth factor and 0.5 μg.mL^{-1} hydrocortizone at 37°C and 5% CO_2 in a humidified incubator and used between passages 15-20. A sub-cultivation ratio of 1:3 was used and media replaced every two to three days. Unless otherwise stated this is the media that MCF-10A cells were grown in throughout the work included in this thesis.

3.2.3 MCF-7

The MCF-7 (ATCC, USA) cell line is an adherent, non-invasive breast epithelial cancer cell line derived from a primary breast tumour from a 69 year old Caucasian female in 1970. MCF-7 cells were cultured in RPMI 1640 media containing 10% foetal calf serum (FCS), 1% penicillin/streptomycin, 1% L Glutamine and 1% fungizone in T75 flasks at 37°C and 5% CO_2 in a humidified incubator and used between passages 20 and 40. A sub-cultivation ratio of 1:3 was used with cell media being replaced every two to three days. Unless otherwise stated this is the media that MCF-7 cells were grown in throughout the work included in this thesis.

3.2.4 MDA-MB-231

The MDA-MB-231 (ATCC, USA) cell line is an adherent, highly invasive, triple negative breast epithelial cancer cell line originating from a secondary tumour site pleural effusion in a 51 year old Caucasian female patient. MDA-MB-231 cells were cultured in the same medium as the MCF-7 cells in T75 flasks throughout the experiments in this thesis unless stated otherwise. A sub-cultivation ratio of 1:20 was used with cell media being replaced every two to three days.

3.2.5 Saos-2

The Saos-2 cell line is a non-tumourigenic osteosarcoma cell line from an 11 year old Caucasian female. The cell line has several osteoblastic properties [82] and was used throughout this thesis for the cells osteoblast-like properties. Saos-2 cells were cultured in Dulbeccos modified Eagles medium (DMEM) without pyruvate, containing 10% FCS, 1% penicillin/streptomycin, 1% fungizone, 1% L Glutamine in T25 flasks at 37°C and 5% CO_2 in a humidified incubator and used between

passages 10-30. A sub-cultivation ratio of 1:3 was used with cell media being replaced upto twice a week. Unless otherwise stated the Saos-2 cells were sub-cultivated following this method throughout the works described in this thesis.

3.2.6 Bone Marrow Endothelial (BME) Cells

Bone marrow endothelial (BME) cells were obtained from Dr. Michael Brown, University of Manchester [83], and were cultured in bone marrow growth medium (Iscoves modified Dulbeccos medium (350 mOsm)), 10% FCS, 10% horse serum, 5 x 10^7 M hydrocortisone and 1% antibiotic/antimycotic solution) at 37°C and 5% CO_2 in a humidified incubator and used between passages 15 and 20. The cells were sub-cultivated at a ratio of 1:2 typically every five days or when the cells reached 90% confluency. As stated in the cell culture section the T25 dishes were coated with fibronectin prior to sub-cultivation.

3.2.7 Freezing/Thawing Cells Stored in Liquid Nitrogen

It is common practice to keep a working bank of cells stored in liquid nitrogen for the reasons previously mentioned. To freeze cells in liquid nitrogen for long term storage the following protocol was followed. A freezing solution consisting of 16 mL of the cells media, 2 mL FCS and 2 mL dimethyl sulfoxide (DMSO) was mixed before following the sub-cultivation method up until the pellet is re-suspended in media. For this protocol the cells are re-suspended in the freezing down solution at this point and 1 mL of the cell suspension is added to each cryogenic vial. Upto a total of 20 vials can be filled with this amount of freezing down solution. The vials are then placed into a plastic freezing container in which the vials are surrounded by isopropanol (IPA) and the container is then placed in a -20°C freezer for one hour. The container is then transferred to a -80°C freezer for 24 h before storing

in a liquid nitrogen dewar. The DMSO acts as a cryo-protective agent lowering the freezing temperature of the freezing down solution and slows down the cooling rate of the solution which reduces the risk of ice crystal formation during freezing which can kill the cells.

When thawing the cells a cell flask containing warm media is prepared just as it would be for sub-cultivated cells. A frozen down cryogenic vial is lifted out of liquid nitrogen and thawed out using a water bath at 40°C. Once the cell suspension is nearly completely thawed it is pipetted into the flask containing the warmed media and transferred to a humidified incubator at 37°C and 5% CO_2. After 24 h the cells are checked with an optical microscope to ensure they are attached to the flask. The media is then pipetted off removing any non-adhered cells and the remainder of the DMSO before adding fresh media and returning to the incubator. The usual sub-cultivation procedure is then followed until the cells reach a certain passage at which 'fresh' cells need to be thawed from the working bank of cells stored in liquid nitrogen.

3.3 AFM Techniques

3.3.1 AFM setup

An Asylum Research MFP-3D AFM was used to capture the entirety of the AFM data presented in this thesis (see figure 3.1). The MFP-3D is an AFM integrated with an inverted optical microscope (Olympus microscope IX71, Tokyo, Japan) to allow optical microscopy techniques to be performed simultaneously with AFM data capture. This makes it a useful tool for studying the mechanical properties of biological samples as the sample can be viewed using the optical microscope to locate specific cell regions to acquire mechanical measurements using the AFM.

This setup also allows the use of fluorescence microscopy to identify cells that have been 'tagged' with specific markers to identify sub-populations of cells with a particular biological interest, which is very important in the selection of cell sub-populations later in this thesis.

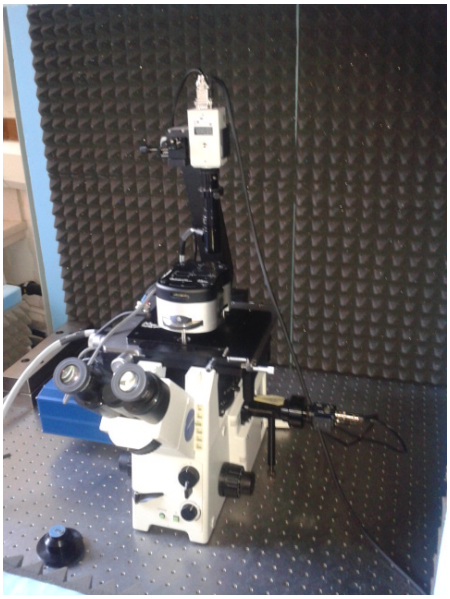

Figure 3.1: Image of Asylum MFP-3D AFM setup.

3.3.2 Development of Imaging Living Cells in Liquid

Initial AFM experiments were performed to familiarise myself with the preparation of living cell samples for use with the AFM. The aim of these experiments was to develop a technique to image living cells using AFM in either contact or intermittent-contact mode. The MCF-7 and MDA-MB-231 cell lines were predominantly used for these experiments as these are the two breast cancer cell lines used throughout these studies. Following the sub-cultivation protocol in section 3.2 up to the point at which the cells were pipetted into a new flask, at which point a fraction of the cells were also pipetted into 50 mm x 9 mm petri polystyrene dishes (BD Falcon). Cells were counted using the Vi-Cell cell viability analyser

(Beckman Coulter). The Vi-Cell is a machine which automates the trypan blue exclusion method to assess cell viability. Cells are drawn into a flow through chamber and mixed with trypan blue. The dye is only taken up by dead cells. A camera then captures an image for 50 random fields of the cell suspension and particle analysis software is then used to count the number of total and viable cells per field and averages the data to give a concentration of cells per millilitre of cell suspension. Typically approximately 2.5 x 10^5 cells were pipetted into each dish before incubating for 24 h in a humidified incubator at 37°C and 5% CO_2. After incubation the cell media was aspirated off and the cells were washed once with PBS. Two millilitres of fresh cell media was then added to the dishes prior to AFM imaging in liquid. The cantilever holder on the MFP-3D is suitable for use in liquid and was sonicated first in IPA for five minutes, followed by five minutes sonication in de-ionised water before drying with a nitrogen airline prior to and after every AFM experiment. The cantilever is then clamped into the holder and attached to the AFM head as shown in figure 3.2. A small droplet of media is

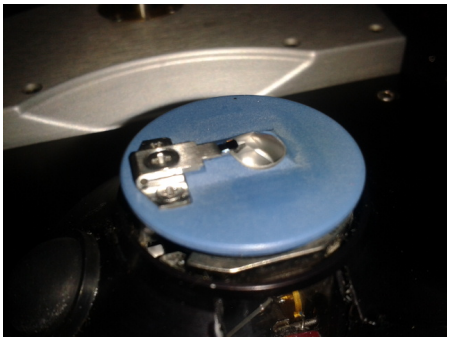

Figure 3.2: Image of the cantilever positioned in the Asylum MFP-3D cantilever holder.

pipetted onto the cantilever before the head is lowered towards the sample. This is to prevent bubbles of air being trapped under the cantilever when it is lowered into contact with the dish containing media and the cell sample. Once the cantilever is submersed in the media the laser is positioned onto the back of the

lever over the tip and the lever is brought into focus using the top optics shown in figure 3.1. For intermittent contact mode the cantilever would then be 'tuned' which involves measuring the cantilever fluctuations due to brownian motion to discover the resonant frequencies of the cantilever. The drive frequency is then set to just below the frequency of the first vibrational mode. For contact mode 'tuning' the lever is not necessary to produce a topographical image. When imaging living cells in contact mode I used the 'softest' cantilevers available to me which were the 0.01 $N.m^{-1}$ triangular cantilevers (cantilever B on the MLCT cantilevers, Bruker, USA). When choosing a cantilever to image a sample it is important to try to match the stiffness of the lever with that of the sample. This is to increase the force sensitivity of the tip-cell interaction and reduce the frictional force exerted on the cells during imaging. Imaging living cells can be difficult due to the disruptive effect the tip has on the cell morphology [84]. Due to the softness of the breast cancer cells the lateral forces exerted on the cell by the tip cause the cell to deform whilst being imaged. When imaging living cells these lateral forces can cause the cells to deform under the force of the cantilever and even cause them to detach from the substrate making it impossible to image the cell.

Initially I imaged the MCF-7 and MDA-MB-231 breast cancer cell lines on the Asylum MFP-3D using intermittent contact mode as shown in figure 3.3. It was found that even using this mode of AFM imaging it proved very difficult not to damage the cells during imaging. Thermal drift of the cantilever during scanning meant that the images were significantly distorted. To reduce thermal drift of the cantilever the experimental setup was allowed around half an hour to equilibrate before experiments, however drift was still present after this time. After experiencing difficulty imaging the cells using intermittent contact mode in liquid I decided to image the cells using contact mode. The 0.01 $N.m^{-1}$ triangular

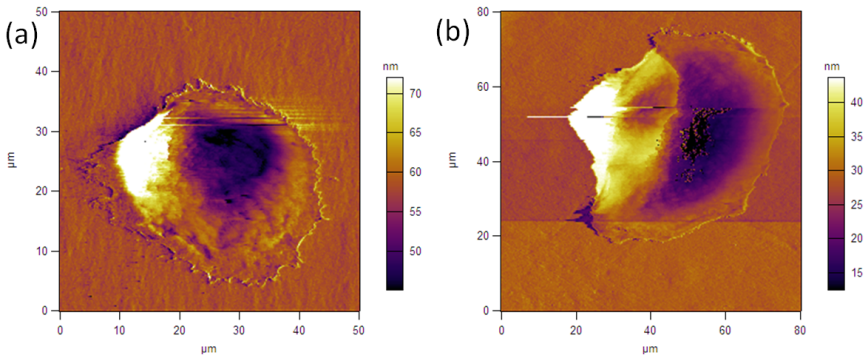

Figure 3.3: Amplitude images of initial intermittent contact mode breast cancer cell imaging. (a) shows an amplitude image of an MDA-MB-231 cell. (b) shows an amplitude image of an MCF-7 cell.

MLCT levers were used for all contact mode imaging in liquid. To improve my imaging technique working with living cells I fixed a dish of MDA-MB-231 cells with 4% formaldehyde. After the usual 24 h incubation in a humidified incubator the media was aspirated off and the cells were washed with PBS. 4% formaldehyde was then pipetted onto the cells and incubated at room temperature for 10 min. The cells were then washed three times with PBS and then imaged in 2 mL PBS. Imaging of the fixed cells highlighted an important artefact when imaging these breast cancer cell lines. The morphology of these cells is similar to a 'fried egg' shape when they are adhered to a surface. They have a central nuclear region which is usually dome shaped or in the case of the 'fried egg' analogy the egg yolk. The spread region surrounding this is then usually much thinner, typically only a few hundred nanometres thick at most. The nuclear region of the cell can vary between a couple of micrometres to around ten micrometres in height depending on the spread of the cell and how adherent the cell is to the substrate. In the case of the fixed cell shown in figure 3.4 the height of the cell is greater than the length of the tip of the cantilever and so as the tip is scanned to the right of the cell it cannot track the surface since the cantilever itself is in contact with the top of the

cell. Due to the cell being 'fixed' the cell is unable to deform under the contact of the cantilever, which may happen when imaging live cells that have not been fixed. The length of the tip is nominally 5 μm so unless longer tips are used it is important that the cells are very spread when imaging them.

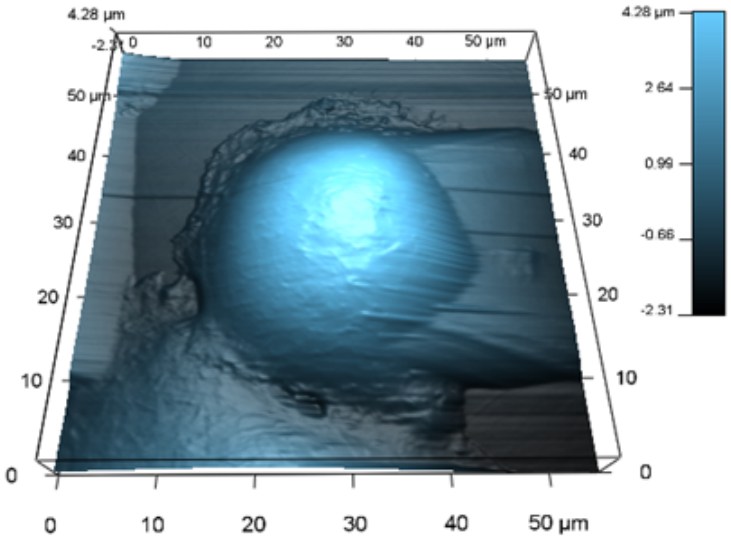

Figure 3.4: A 3D height image of an MDA-MB-231 cell fixed with 4% formaldehyde. The image shows a sloping artefact to the right of the centre of the cell. This artefact occurs due to the length of the imaging tip being shorter than the height of the cell and the steepness of the slope at the edge of the cell. During this part of the image the cantilever as opposed to the tip is in contact with the cell.

I then went back to imaging cells that were not fixed in contact mode. When imaging single cells this time it was noticed that the 'soft' nuclear region of the cells were difficult to image. Imaging the same scan area initially from bottom to top and immediately after from top to bottom it can be seen in figure 3.5 that the direction of the scan can distort the cell.

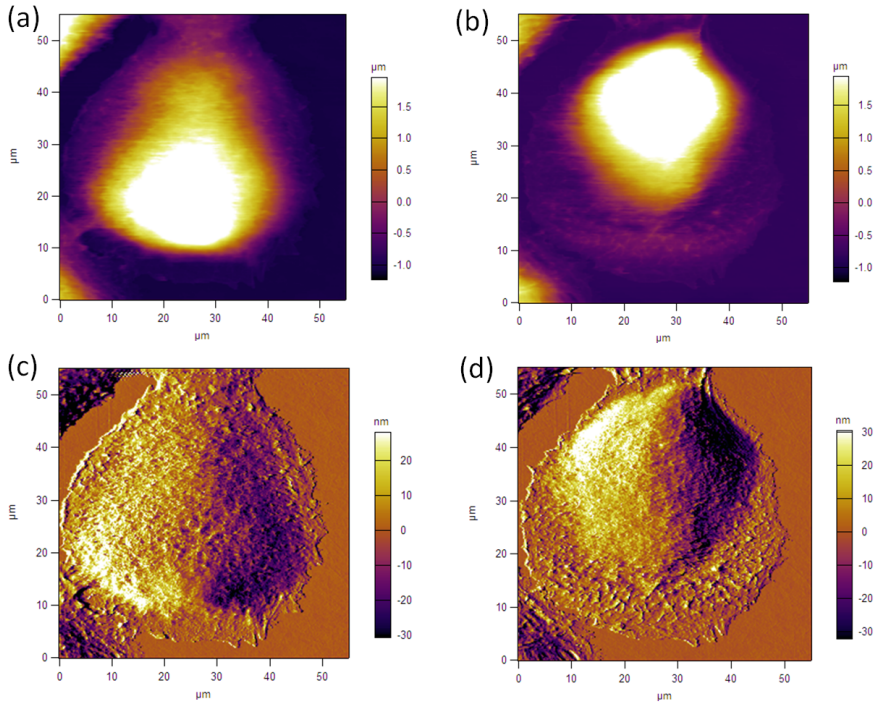

Figure 3.5: Contact mode height and deflection images of a single MDA-MB-231 cell imaged from top to bottom in (a) and from bottom to top in (b). The direction of the scan appears to have an effect on the cell under investigation. Images (c) and (d) are the deflection images that correspond with images (a) and (b) respectively.

To reduce the effect of these artefacts when imaging live cells it is important to allow the system to equilibrate before imaging to reduce thermal drift of the cantilever. Secondly the scan speed is very important. Imaging at a scan rate of around 0.14 Hz was found to track the surface of the cell sufficiently with the feedback loop able to 'react' fast enough to the steep sloping edges of the nuclear region but not too slow that each scan line was at a different height due to cell

movement. The deflection setpoint is also very important. A low setpoint is used to minimise the lateral force exerted on the cells. Typically a setpoint of 0.01 V was used when imaging the breast cancer cell lines. Too high a setpoint can damage regions of the cell, particulary the thin spread regions as shown in figure 3.6.

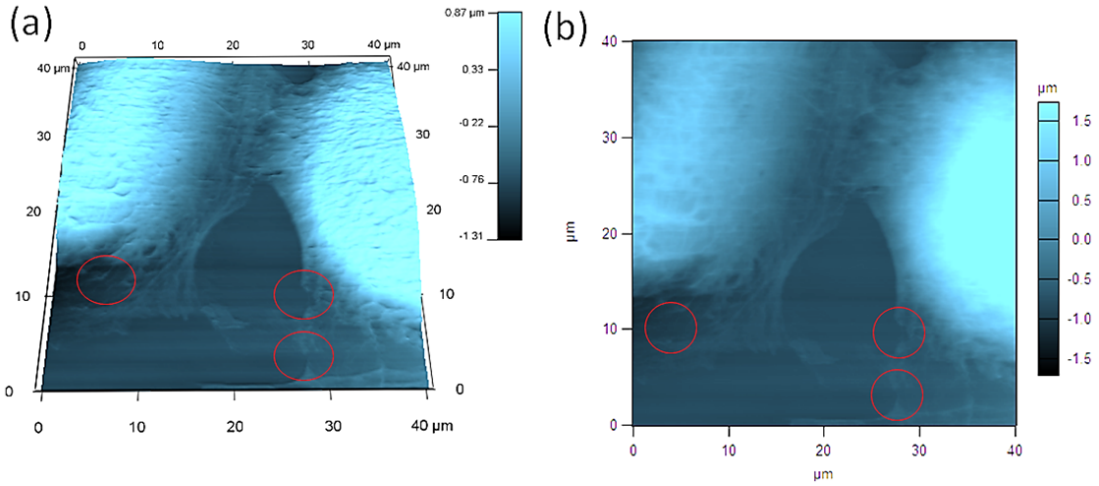

Figure 3.6: Contact mode images of two connected MDA-MB-231 cells. (a) shows a 3D height image of the cells and (b) is the same data represented as a 2D height image. The red circles in these images show regions of the cells which have been damaged by the AFM tip due to the setpoint being too high.

By plating a greater number of cells in each dish the increased cell confluency when imaging allowed small groups or clusters of cells to be imaged. The advantage of this was that when the cells attached to one another they spread out across the substrate causing the height of the central region of the cell to decrease making it easier to image using the AFM. It can be seen in figure 3.7 that the height of the confluent cells is much less than 5 μm which allows them to be imaged much easier than single cells. The cell substrate boundaries are regions where the tip can get stuck and damage the cell as it tracks from the polystyrene dish onto the thin spread region of the cell as can be seen in figures 3.6 and 3.8. If the cells are in contact with each other this boundary is not there and so this problem is

eradicated.

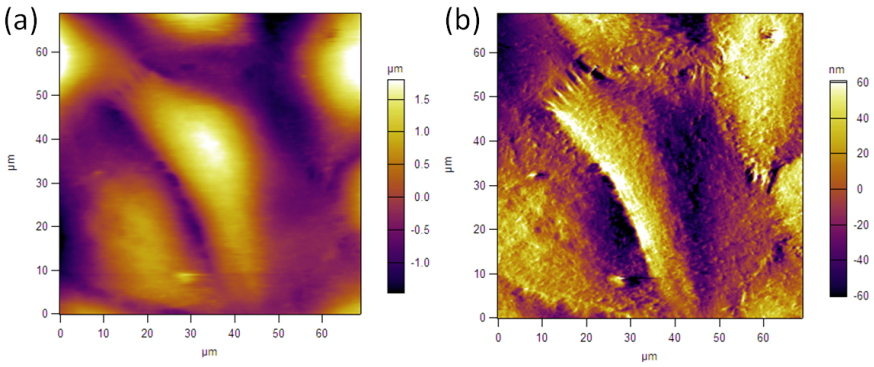

Figure 3.7: Height, (a), and deflection, (b), images of a confluent layer of MDA-MB-231 cells. Several adherens junctions can be seen connecting the central cell to the cells surrounding it in the images.

In figure 3.8 the thin spread region of a single MDA-MD-231 cell has been imaged in contact mode. Due to the nature of the cell membrane being significantly 'softer' than the underlying cytoskeletal components and the fact that these cell regions are incredibly thin compared with the overall height of the cell it is possible to visualise the effect of intracellular structures in these thin regions using AFM.

As well as intracellular imaging the AFM is also able to image the extracellular components of living cells as shown in figure 3.9. This figure shows the height and deflection images of the extra-cellular matrix (ECM) of two adjacent BMECs. The cells were incubated for 72 h after being plated into dishes to allow them to become confluent. Contact mode AFM was then used to image these cells which proved difficult at first since the setpoint was set too high and the tip was 'dragging' through this ECM. By slowing the scan speed and decreasing the setpoint I was able to image the ECM.

To acquire images of single cells the MDA-MB-231 cells were plated into glass bottom dishes (see chapter 4) and incubated for 24 h in a humidified incubator.

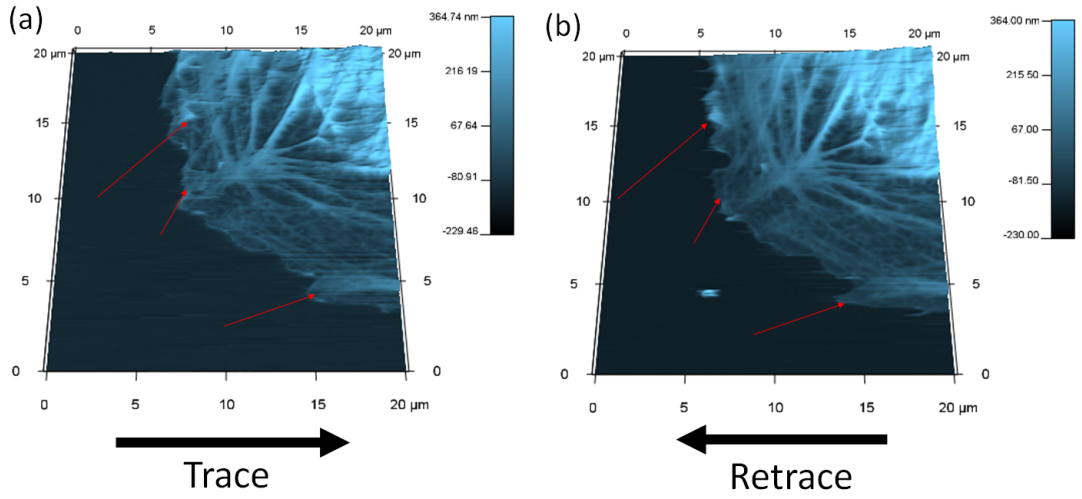

Figure 3.8: 3D height AFM images of a thin spread region of an MDA-MB-231 cell showing the cytoskeletal structure. Image (a) shows the trace image, whereas image (b) shows the retrace image. Arrows on the two images show regions of the cell that are 'disturbed' by the tip during contact mode imaging.

The cells appeared to spread out more on the glass substrate which lowered the height of the cells and allowed them to be imaged in contact mode. Figures 3.10 and 3.11 show contact mode height images of two separate MDA-MB-231 cells. Figure 3.10 has a resolution of 256 x 256 pixels whereas figure 3.11 has a resolution of 512 x 512 pixels. Both images clearly show the spread 'fried-egg' shape morphology of these breast cancer cells with cytoskeletal features clearly visible in figure 3.10. The increased resolution in figure 3.11 appears to give more detail of the surface of the cell. Cross sections shown in both figures show the measured height of each cell with both measuring just over 4 μm in height from the glass to the top of the cell.

Although there are limitations to imaging living cells using AFM, it has been shown here that it is possible to get detailed height information using contact mode for the breast cancer cells being investigated with little damage to the cells. To overcome the imaging artefact shown when the cell height is longer than the

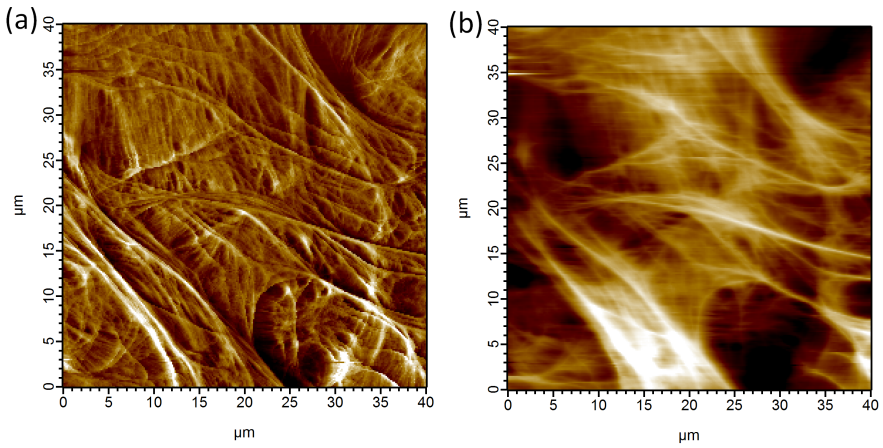

Figure 3.9: Contact mode deflection, (a), and height, (b), AFM images showing the extracellular matrix of a bone marrow endothelial cell layer.

tip length cantilevers with longer tips can be purchased. These cantilevers are, however, relatively expensive compared with the MLCT cantilevers used for these imaging experiments and since the main focus of the work in this thesis was the mechanical characterisation of these breast cancer cell lines I developed the methods mentioned in this chapter to overcome the height limitation I observed by altering the substrate on which the cells were grown and also by plating greater numbers of cells and imaging more confluent clusters of cells.

Contact mode imaging of breast cancer cells has given important information about the morphology of the breast cancer cells (the MDA-MB-231 cells were focused on predominantly as these are the metastatic breast cancer cells which are the biological focus of this work) and enables the visualisation of cytoskeletal components that are responsible for this morphology, however, to extract more information regarding the cells' mechanical properties the use of AFM force spectroscopy was used. This is discussed in greater detail in the subsequent experimental chapters of this thesis. The data analysis methods used to extract mechanical information from these force spectroscopy experiments will be discussed in the next section of this chapter.

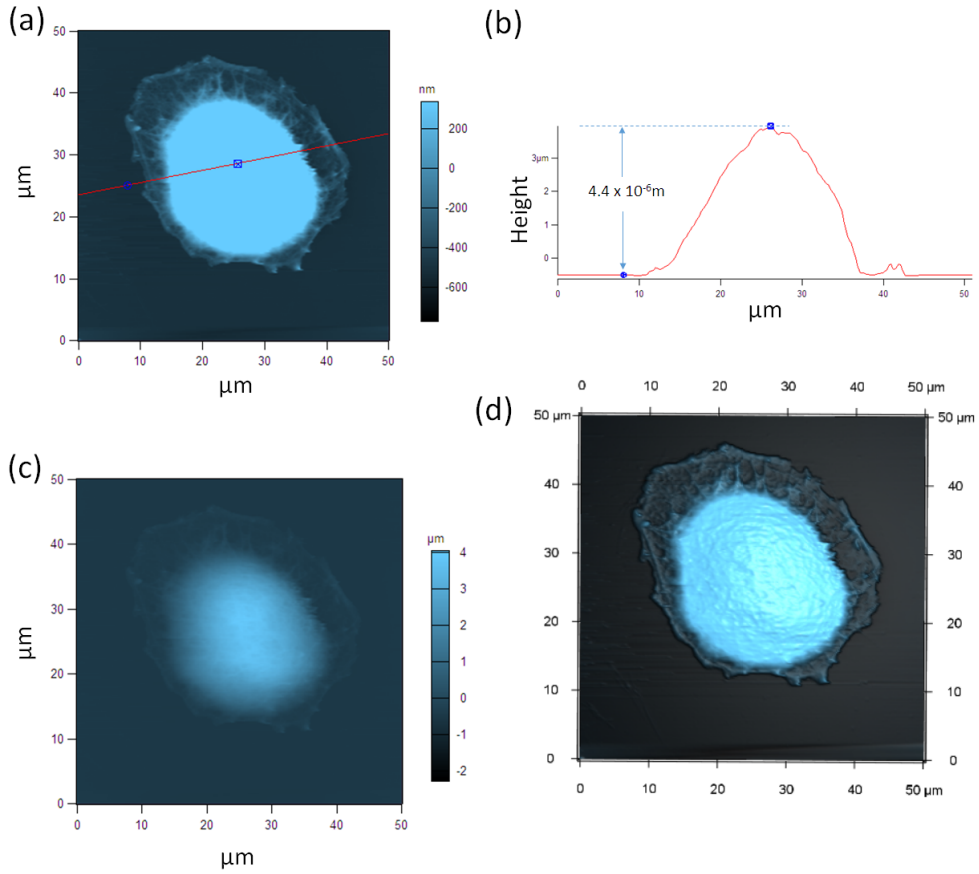

Figure 3.10: Images of a single MDA-MB-231 cell on a glass substrate imaged in contact mode. (a) is a 2D height image of the cell showing a red line which corresponds to the cross section shown in graph (b). Image (c) is a 2D height image of the cell and (d) is a 3D height image which has been rotated so that it is being viewed normal to the glass slide. AFM images are 256 x 256 pixels.

3.4 Data Analysis for Mechanical Characterisation

For the contact model fitting to the data the Asylum Research software (version MFP-3D 120804+1821) which is built in to IgorPro (Wavemetrics, Inc) was used throughout. There is an elastic tab contained in the 'master force panel' which is a user interface within the software which allows the Hertz and Oliver Pharr models to be applied to the force indentation data. Specific parameters have to

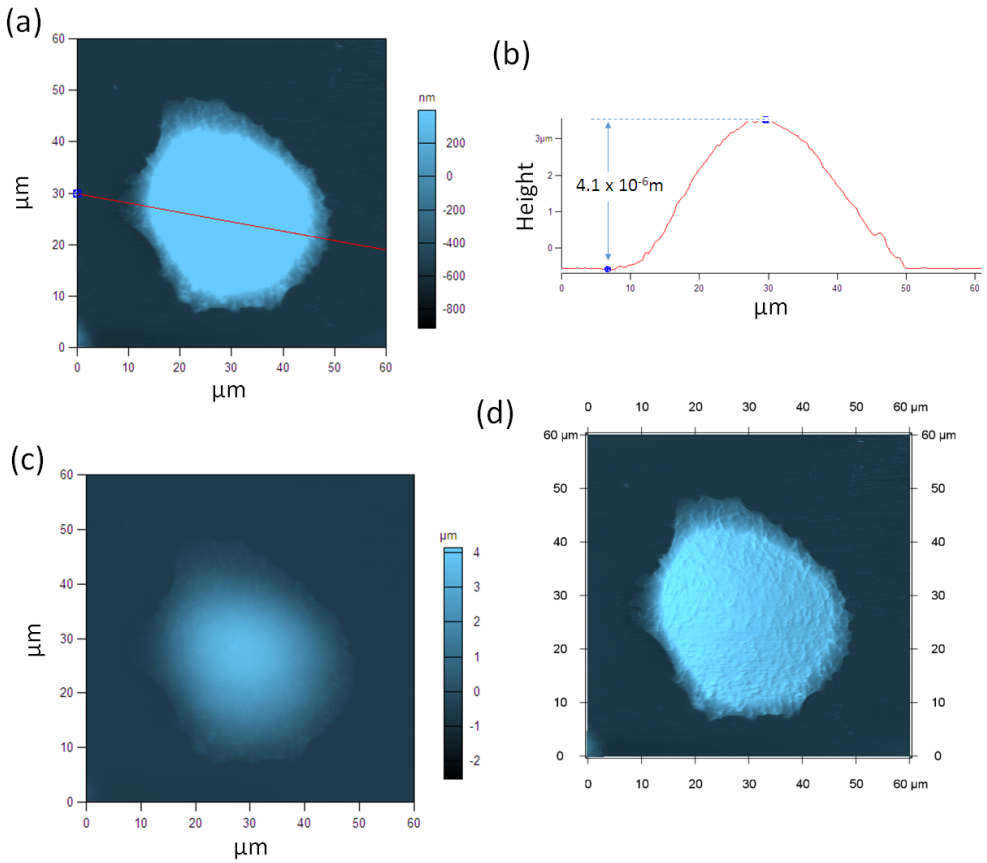

Figure 3.11: Images of a second single MDA-MB-231 cell on a glass substrate imaged in contact mode. (a) is a 2D height image of the cell showing a red line which corresponds to the cross section shown in graph (b). Image (c) is a 2D height image of the cell and (d) is a 3D height image which has been rotated so that it is being viewed normal to the glass slide. AFM images are 512 x 512 pixels.

be manually input such as the tip modulus and Poisson's ratio of the tip and estimated Poisson's ratio of the sample. The Poisson's ratios used were 0.34 and 0.5 for the tip and sample respectively. The viscoelastic Hertz model was not an inbuilt function in the software and so a set of functions were written by myself to fit this model to the stress relaxation data and to extract the parameters necessary to calculate the apparent viscosity of the sample from the data. The following subsections describe the fitting procedures in more detail for each contact model respectively.

3.4.1 Fitting the Hertz Model in IgorPro

As previously mentioned the Asylum Research software has inbuilt functions to extract the Hertz modulus from the force-indentation data. The software allows the choice of a spherical indenter and the radius of the indenter can be input into the model. The software initially performs a line subtract on the non-contact portion of the force-distance data so that it is flat. This is built into the fitting routine and takes the first ten points of the approach data and performs the line subtract on these points. If this is not sufficient the whole of the non-contact data can be selected and 'flattened' manually. The routine then again takes an average of the first ten points and offsets the Y-axis to zero force. An algorithm then 'sweeps' the approach data constantly comparing the data until there is a significant change in gradient which it then offsets to define the contact point. The Hertz equation (equation 2.8) is then fitted to the contact portion of the approach data as shown in figure 3.12. The region of contact data that is fitted can be selected manually by inputting the minimum and maximum percentage of indentation or force as the lower and upper limits of the fit. For the Hertz model fitting in chapters 4 and 5 the initial 50 % of indentation was fitted using this model. The fit returns a value for the reduced modulus, E_r, which is then substituted into equation 2.9 (described in chapter 2) along with the manually inputted values for tip modulus, and the Poisson's ratio of the tip and estimated Poisson's ratio of the sample, which is 0.5 for all fitting performed in this thesis. The Hertz modulus of the sample is then returned from rearranging this equation.

Once the Hertz modulus has been extracted from the force-indentation data it is copied to a spreadsheet in Microsoft Excel for further analysis.

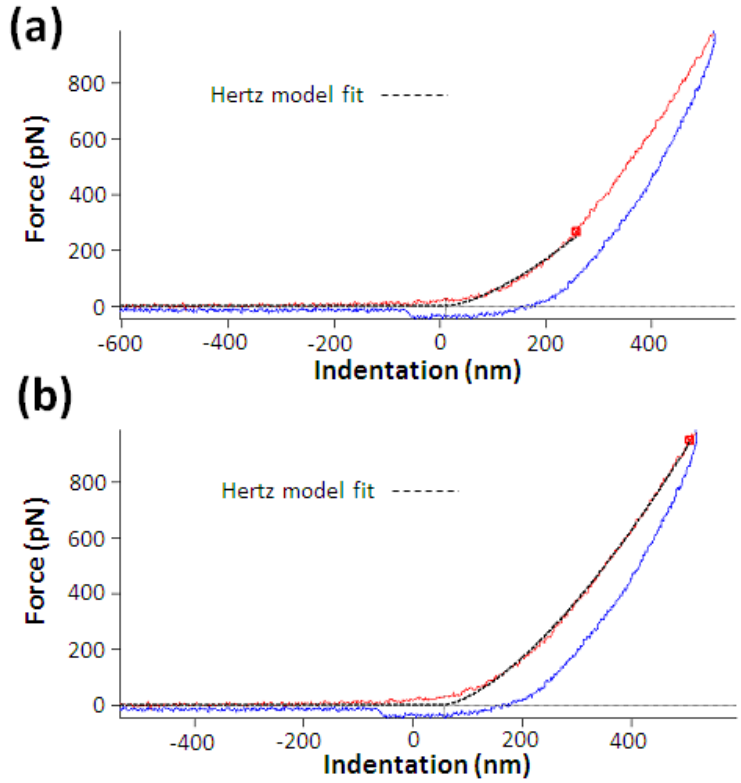

Figure 3.12: Typical graphs showing the region of force-indentation data that is fitted to using the Hertz model in the Asylum Research software in IgorPro. The red curves in the graphs are the approach data and the blue curves are the retract data. (a) shows the Hertz model being fitted to 50 % of the indentation data whereas (b) show the model being fit to 100 % of the indentation data.

3.4.2 Fitting the Oliver Pharr Model in IgorPro

To extract the Oliver Pharr modulus, E_{OP}, and stiffness, S, from the force-indentation data the retract portion of the data is fitted using an inbuilt function in the Asylum Research software which is run with IgorPro. As with the Hertz model fitting the data first has to be line subtracted so that the non-contact portion of the data is 'flat'. After this the contact point is fitted to the approach contact. The software automatically fits the contact point to the retract data in the Oliver Pharr analysis routine which due to the hysteresis in the data is not the initial contact point of the cell. Since the cells are not plastically deformed and

'relax' back to their original height after indentation the contact point is set on the approach data using the same method as for the Hertz model fitting. The power law equation (equation 2.10) is then fitted to the initial 50% of the unloading data as shown in figure 3.13. By differentiating this equation at maximum load and indentation the stiffness, S, is obtained. The stiffness, S, is then substituted into equation 2.11 to calculate the reduced modulus, E_r. This equation also requires the tip-sample contact area which is calculated from equation 2.12 and equation 2.14 as shown in chapter 2 and figure 2.7. This is input into the software via an expansion since the radius of the colloid for the experiment was known. The colloid radius was taken to be the nominal 10 μm quoted by the manufacturer. Once the reduced modulus has been calculated it is then substituted into equation 2.9 along with the tip modulus and Poisson's ratios of both tip and cell to extract the Oliver Pharr modulus, E_r, of the cell.

The values for Oliver Pharr modulus, E_{OP}, and Oliver Pharr stiffness, S, are then copied to an Excel spreadsheet for further analysis which is described in the experimental chapters 4 and 5.

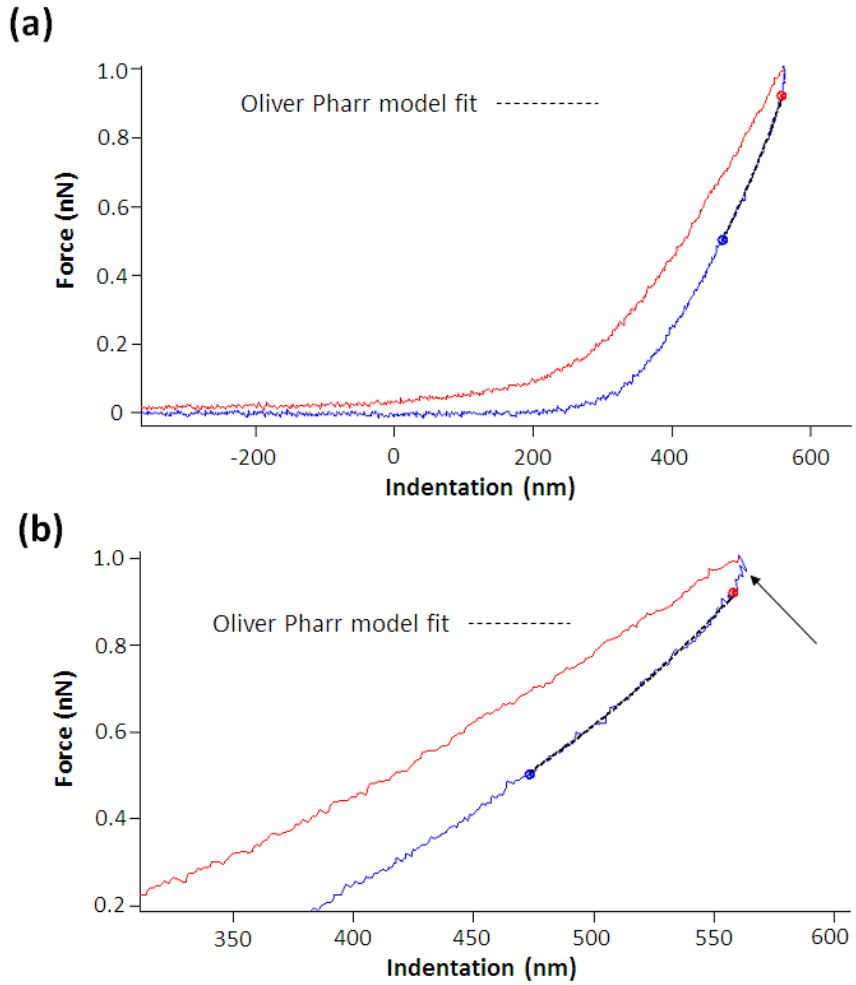

Figure 3.13: Typical graphs showing the region of force-indentation data that is fit using the Oliver Pharr model analysis in the Asylum Research software in IgorPro. The red curves in the graphs are the approach data and the blue curves are the retract data. (a) shows the Oliver Pharr model being fit to the top 50% of the indentation data. (b) is a magnified image of (a) showing at the 'turnaround' point, which is highlighted by the arrow on the graph, there is an initial drop in force which could be due to a slight overshoot in the indentation and/or the viscous properties of the cells. Either way these initial few points are not included in the fitting as they are an artefact of the measurement.

3.4.3 Fitting the Viscoelastic Hertz Model in IgorPro

To extract the apparent viscosity, μ, from the stress relaxation data there was no function in the Asylum Research software so I decided to write a number of functions that fitted an exponential decay curve to the data and extracted the coefficients of this fit. The apparent viscosity extracted from the data gives some indication of the time dependent response of the material being indented, in this case it gives information on the time dependent response of a living cell to an applied load. The exponential fit can be seen in figure 3.14

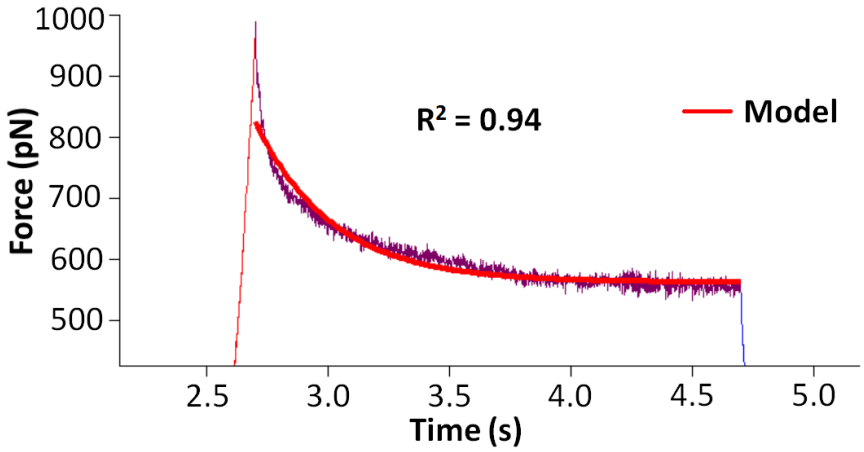

Figure 3.14: A typical graph showing the exponential decay curve being fit to the stress relaxation data over a dwell period of two seconds. Again the red curve to the left is the approach data and the blue curve to the right is the retract data. The purple points which have been fit to are the dwell data.

Three functions were written in total which can be seen in appendix 1 in chapter 8.1. A separate function was written to extract each of the three exponential curve coefficients, y_0, A and τ_ε described below. Each function fitted an exponential decay curve to the data and extracted one of these coefficients separately. By putting equation 2.15 equal to the exponential curve fitting equation:

$$F(t) = y_0 + Ae^{\frac{-(x-x_0)}{\tau_\varepsilon}} \tag{3.1}$$

where $x = t$ and $x_0 = 0$, we get:

$$\frac{4R^{\frac{1}{2}}\delta_0^{\frac{3}{2}}E_R}{3(1-\nu)}(1+\frac{\tau_\sigma-\tau_\varepsilon}{\tau_\varepsilon}e^{\frac{-t}{\tau_\varepsilon}}) = y_0 + Ae^{\frac{-t}{\tau_\varepsilon}} \tag{3.2}$$

The fitting coefficients extracted from the exponential curve fitting are therefore equal to:

$$y_0 = \frac{4R^{\frac{1}{2}}\delta_0^{\frac{3}{2}}E_R}{3(1-\nu)} \tag{3.3}$$

and

$$A = \frac{4R^{\frac{1}{2}}\delta_0^{\frac{3}{2}}E_R}{3(1-\nu)}(\frac{\tau_\sigma-\tau_\varepsilon}{\tau_\varepsilon}) \tag{3.4}$$

which means that

$$\frac{A}{y_0} = (\frac{\tau_\sigma-\tau_\varepsilon}{\tau_\varepsilon}) \tag{3.5}$$

By substituting τ_ε, which is the third coefficient extracted directly from the curve fitting, into the above equation τ_σ can be calculated. All the values necessary to calculate the apparent viscosity, μ from equation 2.16 have now been extracted. These extracted coefficients are then copied to an Excel spreadsheet where the apparent viscosity, μ and other parameters can be calculated.

The data analysis techniques described in this section are used in chapters 4 and 5 of this thesis to extract the mechanical properties of breast cell lines by implementing the mechanical contact models that have been described in the introductory chapter of this thesis. Any further statistical analysis is described in the relevant experimental chapters.

Chapter 4

Mechanical Characterisation of Breast Cancer

4.1 Introduction

This chapter focuses on the development of experimental methods and techniques used in characterising the mechanical properties of living cells using AFM.

Mechanical characterisation of living cells is often performed using the atomic force microscope (AFM) since it allows investigation of cells under near physiological conditions and can be used in conjunction with other techniques such as fluorescence microscopy for cell identification. AFM indentation experiments involve using an AFM cantilever acting as a micro-indenter, to probe either single cells or surgically removed tissues [41, 85] which allows extraction of the cellular and mechanical properties, determined by the response to such interactions.

Cells are commonly modelled as homogeneous, linear elastic bodies using linear elastic models such as the Hertz contact model, even though this is a crude approximation of a cells behaviour which possesses significant active as well as passive

properties. A number of studies now focus on the viscoelastic properties of living cells to further quantify their mechanical properties [47, 86, 50, 87, 88, 89, 49]. This is important since the ability to accurately quantify biomechanical properties of living cells will lead to a greater understanding of cell structure and function. In this chapter, the elastic and viscoelastic properties of benign human breast epithelial cells (MCF-10A), invasive breast cancer cells derived from a primary breast tumour (MCF-7) and highly invasive breast cancer cells derived from a secondary tumour site (MDA-MB-231) were characterised using a number of contact models. This chapter also describes the development of AFM indentation from initial single cell indentations to whole cell force volume mapping and mechanical property characterisation and how the two can be combined and the additional information that can be ascertained from fluorescence microscopy used in conjunction with these AFM techniques.

4.2 Initial Indentation Experiments

Indentation experiments were originally performed using pyramidal shaped cantilevers. Due to the 'sharpness' of the tips on these levers, when indenting the 'soft' surface of the breast cancer cells the pressure gradient exerted on the cells was relatively high compared to colloidal indenters, which can damage the cells and may have an influence on the mechanical properties extracted. The contact area between the tip and cell is also geometrically difficult to estimate with pyramidal tips. Figure 4.1 shows a typical force curve of a single indentation with a pyramidal indenter on an MDA-MB-231 cell. The force required to indent upto nearly a micron in depth of the cell is minimal compared to a colloidal indenter. Sharp pyramidal tips are more suited to probing 'stiffer' materials or particular lo-

calised cell components such as characterising the individual actin filaments within a cell. As the intentions of this study were to characterise the 'bulk' properties of individual cells to compare the mechanical deformability of a number of breast cell lines with varying malignancies, it was thought best to use colloidal probes early on once familiarisation of the experimental routine and calibration had been established.

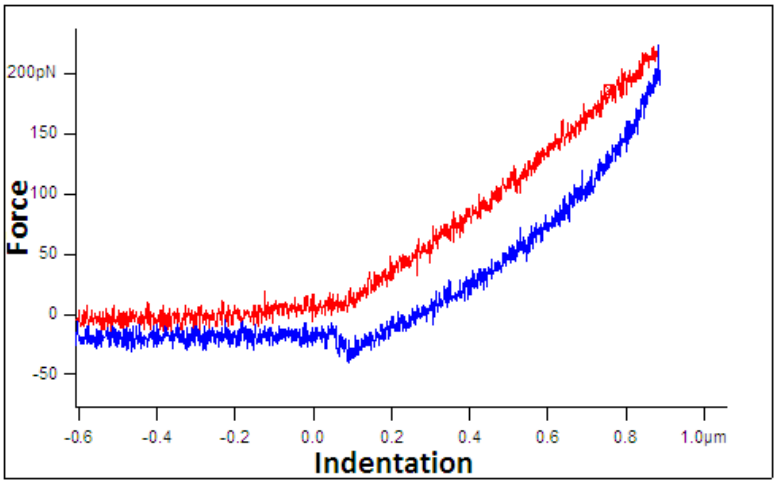

Figure 4.1: Force curve data from a single approach/retract cycle on an MDA-MB-231 cell being indented with a pyramidal shaped tip of spring constant 0.01 $N.m^{-1}$. The red data is the approach data and the blue data is the retract data.

4.2.1 Colloidal Probe Construction

It has been found that it is geometrically simpler to estimate the contact area between the cell and the probe using a colloidal probe compared to a pyramidal indenter. Colloidal probes reduce the pressure gradient applied to the cells compared to a pyramidal tipped cantilever, which makes them less likely to damage the cells during indentation experiments. Colloidal probes also give more of a 'bulk' measurement than a localized measurement as the contact area covers a greater proportion of the cell than a pyramidal/conical tip, which is ideal for investigating

the 'overall' mechanical properties of a cell.

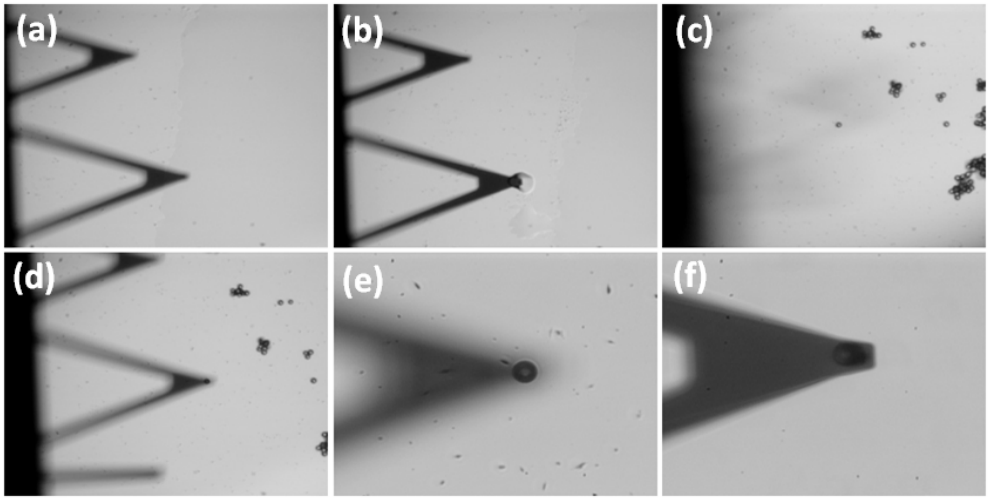

Figure 4.2: (a)-(f)Inverted optical microscope image sequence of a colloidal probe being constructed. (a) is showing the cantilever being lowered towards the glass slide surface with the optical adhesive shown to the right. (b) shows the lever in contact with the optical adhesive. (c) shows the region of glass slide with the polystyrene colloids present. (d) is an image showing the lever being positioned near the chosen polystyrene colloid. (e) shows an increased magnification image to ensure attachment of the colloid is to the correct part of the cantilever. (f) shows the cantilever has been lowered onto the colloid with the colloid positioned directly behind the cantilever tip.

Polystyrene colloids (Polysciences, Inc) with a nominal diameter of 10 μm were attached to v-shaped cantilevers with a nominal spring constant of 0.01 N.m^{-1} using an optical adhesive and curing under UV light. The polystyrene colloids were stored in a glass vial suspended in de-ionised water. A small droplet of suspension was pipetted onto a glass slide and the slide was then left in a glass oven until the water had evaporated off. A small amount of optical adhesive (Norland optical adhesive 81, Cranbury, USA) was then deposited onto the glass slide away from the colloids. Using the inverted optical microscope attached to the AFM, the cantilever was then slowly lowered until the tip was in contact with the optical adhesive. Capillary forces cause the tip and surrounding area

to be immersed in the adhesive. The cantilever was then retracted until it was no longer in contact with the adhesive. Upon retraction the elastic potential energy stored in the cantilever increased until it was sufficient to separate the tip and adhesive, visibly seen as the tip 'sprung' off the surface and went out of focus instantaneously. Once the tip was coated in adhesive the slide was then positioned so that the cantilever was above the colloids. The cantilever was then carefully lowered onto a colloid that was separate from the others. As the cantilever made contact with the colloid a capillary force positioned the colloid in place just behind the tip as shown in the sequence of images in figure 4.2. The cantilever was then retracted and carefully removed from the holder and placed in a gel pack. Long wave UV light (320 - 400 nm) was then used to cure the optical adhesive. The UV light source was left for 10 min to ensure the adhesive was fully cured. The colloidal probe was now ready to be used as an indenter. Figure 4.3 shows SEM images of a colloidal probe constructed using the method described above. SEM images were taken of the initial colloidal probes that were manufactured to ensure that the adhesive was not covering the colloid. Batches of colloidal probes were made on a number of dates for use in AFM indentation experiments.

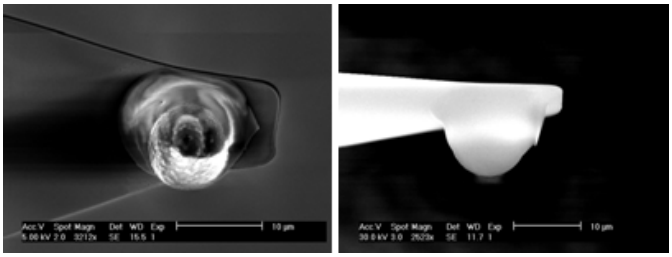

Figure 4.3: SEM images of a 10 μm polystyrene colloid attached to a v-shaped cantilever of nominal spring constant 0.01 N.m^{-1}. Images were acquired by Nic Mullin.

4.2.2 Experimental Development

Initial experiments were performed to investigate the reproducibility of indenting live cells to see what effect, if any, the colloid indentations had on them. An MDA-MB-231 cell was subjected to continuous indentation upto a trigger force of 2.5 nN over the central region of the cell. The indentation rate was set to 0.5 Hz so there was one indentation approach/retract cycle every two seconds.

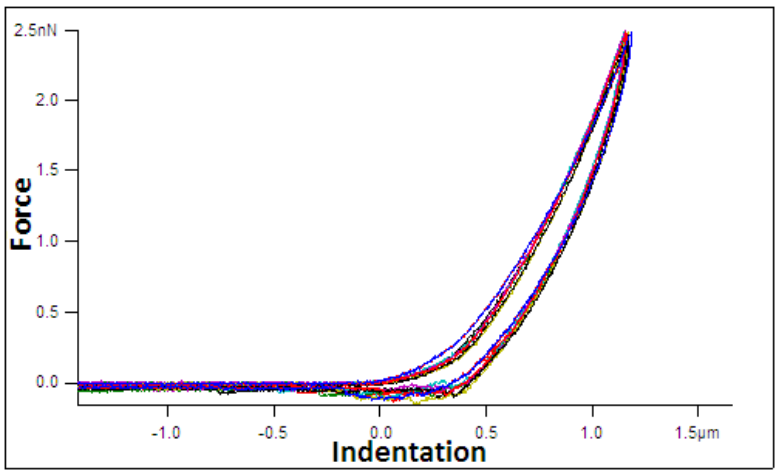

Figure 4.4: Force curve data showing multiple approach/retract cycles over the same point of an MDA-MB-231 cell. From these data taken initially on MDA-MB-231 cells with colloidal probes it was clear that the curves are reproducible below a 0.5 Hz capture rate. By this it is meant that between each pair of force curves (approach and retract) the cell has enough time to relax to its original position.

It is also noticeable when comparing figure 4.1 and figure 4.4 that the force required to indent the cell to a depth of approximately 1 μm is much greater for a colloidal probe than it is for a pyramidal probe, due to the reduced pressure gradient. This reduces the error in the analysis due to effects such as hydrodynamic drag. There is a noticeable difference between the two non-contact regions of the approach and retract force curves shown in these two figures. This is believed to be due to a hydrodynamic force exerted on the cantilever by the cell media. There is also hysteresis between the two contact regions of the approach and

retract force curves for each indentation. This indicates that the indentation is not entirely elastic. There is also a viscous component to the cells being indented which has an impact on the way in which the mechanical properties of the cells can be extracted. The viscous component which shows the cells exhibit time dependent elastic properties meant that it was important that all experiments used to characterise the cells properties were performed at the same velocity and also to the same indentation depth to be able to compare between different cell lines. A rate dependency study was performed as a result of this observation to assess how the loading rate during indentation experiments affected the extracted mechanical values.

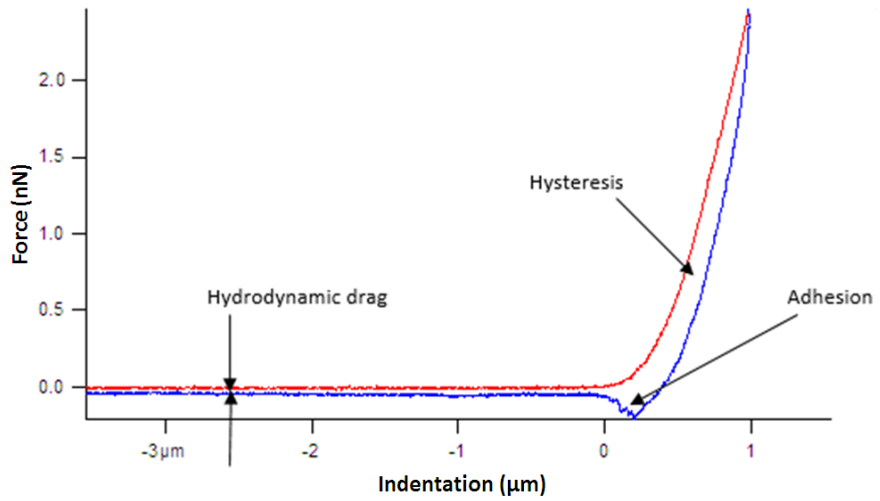

Figure 4.5: Force curve showing the hydrodynamic effect exerted on a cantilever moving through a fluid before and after indenting a living cell. Hysteresis in the piezo could also be contributing systematically to this separation.

In the case of a Newtonian liquid the frictional force is proportional to the velocity, so the separation between the approach and retract data in the non-contact region should increase with approach and retract velocity. To ensure that this separation was indeed due to a hydrodynamic drag force exerted on the lever by the cell medium a number of force curves were taken over a range of

approach/retract velocities. The approach and retract non-contact regions of the curves were fitted with a linear fit in IgorPro to average the approach and retract data and the difference between the two was calculated for a range of velocities. The results showed a linear relationship which confirmed the discrepancy between approach and retract curves was due to hydrodynamic drag on the cantilever moving through the culture medium as shown in figure 4.6.

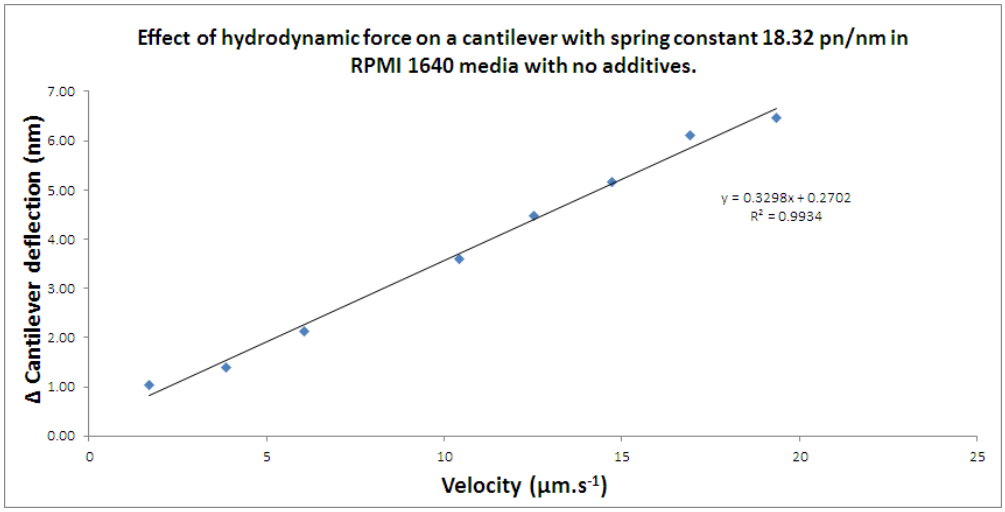

Figure 4.6: A graph showing a linear relationship between the separation between approach and retract force curve data and approach/retract speed of the cantilever. This shows that the force exerted on the cantilever by the cell medium is proportional to the speed of the cantilever through the liquid.

4.3 Initial Force Mapping

When performing indentation experiments on cells in vitro the internal structure of the cell and any effect on the mechanical measurements must be considered. Disrupting the cytoskeleton affects the measured response of an applied load in living cells [90, 91]. It has also been shown that forces applied during AFM experiments can produce spatial rearrangements of internal cell organelles [92] in vitro. It is therefore important to determine which structural cell components may be

contributing towards the mechanical properties extracted from AFM indentation and also to consider the response of the cell to the structural and biochemical effects in such experiments. One way to investigate whole cell mechanics is to use force mapping of entire cells.

Force mapping was initially used here to map the height and morphology of the breast cancer cells as it removed the lateral forces applied to the cell associated with contact mode imaging which can be very damaging to the cells surface when imaging.

4.3.1 Methods

All three breast cell lines cells were grown in 50 x 9 mm petri dishes to more than 50% confluency in the appropriate cell culture medium as described in section 3.2. Cells were washed with PBS and fresh media was added prior to AFM experiments. The Asylum MFP-3D AFM was used to capture force map data for all cell lines investigated in this thesis. The initial force map data shown in figure 4.7 was collected using a 0.01 $N.m^{-1}$ MLCT cantilever with a pyramidal shaped tip.

All other force map data was captured using the same type of lever with a 10 μm polystyrene colloid attached to the lever directly behind the tip as described in section 4.2.1.

The petri dish containing the cell sample was positioned on the XY sample stage of the AFM and the AFM head was lowered until the cantilever was submerged in the cell media in the dish. A clear region of polystyrene dish was then located and a force curve was taken to measure the deflection sensitivity of the cantilever. The spring constant of the cantilever was then calculated as described in section 2.2.3. Once the cantilever properties were obtained the inverted optical microscope was then used to locate cells that were to be mapped. The size of

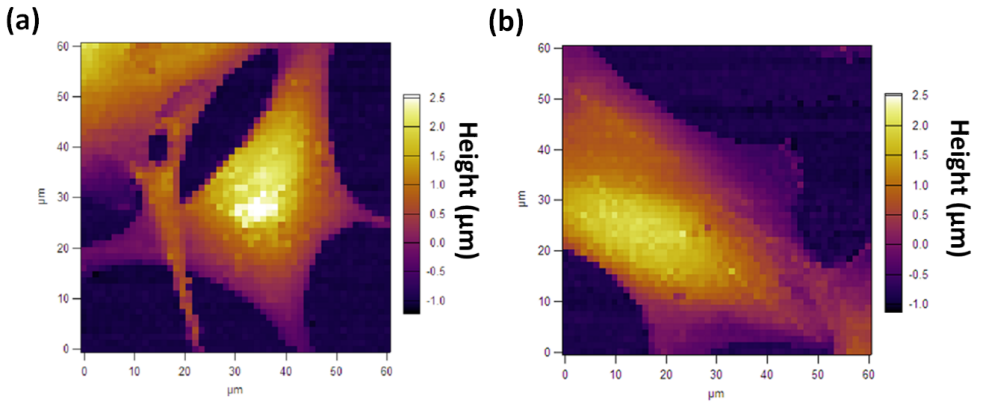

Figure 4.7: Height maps of two MCF-10A cells collected using a pyramidal shaped tip 0.01 N.m^{-1} cantilever. The height is the initial contact point of the tip with the cell and not the indentation depth at triggered force. The triggered force for these two maps was 500 pN at a speed of 9 μm.s^{-1}. (a) and (b) are two separate MCF-10A cells.

the cell was initially estimated and a 10 x 10 or 20 x 20 point force indentation map was taken over the entire cell covering an area of between 40 μm and 70 μm depending on the estimated cell size. Indentations were triggered at 1 nN force, a range of 10 μm and an approach/retract velocity of 10 μm.s^{-1} were the parameters used for each map. The large range was to ensure that the probe and cell fully separated after each indentation point and the velocity used was a trade off between force curve quality and time taken to capture an entire map. Once a 10 x 10 point map was set to the correct size to capture an entire cell with the cell located centrally in the map a greater resolution map was captured, generally 50 x 50 points were taken corresponding to 2500 individual force curves collected over a single cell. Due to the large number of curves each map typically took more than 50 min to complete. Maps were initially taken to investigate the elastic heterogeneity across the surface of each cell to investigate how the mechanical properties of whole cell lines could be characterised using AFM.

Force map data was predominantly acquired for the MDA-MB-231 cell line

as these cells generally remained viable for the longest amount of time after being removed from the humidified incubator. Typically MDA-MB-231 cells were 'mapped' for upto three h after being removed from the incubator before their viability was questioned due to cells appearing to begin to 'round up' in the dishes.

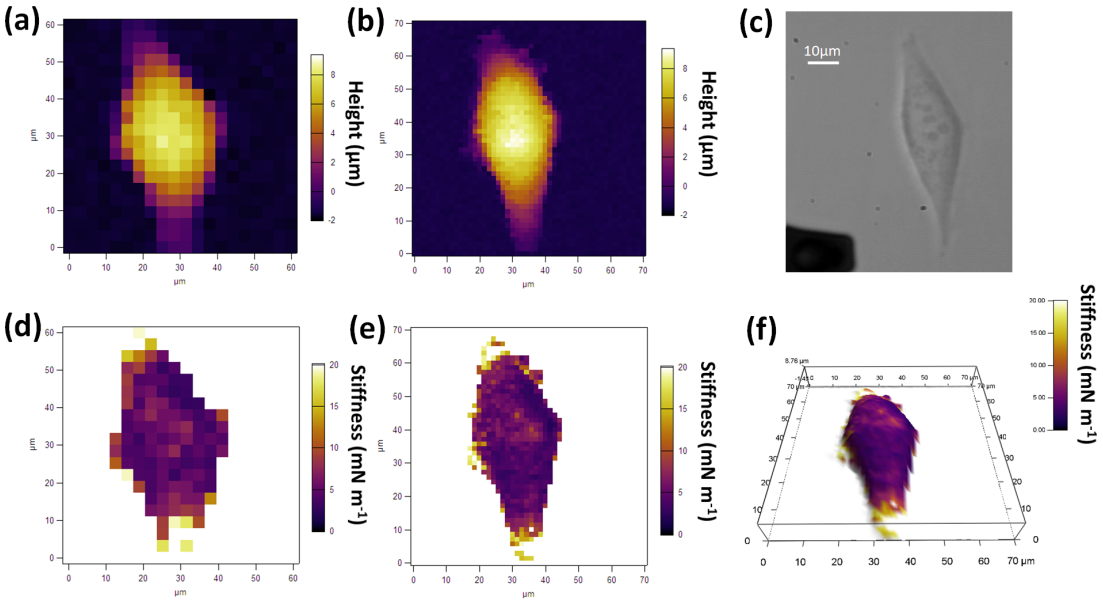

Figure 4.8: (a) A 20 x 20 force map showing height data for a single MCF-7 cell. The height is taken from the initial point of contact with the cell. The 20 x 20 point map data was initially taken to centralise the cell in the map before the resolution and map area was increased. (b) A 60 x 60 force map showing the height data for the same cell. (c) A bright-field image of the MCF-7 cell being investigated. (d) A 20 x 20 point force map showing measured retract stiffness of the MCF-7 cell. (e) A 60 x 60 force map showing retract stiffness of the MCF-7 cell. (f) A 3D height map of the cell with the stiffness data overlaid.

4.3.2 Analysis

All force map data was analysed using IgorPro 6.2 (Wavemetrics, Inc.) software with the Asylum Research MFP-3D offline analysis package(version MFP-3D 120804+1821). IgorPro is an open source software package which allowed code to be edited/written to analyse the force maps. The software usually extracts the

triggered indentation depth for each force curve in a map to produce a height map of the data, which doesn't actually show the topography of the cell as the indentation depth at a particular force is dependent upon the underlying structure of the cell. It was thought to be more appropriate to use the contact point as the height of the cell. Ross Carter, a fellow PhD student in my group at the time, took the code from the Hertz fitting routine in the software which goes through the non-contact data to find the contact point and applied it to the original height map routine to produce height maps which extract the contact point from each force curve in a map to produce a height map of the cells. The code can be seen in appendix 1. The retract stiffness was also extracted from each force curve to produce a stiffness map of each cell. This fits a straight line to the force versus indentation initial retract curve data. I myself wrote a routine which extracted the slope of the retract curve data and an if statement was included in the code which changed any negative stiffness values to 0.02 $N.m^{-1}$ as this is the nominal maximum stiffness value of the MLCT cantilever stated by the manufacturer (Bruker). This code can also be seen in appendix 1. The negative values arise from the force curves acquired on the polystyrene petri dish surface. As this surface is used to calibrate the cantilever initially it can produce negative stiffness values for subsequent force mapping data. These negative values appear as dark regions with the colour scale implying they are softer than the cancer cells being investigated, which is why they are set to 0.02 N as this inverts the colour showing that they are considerably stiffer than the cells.

4.3.3 Results

Force map results showed elastic heterogeneity across the surface of the cells. Specific regions of the cells repeatedly showed increased stiffness compared with

the rest of the cell surface. Thinner regions near the cell edges tended to appear to be stiffer than regions in the centre of the cell which was probably due to a greater contribution of the measurement coming from the dish beneath the cell as these thinner regions are shown to be only a few hundred nanometres in thickness, see figure 4.9.

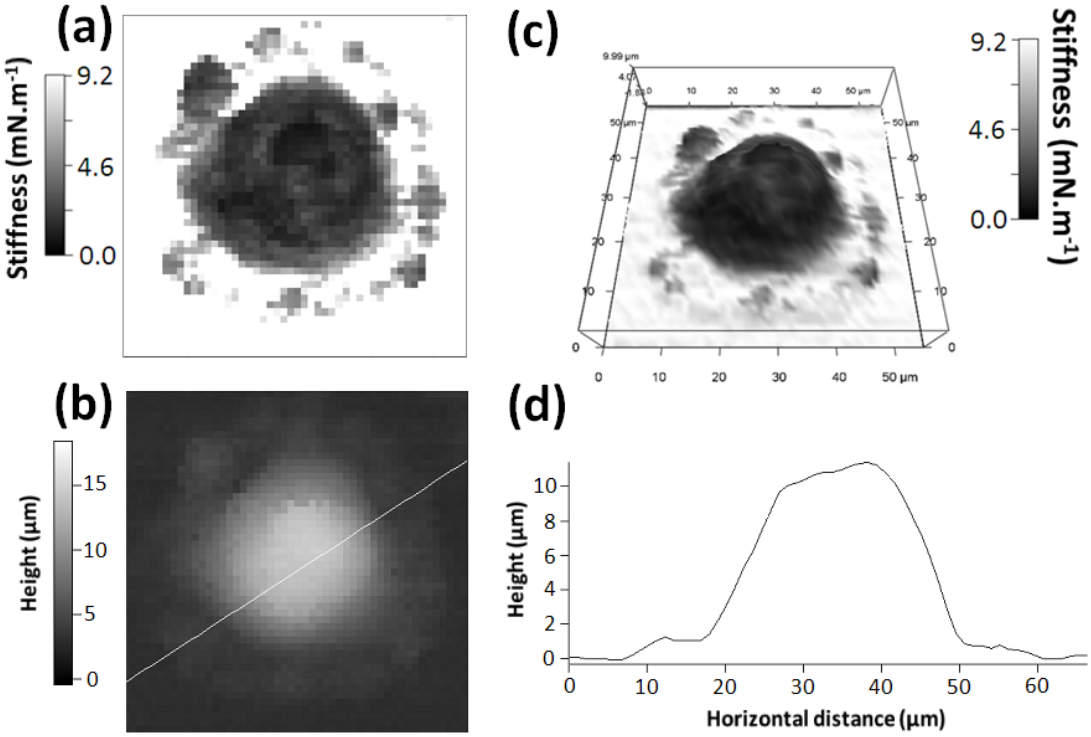

Figure 4.9: (a) Force map showing stiffness data. (b) Force map showing height data. The map also shows a line depicting the cross section shown in (d).(c) A 3D representation of the contact point data which yields a height map of the cell. The colour scale represents the retract stiffness data with increasing stiffness from dark to light. (d) A cross section through the cell shows the height of the cell on a chart.

When comparing the stiffness maps the extend and retract data were initially looked at. Figure 4.10 shows two stiffness maps showing data extracted from force curves from a single MDA-MB-231 cell. One map fits a straight line to the approach data and the second fits a straight line to the retract data. On first

appearance the two look very similar. The stiffness values for the approach data are much lower than for the retract data. This is believed to be due to a viscous component being indented in the approach data. By the time the indenter retracts the viscosity of the cell has dissipated and the retract stiffness measurement is much more of an 'elastic' measurement of the cell.

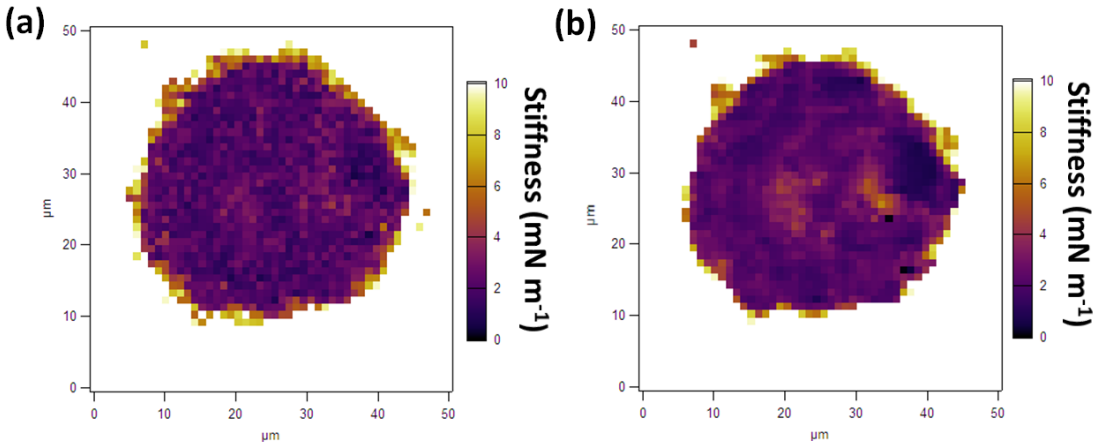

Figure 4.10: (a) Approach and (b) retract stiffness maps of a single MDA-MB-231 cell. The approach data appears to show a 'softer' cell than the retract data. This is likely due to the viscous component of the initial indentation.

Extracting the retract data in the maps was thought to reduce the viscous contribution to the data and be predominantly a measure of the underlying elastic components of the cell such as the cytoskeletal components, for instance, actin filaments and microtubules. By doing this it was thought that the properties of intra-cellular components could be extracted, but it would be necessary to identify the cell component while simultaneously extracting mechanical information. Initially brightfield images were taken in conjunction with mechanical force mapping data and the two sets of information were compared to see if 'stiffer' regions in the force maps corresponded to particular regions in the brightfield images. It was noticed that the main organelle which could be solely identified without any labelling was the cell nucleus and usually the nuclear membrane in which the

nucleus is contained which the effect of can be seen in figure 4.11.

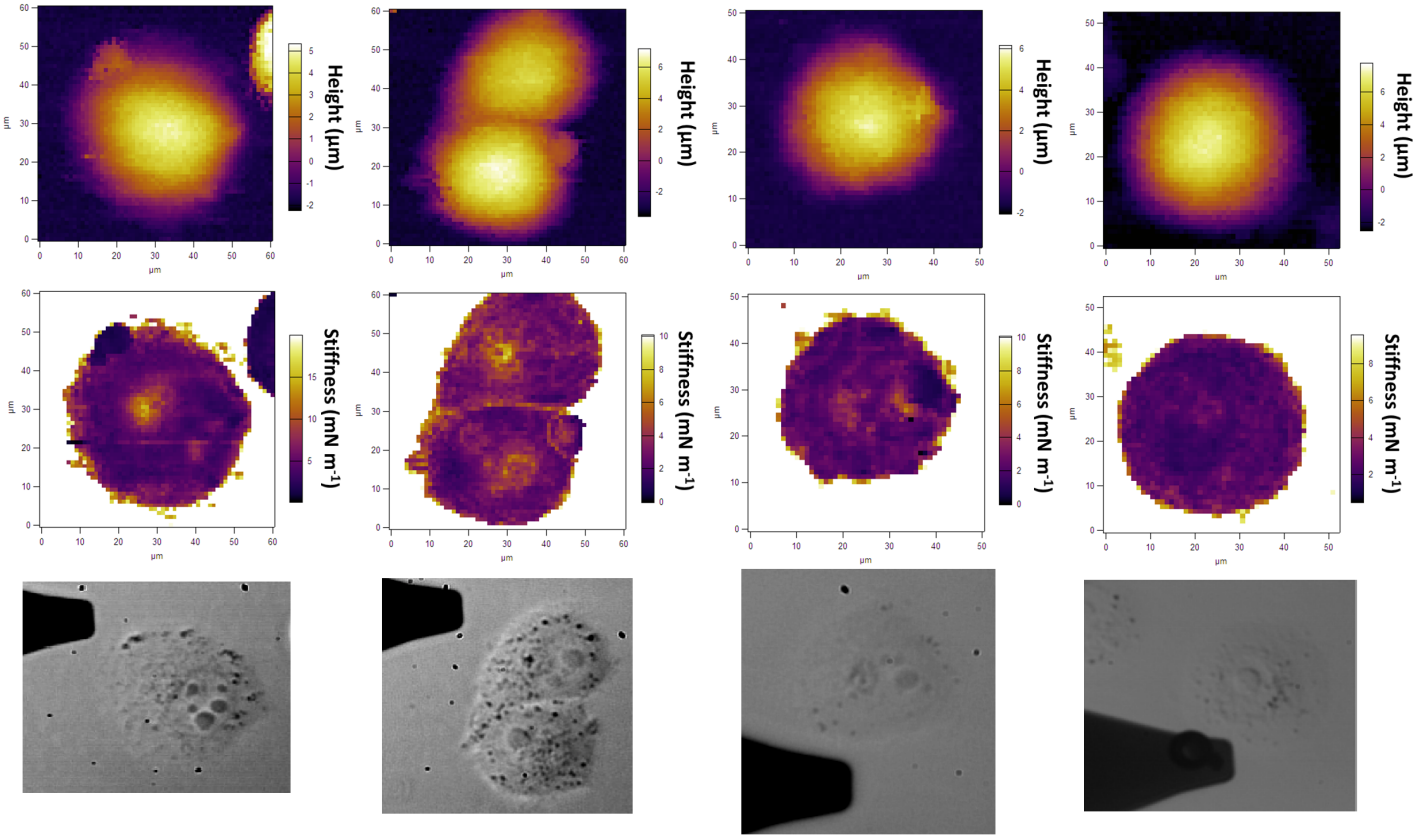

Figure 4.11: Multiple height, stiffness and bright-field data for four single MDA-MB-231 cells. Maps show heterogeneity across the surface of each cell where the 'stiffest' regions appear to correlate with organelles in the bright-field images.

The nucleus generally corresponded to a 'stiff' region in the maps when compared to the immediate surrounding nuclear membrane region. Other 'stiffer' regions shown in the force map data seemed to correspond to densely clustered organelles within the cell. One method to be able to identify these organelles is to use fluorescence microscopy in conjunction with force mapping.

4.4 Force Mapping in Conjunction with Fluorescence Microscopy

Preliminary force mapping data showed that the surface of the cells investigated using AFM indentation experiments were elastically heterogeneous. This heterogeneity appeared to arise from intracellular components contributing to the indentation data extracted from the whole cell force maps. To further investigate the contribution of these cellular structures fluorescence microscopy was used in conjunction with whole cell force mapping using AFM to determine any correlation between measured cell stiffness and the localisation of cellular organelles.

4.4.1 Methods

Initially MDA-MB-231 cells were grown in 50 x 9 mm dishes and stained with MitoTracker Green 250 nM (Invitrogen, UK), for a period of 30 min at 37°C and 5% CO_2. Due to the thickness of these polystyrene dish bottoms the maximum resolution lens that could be used was a 40 x objective lens in air which didn't give enough resolution to determine what part of the cell was fluorescing. This can be seen in figure 4.12

To increase the resolution of the fluorescence data glass bottom dishes were made so that a 60 x oil immersion lens could be used. 50 x 9 mm polystyrene

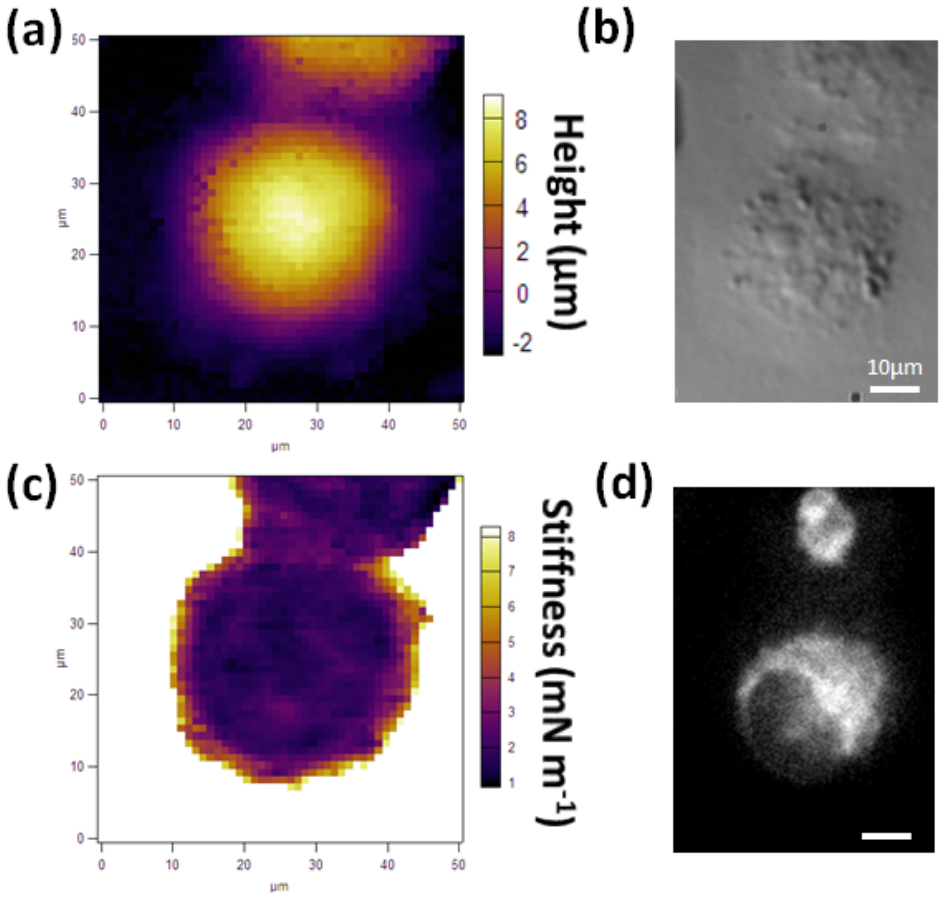

Figure 4.12: (a) is a force map showing height data from a single MDA-MB-231 cell. (b) shows the bright-field image of the cell. (c) is a force map showing the retract stiffness data for the MDA-MB-231 cell. (d) is the fluorescence image of the cell with active mitochondria labelled with MitoTracker.

petri dishes (Falcon BD, Invitrogen) were used and a 18 mm x 30 mm rectangular hole was cut out the bottom of the dishes. Rectangular glass cover slips were then cut to 20 mm x 32 mm using a diamond tipped scribe. Two 1 mm x 32 mm and two 1 mm x 20 mm strips of parafilm (Sigma-Aldrich) were positioned around the hole on the bottom of the dish and the glass cover slip was placed over the hole exactly over the parafilm strips. A soldering iron was then used to melt the parafilm between the polystyrene dish and glass coverslip holding the glass in place. The parafilm provided a non-toxic sealant for attaching the glass cover

slips to the bottom of the dishes. The outside edge of the glass coverslip was then sealed with DPX to ensure the bottom of the dish was completely watertight.

MDA-MB-231 cells plated in 'in house' glass bottom dishes (50 x 9 mm dishes, University of Sheffield, with cover glass attached) were stained with MitoTracker Green 250 nM (Invitrogen, UK), for a period of 30 min at 37°C and 5% CO_2. The glass bottom dishes were used to allow fluorescence imaging. MitoTracker Green is a dye containing a mildly thiol-reactive chloromethyl moiety for labelling active mitochondria (Invitrogen, UK). After staining the media was replaced and force maps were then taken over 50 x 50 grids covering the whole cell using the AFM to investigate how the mechanical properties varied over the cell surface. An indentation speed of 10 μm.s^{-1} was used so that force map data could be collected in under an hour for each cell. Fluorescence images were simultaneously acquired with the force maps to determine whether the mechanical properties correlated with the location of active mitochondria.

4.4.2 Results

Data are presented in the form of simultaneous images taken of single cells as shown in figure 4.13. The images consist of a bright field image, a fluorescence image and a force map showing retract stiffness data which is proportional to the elastic modulus. All images have identical scale, thus allowing direct comparisons. The fluorescence and bright-field image were captured using the same camera with the sample being in exactly the same position for both. These two images were overlaid and cropped so that they represent the exact same area of the sample. The scale of these images was then calculated by dividing the size of a single camera pixel by the magnification of the objective lens being used (60 x). This gave a length measurement per image pixel. This fraction along with the number of

pixels per image was used to create the 10 μm scale bar used in the bright-field and fluorescence images. Elastic modulus values were extracted from representative points on the map to show the elastic heterogeneity of the cells surface and how that corresponds to the spatial distribution of intracellular components.

The two points chosen in figure 4.13 depicted by the red and black markers were analysed by extracting the elastic modulus from the corresponding force curves using both the Hertz and Oliver Pharr models following the data analysis methods described in section 3.4. Oliver Pharr analysis gives E_{OP} values of 595 Pa and 275 Pa for the black and red curves respectively. Hertzian analysis yields E_{Hertz} values of 216 Pa and 86 Pa for the black and red curves respectively. The black marker appears to be over a region containing the nucleolus when directly comparing the stiffness map with the bright-field image. The red marker appears to be indenting a region of the cell surface with the nuclear membrane beneath it. The elastic modulus values show more than a factor of two difference between these two regions with the nucleolus being the 'stiffer' of the two regions. The fluorescent image showing the location and spatial distribution of active mitochondria also appears to correlate with regions of densely clustered organelles in the bright-field image which again correlate with lighter regions in the stiffness map, indicating that regions containing more intracellular components appear stiffer as these organelles seem to be contributing to the measurements being made. It may be the case that these organelles themselves are not 'stiffer' as implied, but rather they contribute to a measurement of the combined cell structure including the cells cytoskeleton, membrane and the organelles themselves which may be 'trapped' within the mesh-like cytoskeleton. The experiments also show that towards the edge of the cell there is a significant contribution to measured stiffness from the underlying substrate. The results of these experiments indicated it is important

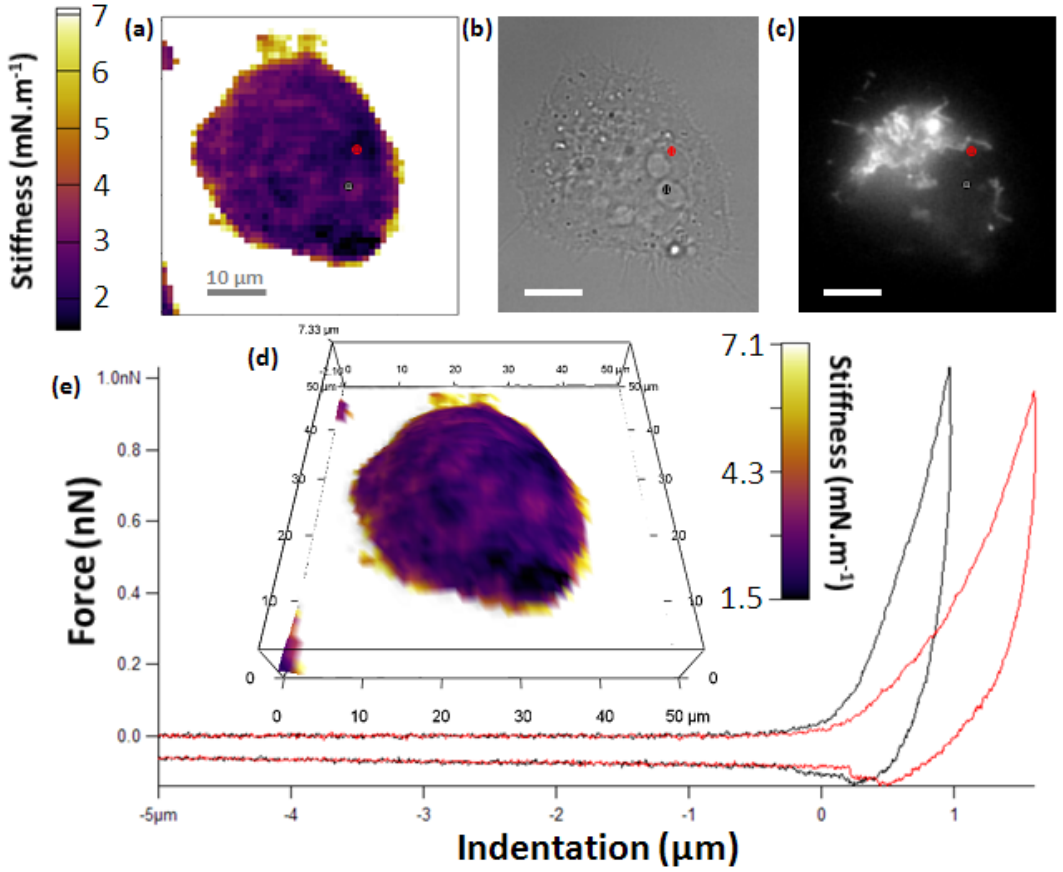

Figure 4.13: Comparison between AFM force data, bright field and fluorescent microscope images of a single MDA-MB-231 cell that has been stained for active mitochondria. (a) 50 x 50 retract stiffness map of a single MDA-MB-231 cell. (b) Bright field optical microscope image of the same cell. (c) Fluorescence microscope image of the cell. (d) 3D map of the contact point of each indentation representing the height of the cell with the retract stiffness data overlaid. The black and red markers in (a)-(c) correspond to the black and red force curves shown in (e). Elastic moduli values were calculated for both curves. Oliver Pharr analysis gave values of 595 Pa and 275 Pa for the black and red curves respectively. Hertzian analysis yielded the values 216 Pa and 86 Pa for the black and red curves respectively. Scale bars in (a)-(c) represent 10 μm.

to take multiple measurements over the cell surface to obtain a true average value for each cell, thus a total of 16 points over a 4 x 4 point grid were taken over the centre of the cell for the remainder of the experiments.

4.4.3 Discussion

It has been shown here that force mapping experiments may be able to investigate even deeper into the structure of living cells than has previously been shown. Mechanical properties of intracellular organelles could possibly be extracted from these experiments which may have important implications in disease diagnosis and treatment. In figure 4.13(a) at the bottom right hand corner the darker region represents a 'softer' region of cell which appears to correlate with a spreading region in the bright field image (figure 4.13(b)) and a raised 'bleb' in the 3D image (figure 4.13(d)). Blebbing has been shown to be involved in cell motility. Not only can cells migrate by means of actin polymerisation extending their membranes outwards, they have been shown to use myosin based blebbing along with cytoplasmic flow to migrate in specific directions [93]. Force mapping in conjunction with fluorescent imaging could be a useful tool to investigate this process in physiological conditions and could lead to a greater understanding of enhanced cell motility in the progression of cancer and other diseases. Previous studies have highlighted the importance of cell motility in carcinogenesis by studying relatively 'soft' labelled MDA-MB-231 cells migrating through 'stiffer' MCF-10A cells in a co-culture system [9]. The loss of E-cadherin in MDA-MB-231 cells increased their motility between benign MCF-10A cells, whereas MCF-7 cells expressing E-cadherin did not show this increased migratory behaviour.

It is well reported that a cell's cytoskeleton contributes greatly to its measured mechanical properties. In the force mapping experiments presented here it

is shown that elastic heterogeneities over the surface of a cell appear to arise from the organisation of intracellular components. It is possible that these organelles are held in position between a mesh like cytoskeletal structure and are thus contributing to the mechanical properties extracted from indentation experiments. Force mapping in conjunction with fluorescence imaging has great potential in characterising whole cell mechanical properties.

4.5 Parental Cell Line Mechanical Property Characterisation

4.5.1 Mechanical Characterisation Cell Setup

The aim of this section of work was to characterise 3 breast cell lines of varying malignancy to see whether metastatic potential correlated with the measured mechanical deformability of the cells. For these indentation experiments the cells were cultured in 50mm x 9mm polystyrene dishes (BD Falcon) for 24, 48 and 168 h for MDA-MB-231, MCF-7 and MCF-10A cells respectively. This was to ensure that due to the differing proliferation rates the cell samples were all in their exponential growth phase during indentation experiments. All cell lines were cultured in their appropriate media as described in the cell culture section in chapter 3.

4.5.2 Characterisation Elasticity Measurements

All AFM measurements were obtained using an MFP-3D atomic force microscope (Asylum Research) integrated with an inverted optical microscope (Olympus microscope IX71, Tokyo, Japan). To ensure cell viability and stability, studies were performed with the cells in their appropriate culture media, within 3 h of removal

from the humidified incubator and performed at room temperature. The colloidal probe cantilever spring constant, k, was calibrated before each experiment using the thermal tune method [33] using the Asylum software as described in section 2.2.3 of chapter 2. In the software a correction factor is performed where the DC noise is subtracted from the measured displacement of the cantilever due to thermal excitation, before integration to give the value for the cantilever spring constant, k. The deflection sensitivity was determined on the petri dish in the cell media. All measured cantilever spring constants were within the range specified by the manufacturer (0.005-0.02 $N.m^{-1}$) and a new colloidal probe was used for each experiment.

For each experiment up to 25 cells were indented and at least 3 experimental repeats were performed on each cell line. Each cell was first located using the inverted optical microscope, following which the colloid was positioned over the central region of that cell. Force maps were taken over 4 x 4 point grids over the central region of the cell as depicted in figure 4.14 corresponding to an area of the cell between 5 μm^2 and 15 μm^2 dependent upon cell size and morphology.

A constant indentation velocity of 3 $\mu m.s^{-1}$ was used which was sufficiently slow to minimise the hydrodynamic force exerted on the cantilever from the media, but fast enough to represent a sudden indentation to allow investigation of the cells elastic properties. A constant trigger force of 1 nN was used throughout the experiments corresponding to indentations between 120 nm and 3 μm depending on both the cell line and the variations in the mechanical properties within each cell. A constant indentation speed and trigger force was used throughout to ensure the loading rate was constant as possible so that any loading rate dependent changes in mechanical properties were kept to a minimum (see section 4.5.5). The parameters used in this study resulted in a loading rate of 6.3 $\pm$ 2.0 $nN.s^{-1}$, 2.7

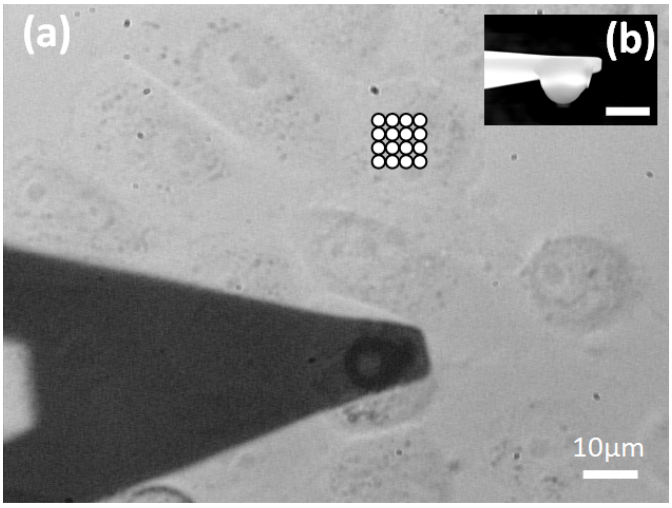

Figure 4.14: (a) An optical microscope image of a colloidal probe AFM cantilever positioned over the central region of an MDA-MB-231 cell. The 4 x 4 grid shown over one of the confluent cells is a pictorial representation of the force map area used to characterise the mechanical properties of the cells. (b) SEM image of the colloidal probe. A 10 μm polystyrene colloid is shown attached to the cantilever. It can be seen that the cantilever tip does not protrude below the colloid. Scale bar represents 10 μm.

$\pm$ 0.8 nN.s^{-1}, 3.9 $\pm$ 1.1 nN.s^{-1}, and 3.6 $\pm$ 0.8 nN.s^{-1} (median $\pm$ median absolute deviation) used for the MCF-10A, MCF-7, MDA-MB-231 and MDA-MB-231 in MCF-10A media cells respectively. This loading rate varied by approximately a factor of two across the different cell lines due to the difference in elasticity of the cells being investigated. The same approach of 6 μm was used throughout with the fixed speed of 3 μm.s^{-1}, with a sample frequency of 0.25 Hz used for each set of approach/retract curves captured for the characterisation study.

4.5.3 Characterisation Stress Relaxation

Force maps were then repeated over the same central cellular area with a two second dwell of the z-scanner position, to quantify the stress relaxation behaviour of the cells in response to a step displacement. The z-scanner position was held constant when the 1 nN trigger force was reached to measure the decay in force

as a function of time between the probe and the cell.

4.5.4 Rate Dependency

In viscoelastic materials, loading rate is an important parameter which may substantially affect the measurements made. Below is described an experiment carried out to ascertain whether inherent variation in loading rate, due to changes in sample stiffness and the fact that AFM data is typically collected at a pre-determined rate of the base of the cantilever to the surface, may have impacted on the data presented in this chapter.

A single MDA-MB-231 cell was located using the inverted optical microscope, following which the colloidal probe was positioned over the central region of that cell. Force maps were taken over a 4 x 4 point grid across the central region of the cell corresponding to an area of 10 μm^2. A force map was collected for a range of indentation velocities between 0.5 $\mu m.s^{-1}$ and 12 $\mu m.s^{-1}$ (0.5, 1, 2, 4, 6, 8, 10 and 12 $\mu m.s^{-1}$). This range of velocities corresponded to a frequency of between 0.04 Hz and 1 Hz and a loading rate of between 0.5 $nN.s^{-1}$ and 21.6 $nN.s^{-1}$. A constant trigger force of 1 nN was used throughout the experiment. The loading rate was calculated by dividing the triggered loading force of 1 nN by the indentation at maximum load divided by the approach/retract velocity. A force map was taken with and without a two second dwell, at each indentation velocity. A second identical experiment was repeated immediately, without moving the sample, allowing the same region to be monitored a second time (This is indicated by Run 1 and Run 2 in the results). Hertz modulus, Oliver Pharr modulus and apparent viscosity values were calculated for each force map point as described in section 3.4 of chapter 3.

4.5.5 Rate Dependency Results

The loading rate was calculated for each indentation and plotted against the calculated Hertz modulus, Oliver Pharr modulus and viscosity values respectively. The results are shown below in figure 4.15.

The results show that the three models used to extract mechanical properties from the approach/retract data do show some indication of being rate dependent. This dependency, however, is minimal over the range of loading rates applied in this experiment. Due to these results the loading speed and trigger force was again held constant throughout all subsequent experiments to reduce the variation in loading rate as much as possible. However, loading rate is dependent on the cell stiffness, so it becomes very difficult to indent at a constant loading rate using the conventional AFM geometry.

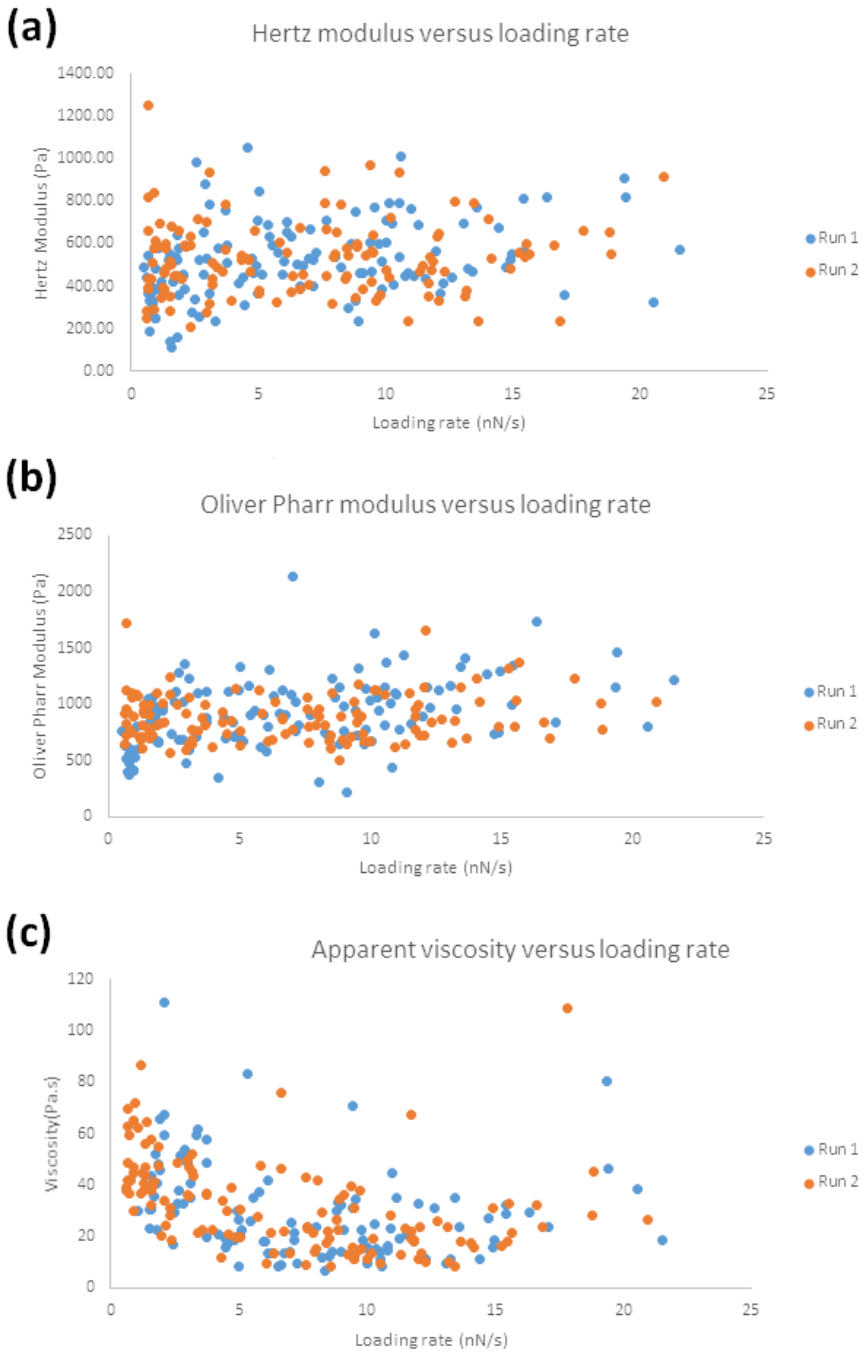

Figure 4.15: (a) A graph showing the Hertz modulus dependency on loading rate. (b) A graph showing the Oliver Pharr modulus dependency on loading rate. (c) A graph showing the dependency of measured apparent viscosity on loading rate.

4.5.6 Data Analysis

AFM experiments to characterise the breast cell lines were conducted on at least 3 different days for all cell lines investigated. The Hertz model, Oliver Pharr model and viscoelastic models as described in section 2.2.4 were fitted to the respective data acquired from the indentation experiments following the fitting procedures described in section 3.4 of chapter 3.

4.5.7 Results

The mathematical models fit the data well for the Hertz ($R^2 = 0.98 \pm 0.02$), Oliver Pharr ($R^2 = 0.99 \pm 0.01$) and viscoelastic ($R^2 = 0.96 \pm 0.02$) tests suggesting that the experimental data are described relatively well by the three theoretical models. Individual cell line model fitting data is shown in table 4.1.

Table 4.1: Comparison of the fitting of the mathematical models to the data. Data is represented as mean ± standard deviation.

	MCF-10A	MCF-7	MDA-MB-231
Hertz model R^2	0.973 ± 0.014	0.988 ±0.012	0.986 ± 0.021
Oliver Pharr model R^2	0.994 ± 0.004	0.995 ± 0.007	0.996 ± 0.006
Viscoelastic R^2	0.940 ± 0.012	0.970 ± 0.008	0.962 ±0.030

4.5.8 Hertz Elasticity

To obtain an average value for the E_{Hertz} elastic modulus parameter, 16 measurements were recorded for each cell at different locations, and at least 50 cells were recorded for each cell line. This allows both cell surface heterogeneity due to internal cell structure and cell sample heterogeneity to be evaluated. This dataset is represented as a histogram which demonstrates the distribution of modulus values

Table 4.2: Comparison of the biomechanical properties for the three breast cell lines investigated. Data is represented as median ± median absolute deviation.

	Property	MCF-10A	MCF-7	MDA-MB-231
Hertz elasticity	E_{Hertz}(kPa)	0.63 ± 0.47	0.18 ± 0.08	0.24 ± 0.09
Oliver Pharr elasticity	E_{OP} (kPa)	1.30 ± 0.05	0.57 ± 0.15	0.57 ± 0.16
	Stiffness ($mN.m^{-1}$)	7.0 ± 2.0	4.5 ± 0.9	4.5 ± 1.0
Viscoelasticity	$E_{relaxed}$ (kPa)	0.24 ± 0.17	0.08 ± 0.04	0.17 ± 0.08
	$E_{instantaneous}$ (kPa)	0.39 ± 0.21	0.13 ± 0.06	0.24 ± 0.10
	E_{young} (kPa)	0.37 ± 0.25	0.12 ± 0.06	0.26 ± 0.12
	μ (Pa.s)	58 ± 30	22 ± 9	29 ± 11

Table 4.3: The biomechanical properties for the MDA-MB-231 cells cultured in MCF-10A media. Data is represented as median ± median absolute deviation.

	Property	MDA-MB-231 in MCF-10A media
Hertz elasticity	E_{Hertz}(kPa)	0.30 ± 0.12
Oliver Pharr elasticity	E_{OP} (kPa)	0.46 ± 0.12
	Stiffness ($mN.m^{-1}$)	3.2 ± 0.5
Viscoelasticity	$E_{relaxed}$ (kPa)	0.16 ± 0.06
	$E_{instantaneous}$ (kPa)	0.20 ± 0.06
	E_{young} (kPa)	0.25 ± 0.09
	μ (Pa.s)	19 ± 5

for each specific cell line as shown in figure 4.16.

All Hertz elastic data distributions are positively skewed and can be described as log normal distributions. Average E_{Hertz} values stated are median values plus or minus the median absolute deviation where the deviation represents the spread in the distribution of the data. For the cell lines investigated the average E_{Hertz} values obtained for the Hertz fitting are 0.63 ± 0.47 kPa, 0.18 ± 0.08 kPa and 0.24 ± 0.09 kPa (median ± median absolute deviation) for the MCF-10A, MCF-7 and MDA-MB-231 respectively as shown in table 4.2.

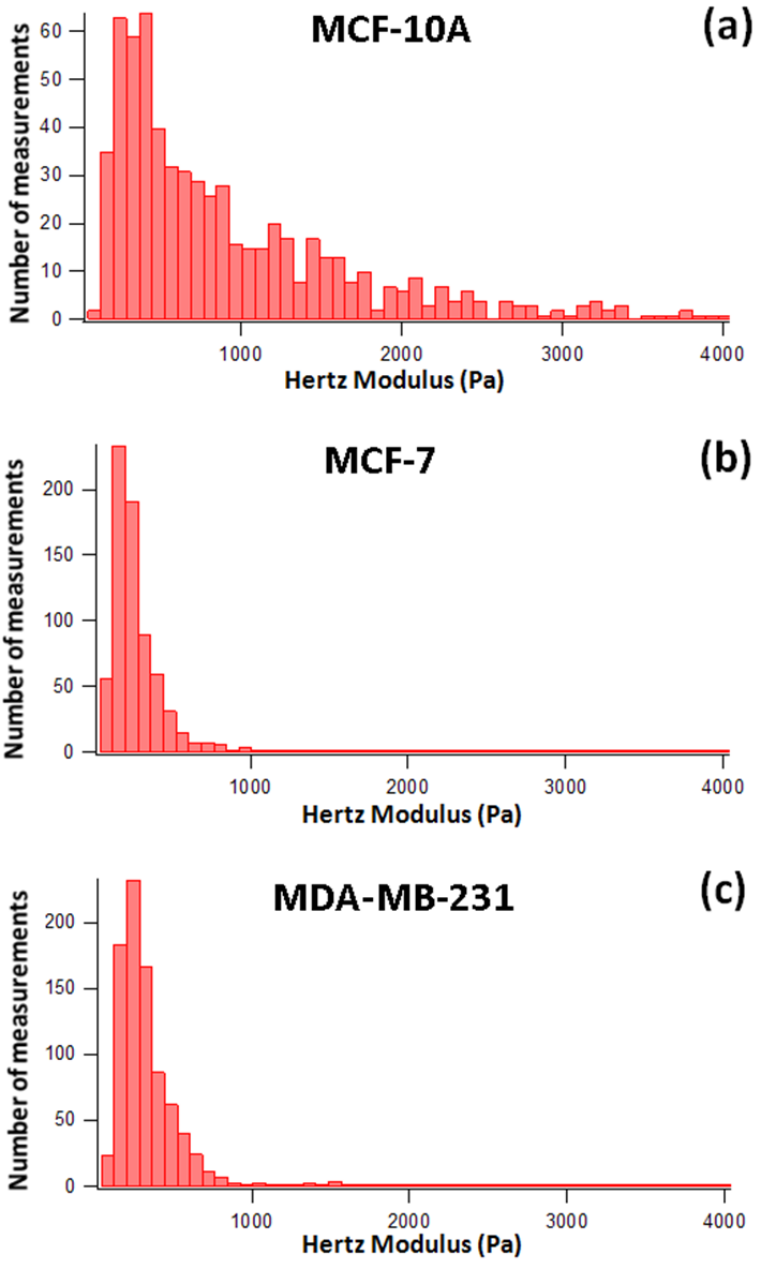

Figure 4.16: (a)-(c) Histograms showing the distribution of Hertz elastic moduli for MCF-10A cells (a), MCF-7 cells (b) and MDA-MB-231 cells (c).

4.5.9 Oliver Pharr Elasticity

To obtain an average value for the E_{OP} elastic modulus parameter, 16 measurements were recorded for each cell at different locations, and at least 50 cells were recorded for each cell line. This allows both cell surface heterogeneity due to internal cell structure and cell sample heterogeneity to be evaluated. This dataset is represented as a histogram which demonstrates the distribution of modulus values for each specific cell line as shown in figure 4.17.

All Oliver Pharr elastic data distributions are positively skewed and can be described as log normal distributions. Average E_{OP} values stated are median values plus or minus the median absolute deviation where the deviation represents the spread in the distribution of the data. For the cell lines investigated the average E_{OP} values obtained for the Oliver Pharr fitting are 1.30 $\pm$ 0.54 kPa, 0.57 $\pm$ 0.15 kPa and 0.57 $\pm$ 0.16 kPa (median $\pm$ median absolute deviation) for the MCF-10A, MCF-7 and MDA-MB-231 respectively as shown in table 4.2).

4.5.10 Hertz Viscoelasticity

To obtain an average value for the apparent viscosity for each cell line, μ, extracted from the viscoelastic model fitting of the stress relaxation data, the same number of measurements is taken for each cell as previously stated. The dataset is represented as a histogram showing the distribution of apparent viscosities for each cell line as shown in figure 4.18.

All apparent viscosity distributions were positively skewed and can be described as log normal distributions. Average viscosity values stated are median values plus or minus the median absolute deviation. Average apparent viscosity values, μ, for the cell lines were 58 $\pm$ 30 Pa.s, 22 $\pm$ 9 Pa.s and 29 $\pm$ 11 Pa.s for the MCF-10A, MCF-7 and MDA-MB-231 cells respectively. The Wilcoxon Rank

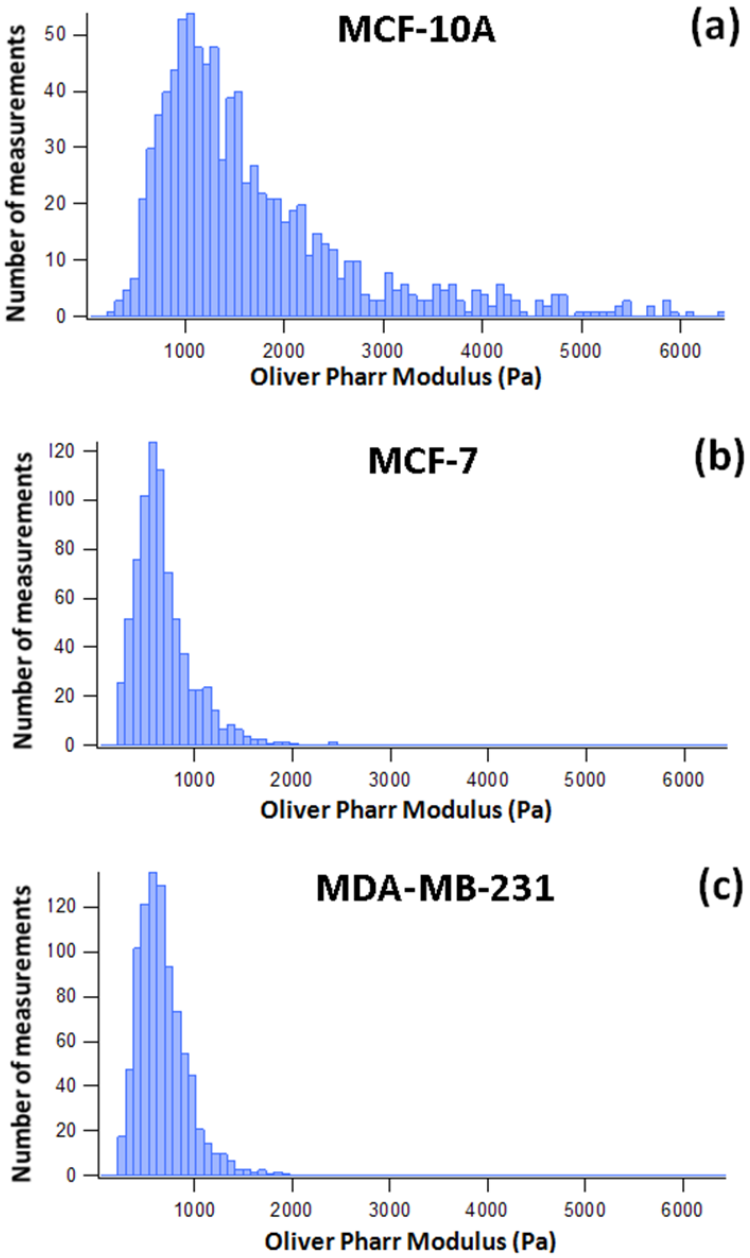

Figure 4.17: (a)-(c) Histograms showing the distribution of Oliver Pharr elastic moduli for MCF-10A cells (a), MCF-7 cells (b) and MDA-MB-231 cells (c).

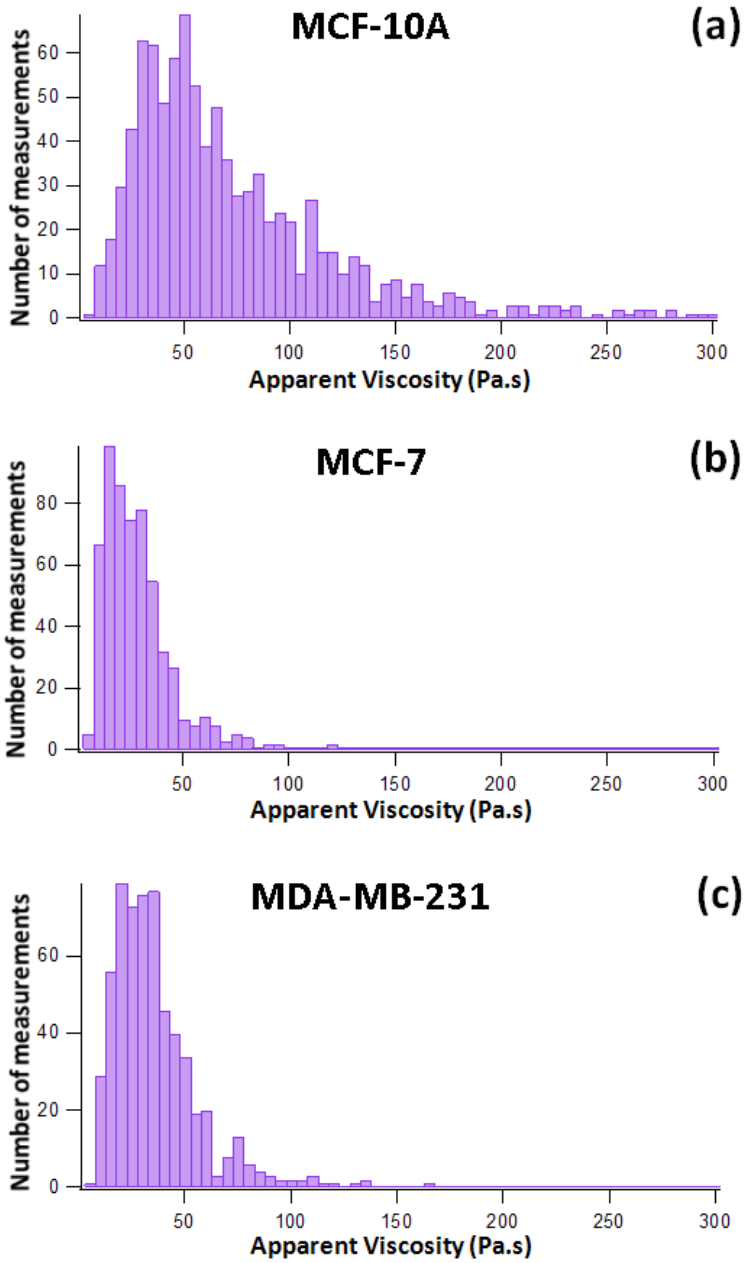

Figure 4.18: Histograms showing the distribution of apparent viscosities for MCF-10A cells (a), MCF-7 cells (b) and MDA-MB-231 cells (c).

test shows statistically significant differences between the apparent viscosities of all three cell lines measured ($p<0.001$). All parameter values extracted from the model fitting are displayed in table 4.2.

4.5.11 Discussion

The Wilcoxon Rank test shows significant differences between the hyperplastic MCF-10A breast cell line and the cancer MCF-7 ($p<0.001$) and MDA-MB-231 ($p<0.001$) cell lines, for both elastic models with the MCF-10A cells being significantly less deformable. There is some indication of a negative correlation between metastatic potential and mechanical deformability when comparing the elastic modulus values between the MCF-7 and MDA-MB-231 cell lines; with the Hertz results indicating significantly lower modulus values for the MCF-7s compared to the MDA-MB-231 cells ($p<0.001$) whereas the Oliver Pharr results show no significant difference ($p>0.05$) between the two cancerous cell lines. This may be down to the different cell morphologies. The MCF-7 cells are typically more 'rounded' when grown in petri dishes and so the underlying cytoskeleton may have less of an effect on the initial part of the indentation for the MCF-7 cell line compared with the more spread morphology of the MDA-MB-231 cells. At the greater indentations at which the Oliver Pharr measurements take place the intracellular structures may be contributing similarly to the response of the cells to an applied load, which could explain why there appears to be no significant difference in the Oliver Pharr moduli for the two cell lines.

The Wilcoxon Rank test shows statistically significant differences between the apparent viscosities of all three cell lines measured when comparing each cell line with the other two ($p<0.01$ for all comparisons).

To ensure any differences were not due to culture medium or cell confluency, studies were repeated and the same media was used for both MCF-7 cells and MDA-MB-231 cells; as it has been shown that differing compositions of cell media can affect the measured mechanical properties in this type of experiment [94]. Since the MCF-10As could not be grown in the same medium, the MDA-MB-231

cells were cultured in the MCF-10A media and characterised as a control experiment as shown in table 4.3. The MDA-MB-231 cells cultured in MCF-10A media showed significantly increased elastic modulus values for the Hertz results compared with MDA-MB-231 cells in their normal media ($p<0.01$), however there was a significantly reduced Oliver Pharr modulus ($p<0.01$) compared with MDA-MB-231 cells in their normal media. This is not unexpected as it has been previously shown that cellular mechanical properties can be affected by the growth medium. The intention of the control study characterising the MDA-MB-231 cells in MCF-10A media was to ensure that the media was not solely responsible for the MCF-10A cells having significantly higher modulus values than the cancerous cell lines. The Wilcoxon Rank test showed a significant difference between the MCF-10A cells and the MDA-MB-231 cells in MCF-10A media with the MDA-MB-231 cells having significantly lower values for both the Hertz ($p<0.01$) and Oliver Pharr ($p<0.01$) modulus respectively. It was concluded from this that the significantly higher stiffness of MCF-10A cells compared to the two cancerous cell lines was not due to the culture medium. Cell confluency has also been shown to affect measured cell stiffness [95, 96]. Consequently these characterisation experiments were performed on single cells wherever possible.

The MDA-MB-231 cells in MCF-10A media had significantly lower apparent viscosities than the MDA-MB-231 cells in their normal media ($p<0.01$). It is not unexpected that a different culture medium should have such an effect on the measured apparent viscosity. The fact that the MCF-10A media lowered the apparent viscosity rather than increasing the level of apparent viscosity measured from the MDA-MB-231 cells is another indication that the significantly increased values exhibited by the MCF-10A cell line are not due to the culture medium used.

It has been shown that for a number of different cancer types that cancerous

cells are significantly more deformable than their benign and normal counterparts [41, 37, 69, 72, 73, 74, 75]. The results of the experiments described in this chapter are in agreement with the existing literature, with the MCF-10A cell line significantly less deformable than the MCF-7 and MDA-MB-231 cell lines when comparing measured Hertz and Oliver Pharr moduli and apparent viscosity values. Previous studies have also shown a positive correlation between mechanical properties of individual cancer cell lines and their malignancy/metastatic potential [46]. This has not been seen in these data. The mechanical properties of the breast cancer cell lines investigated here do not exhibit a positive correlation with their metastatic potential. The MCF-7 cells are significantly more deformable than the MDA-MB-231 cells for the Hertz elastic modulus, but there is no statistically significant difference between the two cell types for the Oliver Pharr modulus, therefore the metastatic potential of these cells does not correlate with the mechanical properties measured here. An inverse correlation between mechanical properties and malignancy has been reported in prostate cancer cell lines [75].

Previous reports on the biomechanical properties of breast cancer cells show measured values of elastic modulus consistent with the results presented here [37, 50, 94]. The viscoelastic values presented here are also on the same order of magnitude as results published on ovarian cancer cells. Apparent viscosities of 144.7 $\pm$ 102.4 Pa.s for early stage ovarian cancer cells and 50.74 $\pm$ 29.72 Pa.s for late stage ovarian cancer cells were reported [46]. We observe similar trends here for breast cancer since the non-cancerous MCF-10A cells have significantly higher apparent viscosities than the cancerous MCF-7 ($p<0.001$) and MDA-MB-231 ($p<0.001$) cells.

Discrepancies between the different elastic models may be due to the methods of data analysis. To adhere to the general findings that the Hertz model is only

valid for indentations less than 10 percent of the cells height, the Hertz model was fit to the initial 50 percent of the approach curves in this analysis. The Oliver Pharr analysis was applied to the top 50 percent of the unloading curves. The hysteresis on unloading means that unloading is almost complete before the vertical height at which the Hertz fit finishes (i.e. 50 percent indentation) is reached. It is not surprising that there is such a large difference between modulus values obtained from approach and retract curves in such a hysteretic system.

4.5.12 Conclusion

It has been shown here that the mechanical properties of non-cancerous breast epithelial cells are significantly different from those of cancerous cells. The model dependent elastic moduli and apparent viscosities of the MCF-10A cells are significantly greater than those of the cancerous MCF-7 and MDA-MB-231 cells. This has been shown by many groups and consequently has recently led to the development of a device used for diagnostic purposes which uses an AFM to indent multiple points of a human breast biopsy to identify cancerous tissue from non-cancerous tissue [41]. To be able to identify the metastatic potential of this kind of sample from indentation type testing alone, however, is still debatable. In this study there appears to be no correlation between the mechanical properties of MCF-7 and MDA-MB-231 cells and the metastatic potential of the cells, since the MDA-MB-231 cells are known to have a much greater metastatic potential than the MCF-7 cells yet the mechanical properties show they appear to be significantly less deformable. The three different models used here to extract mechanical properties from the indentation data show strong correlation for each cell line being investigated, however the differences in values extracted for the two elastic models show the importance of understanding both what the model

is actually measuring and the limitations of these models. The Hertz and Oliver Pharr models yielded differing values of elastic modulus for different indentation depths which shows that the cells investigated here are not homogeneous elastic half spaces, as the models assume, therefore the elastic modulus values extracted from these models cannot be seen as intrinsic cell properties, but more appropriately as an approximation to the mechanical properties of the cell. The data suggest that investigation of the cells viscoelastic properties is more appropriate. I think if only one of the mechanical models described here was to be used to analyse the force-indentation data the viscoelastic model would have to be the one chosen. It gives a reasonable estimate of the elastic parameters of the cells but also gives information about the viscous properties of the cells in the form of an apparent viscosity. When relating these properties of living cells to the physiological conditions that these experiments are aiming to simulate in some way, the time-dependent elasticity of the cells is very important, for example the viscous properties of a cell undergoing intravasation or extravasation is crucial in understanding how metastatic cancer cells are able to invade secondary sites within the body.

4.6 Summary

The main aims of this chapter were to develop specific methods and protocols to investigate biomechanical properties of living cells using AFM. These methods have then been used to compare the mechanical properties of three breast cell lines of varying malignancies. Three different mechanical models were fitted to the experimental data acquired from indentation experiments showing that it is important to know specifically what you want to measure from these types of

experiments before choosing which mechanical model to apply to the dataset.

Force mapping in conjunction with fluorescence microscopy has also been used in this chapter to correlate force mapping data with fluorescence images of labelled mitochondria. This could be further investigated by labelling other intracellular organelles and also by developing the fluorescence microscope further to capture confocal images [97, 98] in conjunction with AFM to increase the resolution of the data being captured. This would allow visualisation of the cytoskeletal deformation during indentation as shown in the literature [98]. It should then be possible to build up a 3 dimensional fluorescence image of the location of specifically stained organelles during indentation, which when compared with force mapping data would be useful in measuring specific properties of intracellular components. The most suitable mechanical model could then be applied to the data depending on what cell component was being investigated.

Chapter 5

Mechanical Characterisation of Breast Cancer Stem Cells

5.1 Introduction

This chapter focuses on the identification of sub-populations of 'stem-like' breast cancer cells and assesses whether mechanical deformability can be used as a marker to detect these cells using AFM. The techniques to characterise the mechanical properties of these cell sub-populations have been developed in the previous chapter, see chapter 4. *In vitro* functionality experiments to assess the cell sub-populations proliferation and migratory behaviour were also performed by Kim Reeves to identify whether the 'stem-like' sub-populations possessed increased metastatic potential over the non 'stem-like' sub-populations.

The inefficiency of metastasis has led to the hypothesis that only a small subset of cells is capable of reinitiating tumour growth at a secondary site. These cells are increasingly believed to be a set of 'stem like' cells also known as cancer stem cells (CSCs), or as they are also referred to in the context of this chapter,

metastasis initiating cells (MICs). These MICs, like stem cells, have the capacity for unlimited self renewal and the requirement of a specific site for growth, as well as an increased resistance to apoptosis (programmed cell death) and an enhanced resistance to therapeutic drugs [99]. They are also thought to be vital in the metastatic process [99].

Stem cells in breast cancer were initially identified by the $CD44^+/CD24^-$ cell surface phenotype, due to their ability to form tumours in immunocompromised mice [30]. More recently an enzyme known to be involved in the self protection of stem cells, by the detoxification of many potentially cytotoxic molecules [100, 101], aldehyde dehydrogenase (ALDH), has been used as a prospective marker for CSCs. A study by Croker *et al* (2009) assessed four different human breast cancer cell lines (MDA-MB-435, MDA-MB-231, MDA-MB-468, MCF-7) for prospective CSC markers including the cell surface phenotype $CD44^+/CD24^-$ and high ALDH expression. Sub-populations of cells with high expression of CSC markers and/or high ALDH, were identified (in each cell line except MCF-7s). Experiments revealed that these sub-populations of cells showed increased growth, proliferation, adhesion, migration and invasion *in vitro* and enhanced tumorigenicity and metastasis *in vivo*, compared with the general population of cells for each cell line (i.e. the population with low expression of CSC markers and ALDH) [102]. The results of this study suggest that these $ALDH^{hi}CD44^+/CD24^-$ cells may be important in the metastatic process in breast cancer.

High ALDH expression has since been used in a number of instances as a marker for cancer stem cells, and in particular, to identify metastatic capacity in breast cancer cells [103, 104], in prostate cancer cells [105], gastric cancer [106] and cervical cancer [107]. A number of studies have recently shown that inhibition of ALDH activity reduces chemotherapy and radiation resistance of the stem like

$ALDH^{hi}CD44^{+}/CD24^{-}$ cells in a number of these different cancers [106, 104, 107]. High ALDH activity has also been shown to mediate metastasis and poor clinical outcome in inflammatory breast cancer (IBC) [103].

It is clear from these studies that ALDH is not only a possible prognostic marker to predict metastasis in a number of cancers, but also a key target in developing therapeutic regimes targeted at drug and radiation resistant cancer cells.

The main aim of the work in this chapter was to identify sub-populations of 'stem-like' cancer cells from the parental breast cancer cell lines and identify any difference in mechanical properties expressed by the different cell sub-populations using the methods developed in chapter 4. Identifying mechanical differences between these cells could prove to be a valuable method of identification of metastatic cells and offer further targets for therapy as well as improve current understanding of the metastatic process.

5.2 Identifying Metastasis Initiating Cells using Flow Cytometry

5.2.1 ALDH Experiments

To be able to characterise the mechanical properties of ALDH sub-populations of breast cancer cells using AFM, the sub-populations first needed to be indentified from the parental populations and sorted into $ALDH^{hi}CD44^{+}/CD24^{-}$ and $ALDH^{low}$ or 'normal' cells.

Initially, fluorescence activated cell sorting (FACS) was used in conjunction with the Aldefluor reagent (Stemcell Technologies) to identify and select possible

MICs in both the MCF-7 and MDA-MB-231 cell lines previously described. Both cell lines were sub-cultivated in their cell specific medium following the protocol in section 3.2 upto the point at which the cell pellet is re-suspended in fresh cell medium. For this method the cells were then re-suspended in 1 mL of Aldefluor Assay Buffer. At this point 500 μl of cell suspension was used to perform a cell count in the Vi-Cell counter to establish the number of viable cells per mL (Vi-Cell cell counter described in chapter 3). Viability of the cells was assessed by trypan blue exclusion. Trypan blue is a dye which is only absorbed by dead cells, so a count of viable and total cells per mL can be done. The sample was then adjusted to a concentration of 1 x 10^6 cells/mL. For each sample tested, one eppendorf was labelled 'test' and the other 'control'. 1 mL of the adjusted cell suspension was then added to each 'test' sample eppendorf. For each sample 5 μl of diethylaminobenzaldehyde (DEAB) solution, which is a specific inhibitor of ALDH activity, was added to the 'control' eppendorf and was recapped immediately to prevent evaporation of the DEAB. 5 μl of activated Aldefluor substrate per mL of sample was then added to the 'test' eppendorf. The sample was mixed and 0.5 mL was immediately added to the DEAB 'control' eppendorf. The 'test' and 'control' samples were then incubated for 45 min at 37°C and 5% CO_2. Following the incubation period, the samples were centrifuged, the supernatant pipetted off and the cell pellets re-suspended in 0.5 mL Aldefluor Assay Buffer. Flow cytometry was then used to determine the ALDH expression of the cells.

A flow cytometer passes thousands of cells per second through a laser beam by hydro-dynamically focusing the cells so that only one cell at a time passes through the laser beam. The laser light is scattered off the single cells passing through and forward and side scatter photo detectors are used to determine their size, granularity and fluorescence. In the case of the Aldefluor substrate, incident

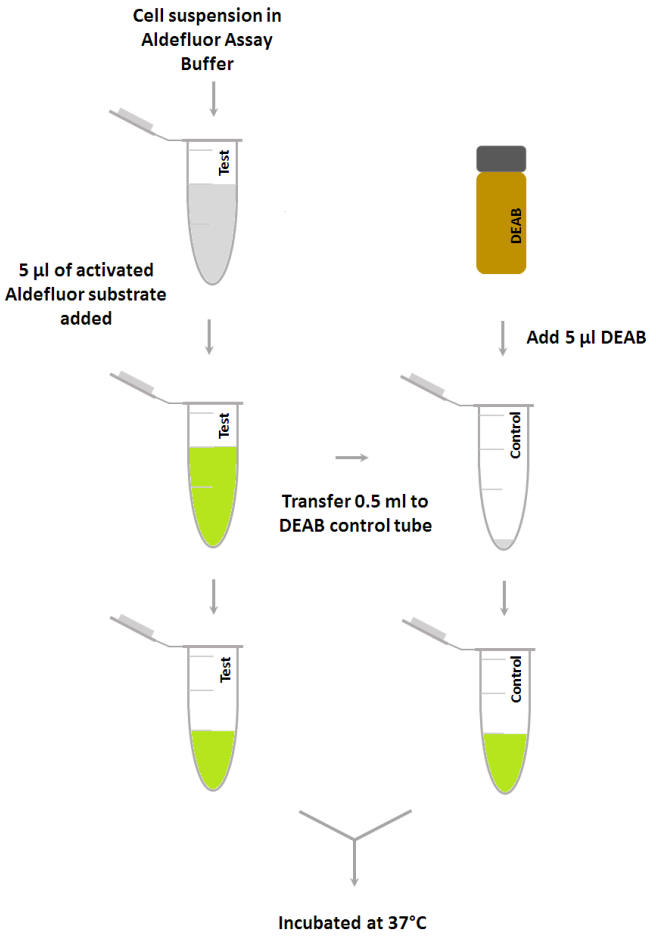

Figure 5.1: Schematic diagram showing the protocol for staining cells with Aldefluor stemcell staining kit from Stemcell Technologies.

laser light of 488 nm wavelength excites the substrate and light of wavelength 515-545 nm is emitted. This fluorescence is detected from the side scatter detectors. The forward scatter detector detects the size and granularity of the cells.

The 'control' sample was passed through the flow cytometer first and a 'gate' was set around the data as shown in figure 5.3. The 'test' sample was then passed through the flow cytometer and the the shift in fluorescence measured using the gating. By measuring the shift in fluorescence between the 'control' and 'test' samples for the MCF-7 and MDA-231 cell lines the size of the sub-population of prospective metastasis initiating cells can be measured. ALDH expression for

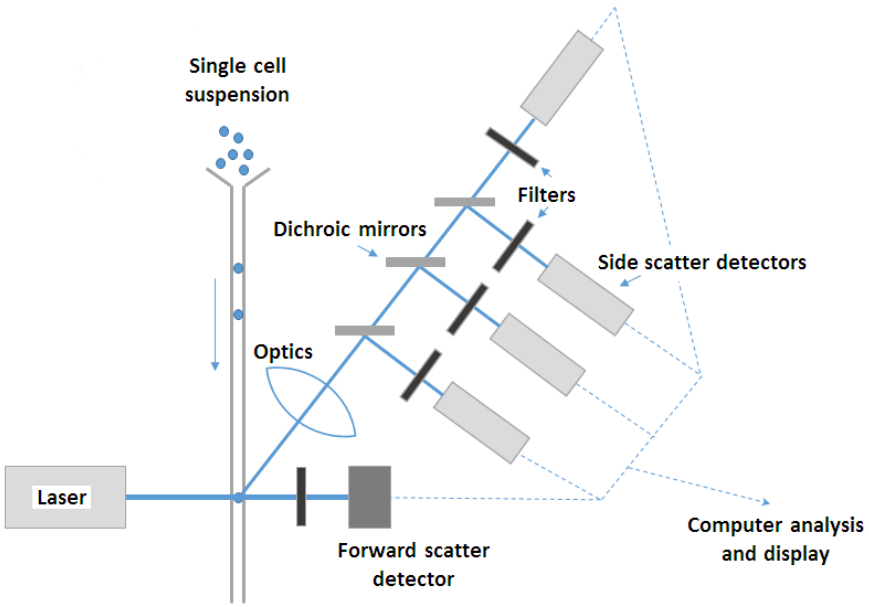

Figure 5.2: A schematic diagram of a flow cytometer.

both cell lines was determined using flow cytometry on 3 independent dates.

In the MCF-7 cell line 6.4 ± 1.3 % of cells express high levels of ALDH, whereas in the MDA-MB-231 cell line 11.3 ± 2.0 % of cells express high levels of ALDH (n=3), where the values are mean ± standard deviation. This is as expected since the MDA-MB-231 cell line is known to be more metastatic than the MCF-7 cell line, so it is expected to contain a larger percentage of possible metastasis initiating cells.

5.2.2 CD24/CD44 Flow Cytometry Experiments

Flow cytometry was also used to determine the expression of the CD24 and CD44 cell adhesion molecules on both the MCF-7 and MDA-MB-231 breast cancer cell lines. The cell adhesion molecules CD24 and CD44 and more specifically the $CD44^{+}/CD24^{-}$ phenotype are known to be an indicator of increased malignant and metastatic capacity in breast cancer cells as previously mentioned.

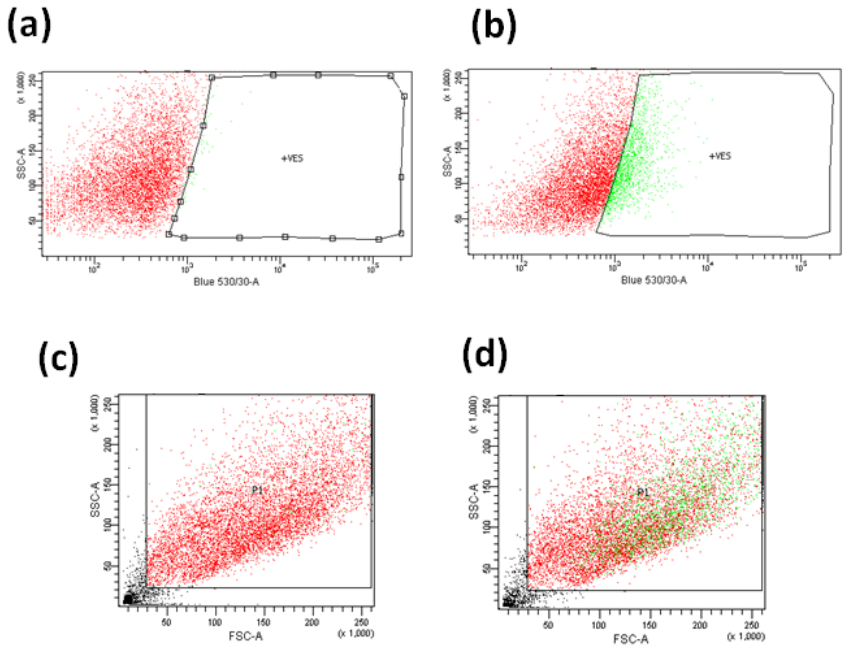

Figure 5.3: (a) An image showing the side scatter versus fluorescence for the 'control' sample of MDA-MB-231 cells using the sample preparation method described. An area is 'gated' to the right of the cells to identify a shift in the fluorescence in the 'test' sample. (b) Shows the shift in fluorescence in the 'test' sample (indicated by the green points). Increasing ALDH expression is shown from left to right.(c) shows the side scatter versus forward scatter for the light detected after being scattered around the cells in the control sample. (d) An image showing the cells with higher ALDH expression in the 'test' sample in green after gating. This shows that the ALDH expression is not dependent on cell size or granularity (Granularity is shown on the vertical axis).

Monoclonal antibodies (mAbs) were used to identify CD24 and CD44 expression on the cell surface of the MCF-7 and MDA-MB-231 cell lines. To identify CD24 adhesion molecule expression Anti-human CD24 APC was used along with mouse IgG1κ Isotype control APC to rule out any non-specific binding. Anti-human/mouse CD44 PE was used along with Mouse IgG2bκ Isotype control PE was used to identify CD44 expression.

The antibody staining protocol used was as follows. Cells were subcultivated following the method described in chapter 3 up until the point where they were

resuspended in PBS and counted using the ViCell cell counter as previously described. 1 x 10^5 of the cells were then transferred to each 1.5 mL micro-centrifuge tube (eppendorf tube) and 1 mL of cold (4°C) PBSF(90 % PBS plus 10 % FCS) was added to the cell suspension in each tube. One tube was used for each sample. For measuring CD24 and CD44 expression 5 sample tubes were needed for each cell line. These were for unstained cells, CD24 stained cells, CD44 stained cells, both CD24 and CD44 stained cells and finally a tube for cells stained with both isotype controls. The cells were then centrifuged for 5 min at 300g before aspirating off the supernatant and resuspending in 20 μl of PBSF. 1 μl of mouse serum was then added to the cell suspension and incubated at room temperature for 15 min. This inhibits non specific monoclonal antibody binding. The next step was to add appropriate combinations of mAbs or isotype controls to the cells. PBSF was added to the unstained sample to a final volume of 200 μl. For the CD24 sample 10 μl of Anti-human CD24 APC antibody was added to the cell suspension. For the CD44 sample 1.25 μl of Anti-human/mouse CD44 PE antibody was added to the cell suspension. For the CD24/CD44 sample both antibodies were added. For the Isotype control sample 5 μl of each of the mouse IgG1κ Isotype control APC and the Mouse IgG2bκ Isotype control PE were added to the cell suspension. PBSF was added to all cells to a final volume of 200 μl. Each sample was then passed through the flow cytometer one at a time with the results being recorded.

First the unstained sample was passed through the flow cytometer as a control. The Isotype controls were then passed through to identify any non-specific binding. Gating was performed on these isotype control samples to determine the baseline level for CD24 and CD44 expression. Any signal above these baseline values from the 'test' CD24/CD44 samples represents positive and specific expression of these

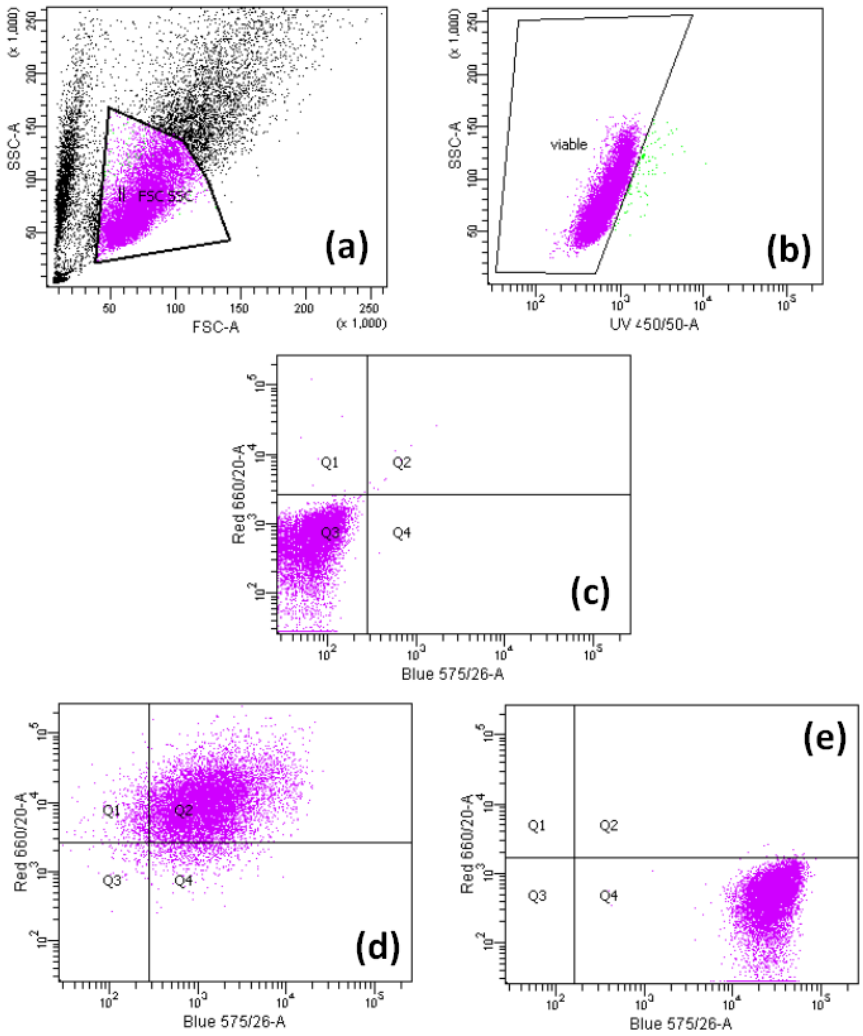

Figure 5.4: (a)shows the forward scatter versus side scatter data and the gating used to select the cells based on granularity and size. (b) shows side scatter versus UV detector data showing the viable cells selected in purple and the dead cells in green. (c) shows the isotype control data and how the gating was set. (d) is a typical graph showing data for MCF-7 cells stained for CD24/CD44 expression. (e) is a typical graph showing MDA-MB-231 cell staining for CD24/CD44 expression. In (c), (d) and (e) CD24 expression is shown on the vertical axis and CD44 expression is shown along the horizontal axis.

two cell surface markers. The individual and combined CD24 and CD44 labelled samples were then passed through the flow cytometer and the data recorded. All samples were stained with a UV live/dead viability stain prior to being analysed using the flow cytometer. The stain is only taken up by dead cells. Only single cells were used in the analysis by gating initially using forward and side scatter data which is used to ignore cell debris and grouped cells which pass through the laser. Viable cells were then selected by gating the side scatter and UV detector data. This experiment was performed on three different dates for both the MCF-7 and MDA-MB-231 cell lines.

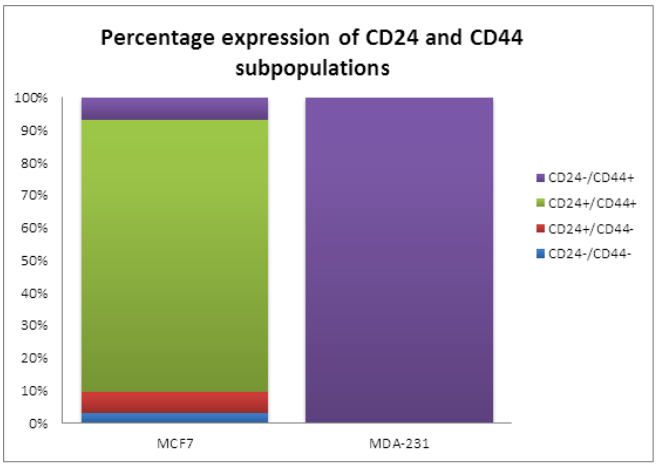

Figure 5.5: Bar charts showing the percentage expressions of CD24/CD44 phenotypes for the MCF-7 and MDA-MB-231 cell lines.

Expression of these markers for the MDA-231 and MCF-7 cell lines showed that the MDA-231 cells had a significantly higher metastatic marker expression compared with the MCF-7 cells ($p<0.01$). $99.8\pm0.1\%$ of MDA-MB-231 cells and $7.0\pm0.6\%$ of MCF-7 cells were of the $CD24^{-}/CD44^{+}$ cell phenotype. This was expected since the MDA-231s are known to be more metastatic than the MCF-7s.

Experiments were also performed to 'triple label' the cell lines with the intention of using flow cytometry to not only quantify the expression of CD24 and

CD44 adhesion molecules expressed by the cell lines but also to group the cells initially into ALDH sub-populations to see whether the percentage of cells expressing the $CD24^{-}/CD44^{+}$ cell phenotype correlated with the $ALDH^{high}$ sub-population within each cell line. These experiments were inconclusive since the fluorescent markers used for the CD44 labelling had an emission spectral overlap with that of the ALDH stain rendering it impossible to distinguish between the two signals.

5.2.3 Confocal Imaging of Actin in MDA-MB-231 Cells

After it was noticed that cell confluency affected the mechanical properties in chapter 4 confocal microscopy was used to compare the expression of actin in MDA-MB-231 cells for single cells and cells clustered together in the same sample. This was to visualise how cell confluency might influence the mechanical properties of confluent cells and affect the measured mechanical properties from AFM indentation experiments. For this experiment the MDA-MB-231 cells were cultivated following the usual method described in section 3.2 but seeded at 100,000 cells per well in a 4 well chamber slide. The wells were coated with 20 μg.mL^{-1} fibronectin in PBS an hour prior to the MDA-MB-231 cells being seeded. The cells were then placed in a humidified incubator at 37°C and 5% CO_2 for 24 h. After 24 h the media was removed and the cells fixed in 4 % formaldehyde for 20 min. The cells were then washed in PBS three times for a duration of two min per wash. The cells were then permeabilised with 0.1 % triton in PBS for five min, after which, the cells were washed a further three times in PBS for two min per wash. The cells were then stained with Texas-red phalloidin (Life Technologies) (1:83) in 10 mM Hepes buffer(pH 7.5, 0.15 M NaCl) for 1 h at room temperature. After the incubation the cells were washed four times for a duration of five min per wash. The bottom of the chamber slide was then marked with permanent marker

to show the location of the chambers before the plastic chambers and adhesive were removed from the upper side of the chamber slide. One drop of vectashield mounting medium containing DAPI (Vector Laboratories) was added on top of each well area before placing a glass coverslip on top of the slide. DAPI is used to stain the nuclues of a cell. Clear nail polish was then used to seal the glass slide to the coverslip. The sample was then kept at 4°C before observation on the confocal microscope. The phalloidin stained MDA-MB-231 sample was viewed using a

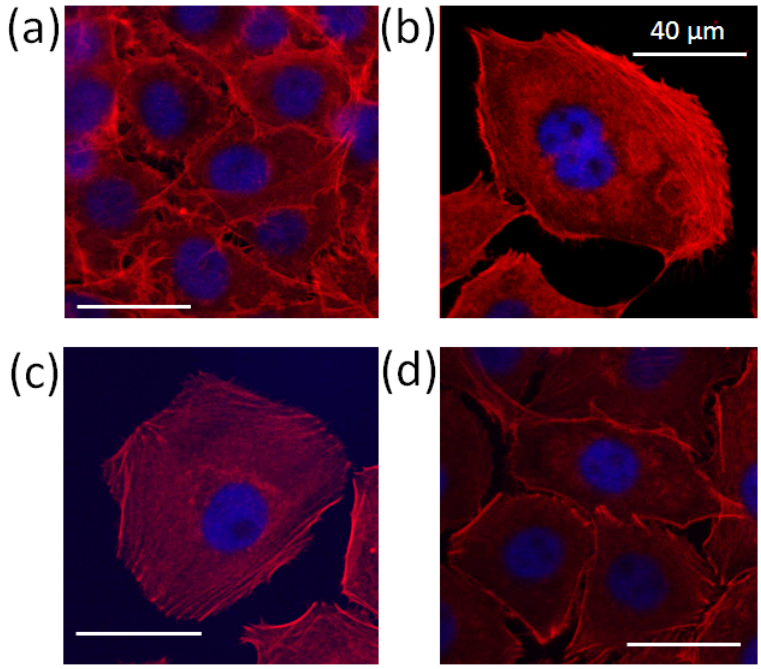

Figure 5.6: Confocal images of MDA-MB-231 cells stained for actin with phalloidin and DAPI. The actin is shown as red in these images and the nucleus is shown in blue. The scale bar in each image represents 40 μm.

confocal microscope with a 40 x liquid immersion lens. The images show that the concentration in these cells is typically higher at the edge of the cells. Specifically in the single cell images the actin concentration is noticeably higher around the edges. Actin is known to be involved in cell motility and cells have been shown experimentally to have increasing concentration of actin towards the leading edges

of their spreading membrane regions [108, 109]. For the case of the more confluent cells shown in images 5.6 (a) and (d) the actin concentration is highest at the adherens junctions between cells. This increased actin concentration at cell-cell junctions is known to be involved in epithelial cell binding [110].

5.3 *In vitro* Functionality Experiments

5.3.1 Cell Proliferation Assay

The cell proliferation/MTS assay is a colourimetric assay which measures the cellular metabolic activity. Cells are seeded in 96 well plates and proliferation is measured using MTS solution. At intervals of 24 h MTS solution is added to the wells and incubated at 37°C and 5% CO_2 for 3 h in darkness. Absorbance in each well is then measured using a spectrophotometer at 492nm. Relative absorbance is calculated by subtracting off absorbance from the control wells containing only media. The absorbance is representative of the cells proliferation.

5.3.2 Migration/Boyden Chamber Assay

The migration/invasion Boyden chamber assay is a chemotactic assay in which cells are plated into a well containing serum free media which is separated from a chamber (filled with serum media and positioned below it) by a porous membrane coated in fibronectin. After 24 h in physiological conditions the membrane is removed and the cells are fixed with Haematoxylin, washed and stained. The membrane is then dried and 5 random fields are counted for each well to give an average number of migrated/invasive cells per well.

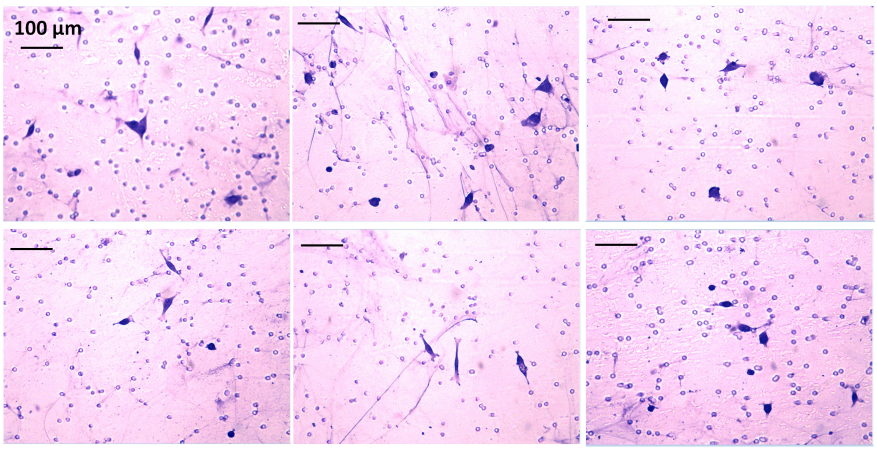

Figure 5.7: Images of a typical Boyden chamber assay membrane after 24 h with cells fixed and stained. Each image is a random field showing the purple stained cancer cells that have migrated through the membrane. The scale bar in each image represents 100 μm.

5.3.3 Methods

The functional assays described above were performed on MDA-MB-231 ALDH sub-populations by Dr Kim Reeves. For the proliferation experiments 6000 MDA-MB-231 cells were plated in 6 wells of a 96 well plate on 3 separate occasions for each ALDH sub-population and each time point (24, 48, 72, 96 and 120 h). The ALDH cells sub-populations were selected using FACS as previously described. The three ALDH sub-populations of MDA-MB-231 cells used for the proliferation studies were ALDH^{low}, ALDH^{high} and an unsorted/mixed population. The unsorted/mixed population were also passed through the flow cytometer for consistency.

For the migration assay the ALDH^{low} and ALDH^{high} sub-populations were compared. 10^4 cells were plated into 6 Boyden chamber wells and were allowed to migrate for 24 h before being fixed, washed and stained and then counted using an optical microscope.

These assays were attempted on ALDH sorted MCF-7 cells by myself also, but due to the length of time required to stain and sort the MCF-7 cells into

ALDH^{high} and ALDH^{low} sub-populations on the flow cytometer and the very low percentage of ALDH^{high} MCF-7 cells to begin with, the cells became apoptotic during sorting and the experiment was unsuccessful since there were not enough viable cells. This result itself showed the decreased survivability of the MCF-7 cells compared with the MDA-MB-231 which correlates with the respective cell lines potential malignancies.

5.3.4 *In vitro* Results and Discussion

Dr Reeves' proliferation results showed that ALDH^{high} MDA-MB-231 cells proliferate at significantly higher levels than the ALDH^{low} MDA-MB-231 cells for the 48, 72, 96 and 120 hour time points ($p<0.01$). The mixed population showed significantly higher proliferation levels than the ALDH sub-populations for these time points also ($p<0.01$) indicating that the heterogeneity of ALDH expression in the cell population may impact cell proliferation somehow.

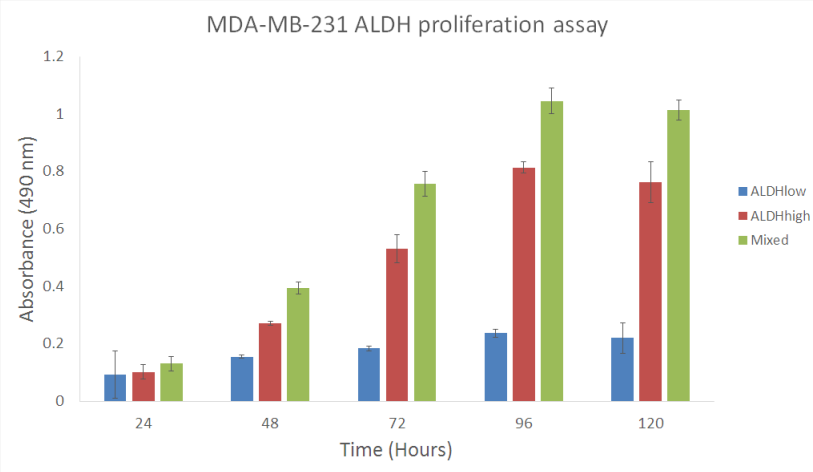

Figure 5.8: A graph showing the proliferation of three ALDH sub-populations of MDA-MB-231 cells over 120 h.

Dr Reeves' migration assay results show that the ALDH^{high} MDA-MB-231 cells migrate significantly more than ALDH^{low} cells over a 24 hour period ($p<0.01$).

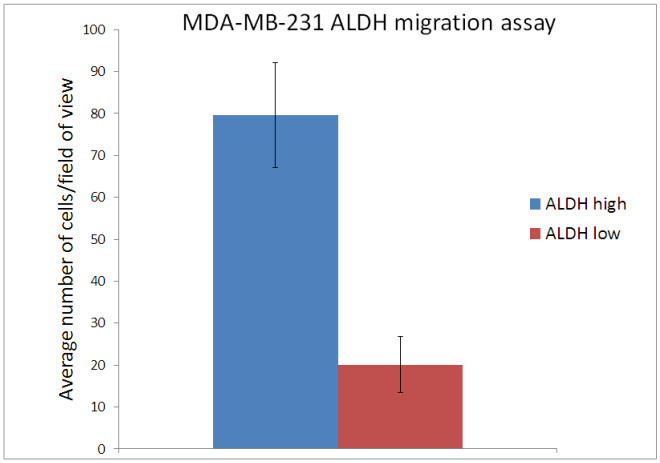

Figure 5.9: A graph showing the migration of the ALDH^{low} and ALDH^{high} sub-populations of MDA-MB-231 cells after being allowed to migrate for 24 h.

The results shown here from Dr Reeves' experiments show that the ALDH^{high} MDA-MB-231 cells display significantly increased migratory and proliferative behaviour compared with the ALDH^{low} MDA-MB-231 cells which is in agreement with previous ALDH studies [103, 99]. These results indicate that ALDH expression is indeed a good indicator of metastatic potential in the MDA-MB-231 breast cancer cell line. It could be the case that increased ALDH expression, which is known to be involved in the self protection of cells, may be linked with increased cell survival and therefore the ALDH cells survive being passed through the flow cytometer much better than cells with low ALDH expression.

5.4 Stem-like Breast Cancer Cell AFM Characterisation

5.4.1 Selecting 'Stem-like' Cells for AFM

Using FACS cells can be separated into sub-populations of ALDH^{high} and ALDH^{low} by gating around the top 10% of the fluorescence data and the bottom 10% respec-

tively. These cells can then be used in biological assays as previously described or be plated in petri dishes for AFM experiments. It was found that plating the cells in petri dishes after FACS for use with the AFM that the cells took much longer to adhere to the petri dish substrate than those cells which had not been passed through the flow cytometer. It may have been the case that the length of time in which it took to stain and sort the cells at 4 °C using this method affected the cells viability. This had a significant effect on the number of cells that could be used and so an alternate method of selecting the different sub-populations of cells was needed.

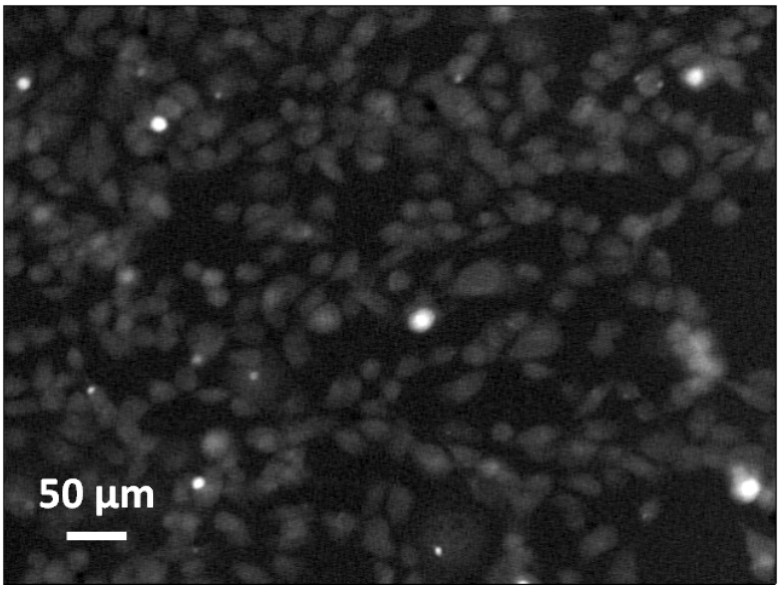

Figure 5.10: Fluorescent microscope image of MDA-MB-231 cells. The bright cells indicate the cells expressing high levels of ALDH. The ALDH^{high} cells were selected by thresholding these fluorescent images in ImageJ and using the particle analysis tool to extract area and grey value data for the cells. The cells were deemed ALDH^{high} if their maximum grey value was more than two standard deviations greater than the average grey value for all the cells analysed, effectively selecting the top 5 % brightest cells. The scale bar shown represents 50 μm.

To select ALDH^{high} cells for mechanical characterisation experiments using AFM, MDA-MB-231 cells were initially grown in 50 x 9 mm petri dishes for 24 h. The MDA-MB-231 cell line was chosen for this study since it possessed the highest

metastatic capacity of the three breast cell lines and *in vitro* studies showed that 99.8 ± 0.1 % of the cells were of the $CD24^-/CD44^+$ phenotype, which meant that it was more likely that the $ALDH^{high}$ cells selected via fluorescence microscopy were also more likely to be of the $CD24^-/CD44^+$ phenotype than the MCF-7 cell line. These markers could not be selected by using the fluorescence microscope in conjunction with the AFM since only the GFP filter cube was installed on the microscope setup. After 24 h incubation at 37°C and 5% CO_2 the cells were washed with PBS and 5 μl of activated Aldefluor substrate in 1 mL of PBS was added to the cells. They were then incubated at 37°C and 5% CO_2 for 45 min. After incubation the cells were then washed twice in PBS and fresh media was then added before imaging on the fluorescence microscope built onto the underside of the AFM stage. $ALDH^{high}$ cells were then selected as shown in figure 5.10. The fluorescence images were thresholded before using the particle analysis tool in ImageJ software to extract the pixel area and minimum, maximum and mean grey values for each cell. This data was then used to select the cells with mean grey values at least 2 standard deviations above the overall mean grey value of the cells, effectively selecting the brightest 5% of the cells.

5.4.2 AFM Methods

All AFM measurements were again obtained using an MFP 3D atomic force microscope (Asylum Research) integrated with an inverted optical microscope (Olympus microscope IX71, Tokyo, Japan). To ensure cell viability and stability, studies were performed with the MDA-MB-231 cells in their appropriate culture media, within 3 h of removal from the humidified incubator and performed at room temperature. The colloidal probe cantilever spring constant, k, was calibrated before each experiment using the thermal tune method [33] using the Asylum software as

described in chapter 2. The deflection sensitivity was, as in chapter 4, determined on the petri dish in the cell media. All measured cantilever spring constants were within the range specified by the manufacturer (0.005 $N.m^{-1}$ – 0.02 $N.m^{-1}$) and a new colloidal probe was used for each experiment.

For each experiment up to 8 cells were indented for both the $ALDH^{high}$ and $ALDH^{low}$/normal sub-populations and at least 4 experimental repeats were performed on each MDA-MB-231 sub-population. Each cell was first located using the inverted optical microscope after selecting the relevant cell using fluorescence microscopy, following which the colloid was positioned over the central region of that cell. Force maps were, as in chapter 4, taken over 4 x 4 point grids over the central region of the cell as depicted in figure 4.14 corresponding to an area of the cell between 5 μm^2 and 15 μm^2 dependent upon cell size and morphology.

The same indentation parameters as those described in chapter 4 were used for the work described in this chapter so that the measurements made could be compared with those taken on the parental cell lines. A constant indentation velocity of 3 $\mu m.s^{-1}$ was used throughout these characterisation experiments. A constant trigger force of 1 nN was used throughout the experiments corresponding to indentations between 250 nm and 1840 nm depending on both the heterogeneity of the cell sub-population and the variations in the mechanical properties within each cell. A constant indentation speed and trigger force was used throughout to ensure the loading rate was constant as possible so that any loading rate dependent changes in mechanical properties were kept to a minimum (see section 4.5.5). The parameters used in this study resulted in a loading rate of 5.2 ± 1.2 $nN.s^{-1}$ and 5.2 ± 1.2 $nN.s^{-1}$ (median ± median absolute deviation) used for the $ALDH^{high}$ and $ALDH^{low}$/normal sub-populations respectively. The same approach distance of 6 μm was used throughout with the fixed speed of 3 $\mu m.s^{-1}$, with a sampling

frequency of 0.25 Hz used for each set of approach/retract curves captured for this characterisation study.

5.4.3 Results

Table 5.1: The biomechanical properties for the ALDH^{high} subpopulations of semi-confluent MDA-MB-231 cells. Cells were imaged in PBS. Data is represented as median ± median absolute deviation.

	Property	ALDH^{high} MDA-MB-231
Hertz elasticity	E_{Hertz}(kPa)	0.18 ± 0.08
Oliver Pharr elasticity	E_{OP} (kPa)	0.39 ± 0.12
	Stiffness(mN.m^{-1})	3.2 ± 0.7

The ALDH sub-population characterisation studies were initially performed on single ALDH^{high} cells. The cells were semi-confluent, as they were in the parental cell line study in chapter 4 and they were also in PBS to increase the resolution of the fluorescence microscopy images for stem-like cell detection. It was noticed that during these initial studies the ALDH^{high} cells were often attached to other cells making it difficult to compare the different sub-populations. The significantly lower elastic moduli results from these ALDH^{high} cells could not be compared with the parental MDA-MB-231 cells as they were not in the same medium. Consequently all subsequent ALDH AFM studies were performed in their usual growth medium and not PBS as the initial experiments mechanical results may have been lower than the parental MDA-MB-231 cell line due to the medium in which they were in. To ensure any mechanical differences were not due to cell confluency the MDA-MB-231 cells were also grown in the petri dishes for 48 h after being plated at a higher cell density to ensure the cells were confluent during AFM studies. This allowed confluent ALDH^{high} cells to be compared with

confluent ALDH^{low}/normal cells.

Table 5.2: Comparison of the fitting of the mathematical models to the ALDH characterisation data. Data is represented as mean ± standard deviation.

	ALDH^{high} MDA-MB-231	ALDH^{low} MDA-MB-231
Hertz model R^2	0.976 ± 0.014	0.983 ±0.006
Oliver Pharr model R^2	0.997 ± 0.001	0.997 ± 0.001
Viscoelastic R^2	0.956 ± 0.041	0.951 ± 0.025

Table 5.3: Comparison of the biomechanical properties for the ALDH^{high} and ALDH^{low}/normal subpopulations of MDA-MB-231 cells. Data is represented as median ± median absolute deviation.

	Property	ALDH^{high} MDA-MB-231	ALDH^{low} MDA-MB-231
Hertz elasticity	E_{Hertz}(kPa)	0.33 ± 0.13	0.37 ± 0.16
Oliver Pharr elasticity	E_{OP} (kPa)	0.89 ± 0.28	0.92 ± 0.31
	Stiffness(mN.m^{-1})	4.8 ± 1.3	4.7 ± 1.1
Viscoelasticity	$E_{relaxed}$ (kPa)	0.24 ± 0.09	0.25 ± 0.09
	$E_{instantaneous}$ (kPa)	0.34 ± 0.12	0.34 ± 0.11
	E_{young} (kPa)	0.36 ± 0.14	0.37 ± 0.13
	μ (Pa.s)	45 ± 21	41 ± 17

5.4.4 Hertz Elasticity

To obtain an average value for the E_{Hertz} elastic modulus parameter, 16 measurements were recorded for each cell at different locations, and at least 28 cells were recorded for each cell sub-population. This allowed both cell surface heterogeneity due to internal cell structure and cell sample heterogeneity to be evaluated. This dataset is represented as a histogram which demonstrates the distribution of modulus values for each specific cell sub-population as shown in figure 5.11.

All Hertz elastic data distributions are positively skewed and can be described

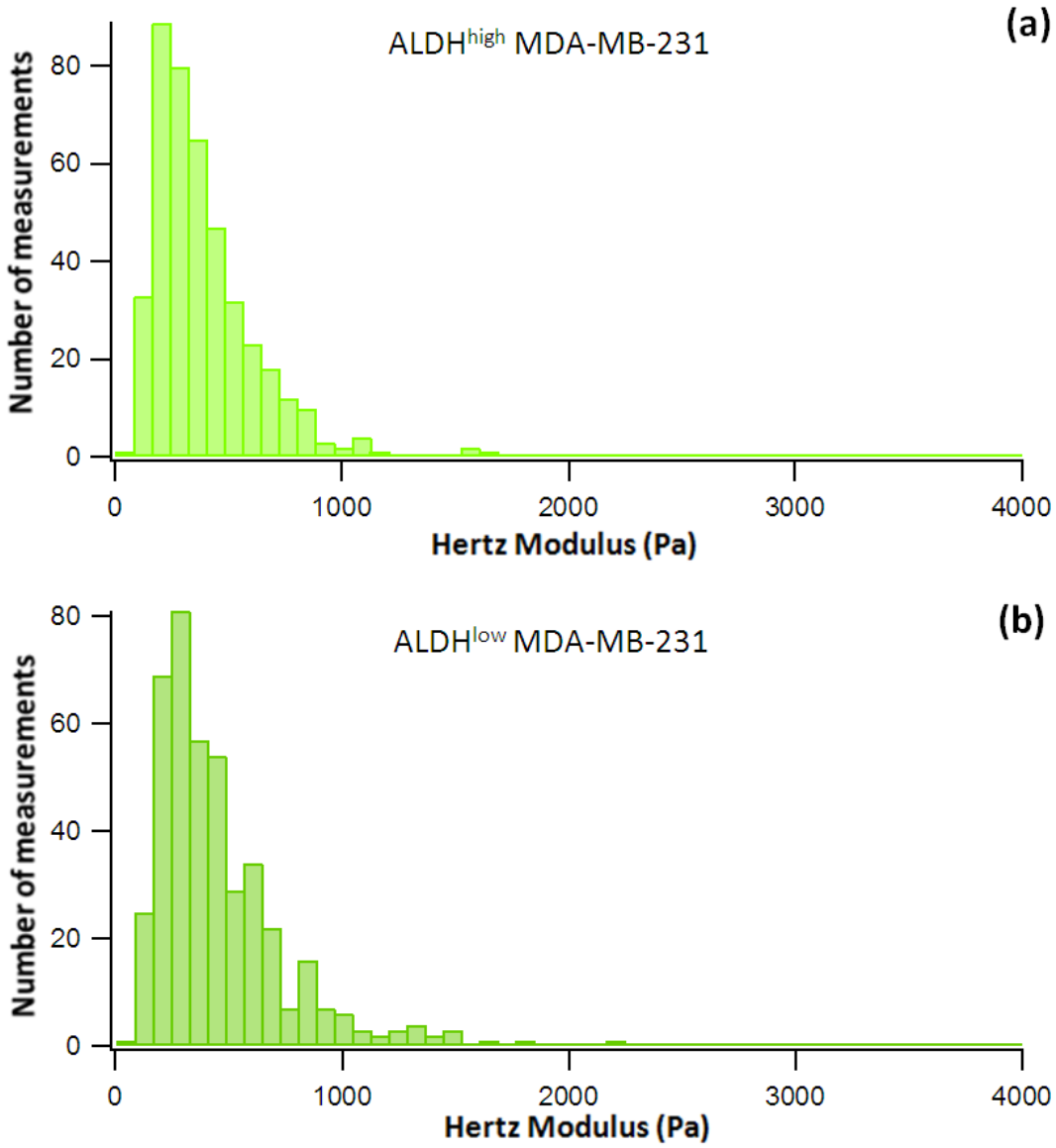

Figure 5.11: (a)-(b) Histograms showing the distribution of Hertz elastic moduli for ALDH^{high} MDA-MB-231 cells (a) and ALDH^{low}/normal cells (b).

as log normal distributions. Average E_{Hertz} values stated are median values plus or minus the median absolute deviation where the deviation represents the spread in the distribution of the data. For the cell lines investigated the average E_{Hertz} values obtained for the Hertz fitting are 0.33 ± 0.13 kPa and 0.37 ± 0.16 kPa (median ± median absolute deviation) for the $ALDH^{high}$ and $ALDH^{low}$/normal MDA-MB-231 cells respectively as shown in table 5.3.

5.4.5 Oliver Pharr Elasticity

A total of 16 measurements were recorded for each cell at different locations, and at least 28 cells were recorded for each cell line to obtain an average value for the E_{OP} elastic modulus parameter. This dataset is, as it was for the E_{Hertz} values, represented as a histogram as shown in figure 5.12.

All Oliver Pharr elastic data distributions are positively skewed and can be described as log normal distributions. Average E_{OP} values stated are median values plus or minus the median absolute deviation where the deviation represents the spread in the distribution of the data. For the cell sub-populations investigated the average E_{OP} values obtained for the Oliver Pharr fitting are 0.89 ± 0.28 kPa and 0.92 ± 0.31 kPa (median ± median absolute deviation) for the $ALDH^{high}$ and $ALDH^{low}$/normal MDA-MB-231 cells respectively as shown in table 5.3).

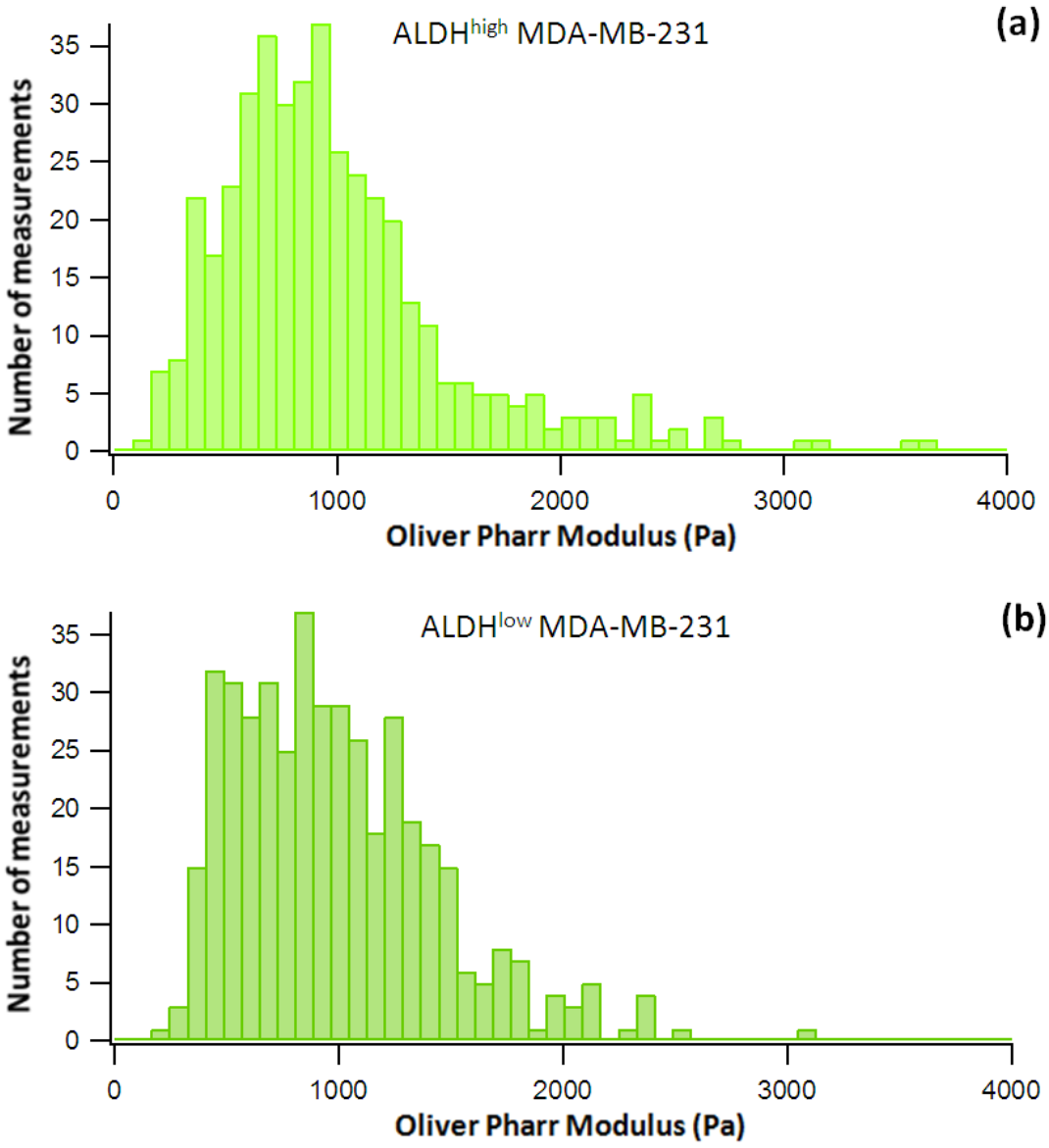

Figure 5.12: (a)-(b) Histograms showing the distribution of Oliver Pharr elastic moduli for ALDH^{high} MDA-MB-231 cells (a) and ALDH^{low}/normal cells (b).

5.4.6 Hertz Viscoelasticity

To obtain an average value for the apparent viscosity for each ALDH sub-population, μ, extracted from the viscoelastic model fitting of the stress relaxation data, the same number of measurements is taken for each cell as previously stated. The dataset is represented as a histogram showing the distribution of apparent viscosities for each cell line as shown in figure 5.13.

All apparent viscosity distributions are positively skewed and can be described as log normal distributions. Average viscosity values stated are median values plus or minus the median absolute deviation. Average apparent viscosity values, μ, for the cell lines were 45 $\pm$ 21 Pa.s and 41 $\pm$ 17 Pa.s for the ALDH^{high} and ALDH^{low}/normal MDA-MB-231 cells respectively. All parameter values extracted from the model fitting are displayed in table 5.3.

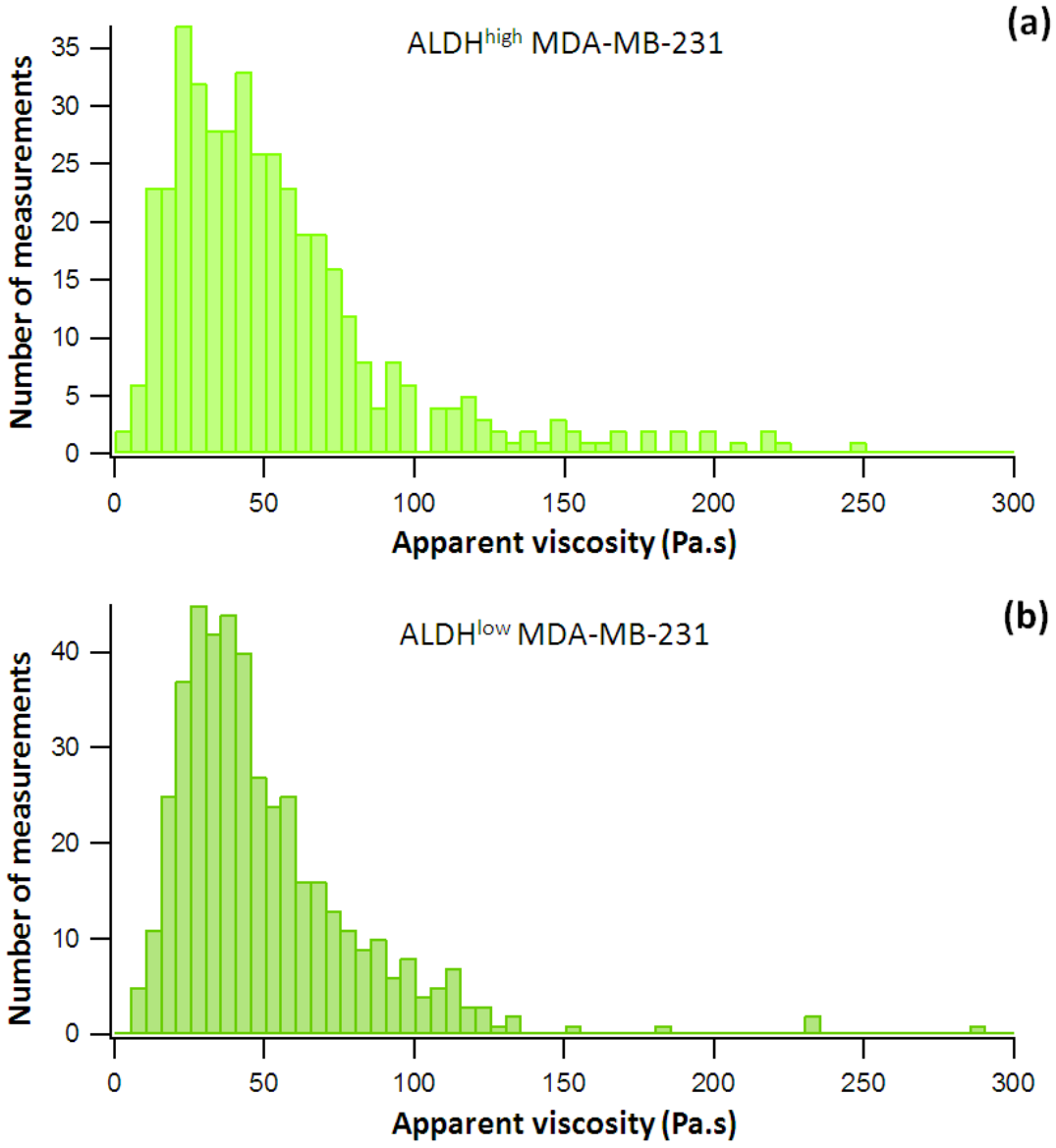

Figure 5.13: (a)-(b) Histograms showing the distribution of apparent viscosities for ALDH^{high} MDA-MB-231 cells (a) and ALDH^{low}/normal cells (b).

5.4.7 Discussion

The Wilcoxon Rank test shows there is a statistically significant difference between the Hertz elastic modulus results for the two sub-populations with the ALDH^{high} cells exhibiting a significantly lower hertz elastic modulus than the ALDH^{low}/normal cells ($p<0.01$). The Oliver Pharr modulus and apparent viscosity values however show no significant difference between the two cell sub-populations ($p>0.05$). Overall the results therefore appear to show no real significant difference between the two cell ALDH sub-populations for the MDA-MB-231 cell line. Again, as in chapter 4 the discrepancies between the three different mechanical models applied to the data are likely due to the methods of data analysis and the hysteresis on unloading which result in the unloading being almost complete before the vertical height at which the Hertz fit finishes (i.e. 50 percent indentation) is reached. It is not surprising that there is such a large difference between modulus values obtained from approach and retract curves in such a hysteretic system.

The Hertz modulus, Oliver Pharr modulus and apparent viscocity values for both ALDH sub-populations of the MDA-MB-231 cells are all significantly higher than the values measured on the parental MDA-MB-231 cell line shown in chapter 4 ($p<0.01$ for all comparisons). This is believed to be due to the higher confluency of the cells indented in the ALDH experiments.

Work conducted by Lee *et al.* on the migratory behaviour of MDA-MB-231 cells in a co-culture system with MCF-10A cells showed that due to the loss of E-cadherin expression by the MDA-MB-231 cells the 'stiffer' MCF-10A cells exerted a pressure on the MDA-MB-231 cells eventually causing them to spontaneously migrate between the MCF-10A cells to a region under less pressure [9]. It may be the case that in the work presented in this chapter, the fact that there appears to

be no mechanical difference between the ALDH sub-populations of MDA-MB-231 cells, may not be important in the migratory behaviour of these cells. It seems as long as they are more deformable than the surrounding environment, along with loss of adhesion molecules such as E-cadherin they may be able to migrate through the primary tumour environment and intravasate into the vasculature as long as they are relatively more deformable than their surrounding environment. The role of ALDH may then be more important in the survival of the circulating cells in the blood and lymphatic vessels, which is a specific trait of metastatic cells. Specific cell surface markers and their adaptability to survive in the vasculature may be more fundamental to the enhanced ability of metastatic cells to invade at a secondary site.

It has also been hypothesised by statistical methods that non 'stem-like' cancer cells or 'non-specialised' cancer cells may also have the ability to form secondary metastases by chance [111]. It would be less likely than the event of a more 'specialised' cancer cell but possible nonetheless. This idea could also support the results shown here that both ALDH cell sub-populations may possess the mechanical properties to be able to metastasise, but some may have other properties such as high ALDH expression also which may be more important in the survival of the cancer cells when in circulation and cell surface markers which may be present on these more 'specialised' cells may increase their chances of metastasising to specific sites. It has been shown that ALDH^{high} cells implanted into mice via intra-cardiac injection appear resistant to zoledronic acid treatment since their ability to form tumours is unaffected by the treatment compared with parental MDA-MB-231 cells ability to form tumours, which is significantly reduced by this bone anti-resorptive bisphosphonate [112]. This shows that ALDH expression could indeed play an important role in the survival of circulating tumour cells during metastasis.

5.4.8 Conclusion

Despite the MDA-MB-231 ALDH^{high} sub-population exhibiting an increased metas -tatic capacity in functional *in vitro* assays compared to the MDA-MB-231 ALDH^{low} /normal sub-population, there appears to be little difference between the two mechanically. It was hypothesised that the 'stem-like' ALDH^{high} cells would be more deformable than the ALDH^{low}/normal cells correlating with their enhanced invasive and proliferative properties compared with the ALDH^{low}/normal sub-population. The results don't appear to show this conclusively. The Hertz model results seem to be in agreement with this hypothesis, but the other mechanical property values are not. As mentioned in chapter 4 the mechanical models are fit to the indentation data at slightly different indentation depths due to the constraints of the models so it may be the case that the Hertz model results have less of a contribution from the underlying cytoskeleton of the cell and are more of a measure of the cells cytoplasmic region. It may be that the cytoplasmic region of the ALDH^{high} MDA-MB-231 cells is more deformable than that of the ALDH^{low} cells. Without being able to simultaneously capture the AFM indentation data with confocal microscopy though, it is not possible to know this. It may also be the case that a larger number of cells may need to be sampled to show if there is any significant difference between the sub-populations. This was not possible in this study due to the time and cost restrictions with such AFM experiments.

There are MDA-MB-231 cell lines that have been conditioned to preferentially migrate to the bone *in vivo* that could be used to compare with parental MDA-MB-231 cells. MDA-231 cells are administered to mice via intra-cardiac injection and subsequently form tumours. The tumours formed in the bone of these mice are then extracted and re-injected into other mice. This process continues for seven iterations resulting in an MDA-MB-231 cell line that specifically homes to bone. It

would be interesting to compare the mechanical properties of these cells with the parental MDA-MB-231 cell line to see if they correlate with metastatic potential. From the results presented in this chapter it appears that the 'stem-like' ALDH^{high} sub-population of cells has no mechanical advantage over the ALDH^{low}/normal cells in their ability to deform under an applied load. Maybe the specific mutations bone conditioned MDA-MB-231 cells undergo to be able to metastasise to bone so readily also have an important role in the mechanical deformability of the cells. It may be that the ALDH^{high} cells are the same cells that are able to form these bone tumours in which case it would be interesting to obtain such a bone specific cell line and compare it's ALDH expression with the parental MDA-MB-231 cells as well as characterise them mechanically using the methods described in this thesis.

5.5 Summary

A number of different techniques were used throughout this chapter to characterise ALDH sub-populations of breast cancer cell lines, particularly the MDA-MB-231 breast cancer cell line. The purpose of this chapter was to characterise these sub-populations using a number of techniques including the AFM protocol developed in chapter 4. The sub-populations of cells were successfully characterised however no overall significant difference between the mechanical properties of the ALDH^{high} and ALDH^{low} sub-populations was apparent. ALDH positive expression is still believed to be important in the self-protection of circulating tumour cells during metastasis however, even though it appears the ALDH^{high} cells have no clear advantage compared with the ALDH^{low}/normal cells in their ability to be deformed which was hypothesised to give them a particular advantage in intravasation/extravasation. It appears that there are other factors involved in the

homing of these metastatic cancer cells to the bone micro-environment.

Chapter 6

Single Cell Force Spectroscopy to Investigate the Mechanisms of Breast Cancer Metastasis

6.1 Introduction

The importance of cell adhesion in metastasis has already been highlighted in the introductory chapter of this thesis. During epithelial to mesenchymal transition (EMT) expression of E-cadherin is lost which has been shown to promote motility in breast cancer [9] and overexpression of N-cadherin has also been shown to be associated with EMT [11]. N-cadherin is a transmembrane protein which plays an important role in cell-cell adhesion. Cell adhesion molecules, such as integrins and cadherins, are linked to cytoskeletal components in the cell via intermediate proteins. External mechanical perturbations on a cell due to cell-ECM interactions are converted into chemical signals which induce adhesions between transmembrane integrin receptors and ECM contacts (ligands) [113]. These are

known as focal adhesions. The link between these external perturbations and the cells cytoskeleton couples the adhesive and mechanical properties of the cell, which means that the same signalling involved in cell adhesion may be involved in the mechanical rearrangement of a cells cytoskeleton during metastasis [114]. This makes cell adhesion an important topic in metastasis research as cell adhesion at a distant secondary site can possibly therefore induce mechanical alterations which allow the metastatic cells to extravasate through the endothelium and go on to form secondary tumours. Once invasion of the secondary site has occurred, further adhesive interactions with the tumour micro-environment can induce bone resorption, in breast cancer, which leads to the release of growth factors that can stimulate tumour growth which in turn stimulates further bone resorption as depicted in figure 6.1 [115, 116]. It has recently been shown by Coleman *et al* that current cancer treatment can promote bone resorption in breast cancer [116] and bisphosphonates such as zoledronic acid are used as an adjuvant therapy in patients with bone metastasis as an anti-resorptive agent [117]. Zoledronic acid is currently being used to prevent treatment induced bone loss in these patients [118] and could possibly be used in metastasis prevention in the future. It has been shown to reverse EMT in breast cancer by decreasing the expression of N-cadherin and upregulating E-cadherin expression [119]. A recent meta-analysis of over twenty two thousand women with early stage breast cancer showed that adjuvant zoledronic acid treatment lowered bone metastasis recurrence and breast cancer deaths in postmenopausal women. These findings showed a 17% reduction in breast cancer related mortality and are important in influencing current practices in the adjuvant treatment of early stage breast cancer in postmenopausal women [118].

The main aim of the work presented in this chapter was to investigate the inter-

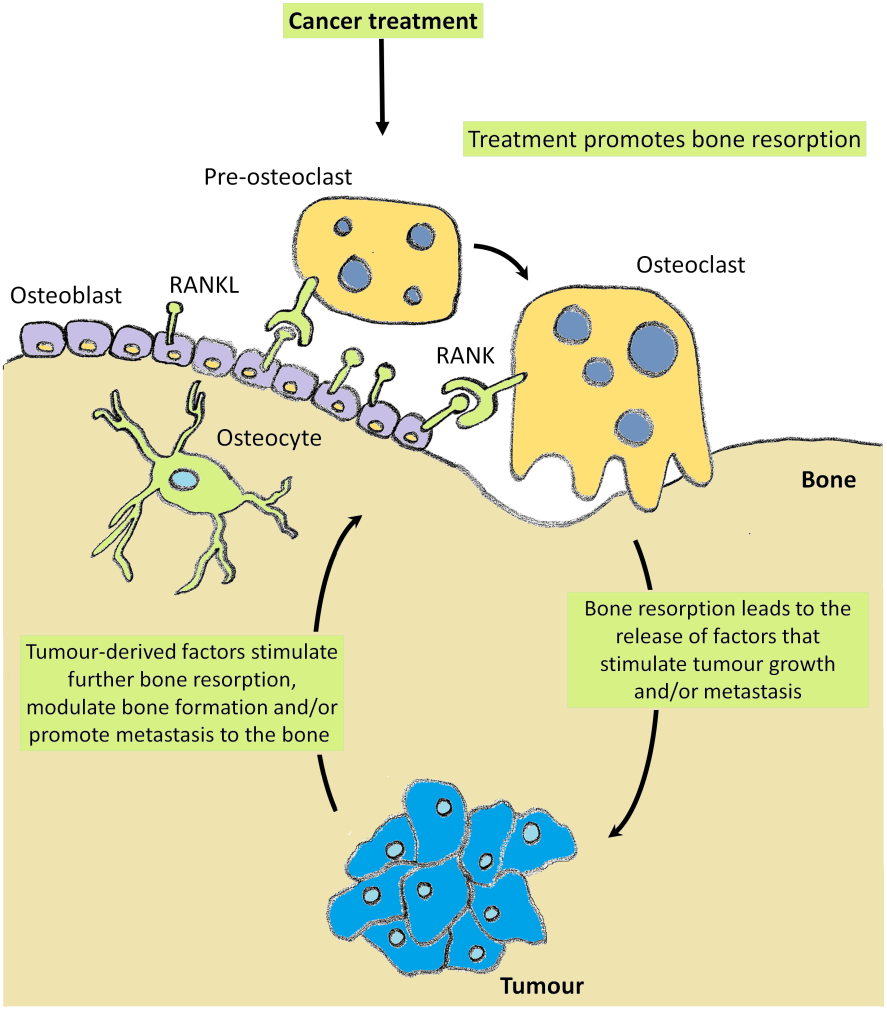

Figure 6.1: Cartoon showing the effect cancer treatment can have on the bone micro-environment during bone metastasis. The image shows how the secondary tumour can interact with cells such as osteoblasts and osteoclasts within this micro-environment to promote it's own growth. The cartoon is inspired by an image found in a review on the management of cancer treatment-induced bone loss by Coleman *et al* [116].

action between metastatic breast cancer cells and the tumour micro-environment at the secondary site. The bone tumour micro-environment is focused on in this research as breast cancer predominantly metastasises to bone and once it has there is currently no cure, only palliative treatment when the cancer reaches this stage. These interactions were to be investigated using single cell force spectroscopy (SCFS) with the AFM.

Not only can AFM be used to investigate the viscoelastic properties of individual cells, as shown in the previous experimental chapters, but it can also be used to investigate cell adhesion. AFM has often been used to measure the forces involved in protein-protein or protein-ligand interactions [120]. The ligand is attached to the AFM tip and the corresponding receptor is attached to the substrate. The tip is brought into contact with the surface forming an interaction bond between the ligand and receptor. The tip is then retracted from the surface and the force required for the ligand and receptor to fully dissociate, known as the unbinding force, is recorded [120]. As has been described in the introductory chapter of this thesis, as well as single proteins/ligands being attached to an AFM tip, it is also possible to attach living cells to the AFM cantilever to measure the adhesion forces between cells; a technique known as single-cell force spectroscopy [76]. The pulling range for such experiments is far greater than for single ligand/protein experiments due to the deformation of the cells as they are pulled apart and the resulting tethers/membrane nanotubes can be pulled tens of micrometres before dissociation occurs [121, 122]. Consequently the effective pulling range of the AFM being used must be sufficient to fully dissociate the two cells. It is also important that the contact conditions (duration and force) and the retraction parameters such as pull off rate can be controlled [59]. These limiting conditions of SCFS are the subject of the initial experimental development in this chapter.

A recent study investigated the adhesion between breast cancer cells of differing metastatic potential [123]. In this study the MCF-7, T47D and MDA-MB-231 cell lines were used. SCFS was used to to investigate each cell types cellular adhesion with itself. The adhesion force required to separate MCF-7 cells from MCF-7 cells, T47D cells from other T47D cells and MDA-MB-231 cells from other MDA-MB-231 cells was measured. The results showed an inverse relation between metastatic potential and adhesion force required to separate the cells. This inverse relation was attributed to the loss of E-cadherin expression and enhanced N-cadherin expression in these cell lines. Several SCFS studies have also recently investigated the cellular adhesion interaction between different cell types. The interaction between melanoma cells and cerebral endothelial cells has been investigated [124] as well as the adhesive interaction of T lymphocytes with endothelial cells [121] and prostate cancer cells with BME cells [125]. The latter was a study by Dr. Kim Reeves *et al* whose *in vitro* data has been referred to in chapter 5 of this thesis. In her findings she showed that the adhesive interaction between metastatic prostate cancer cells (PC3 cell line) and BME cells was significantly reduced when the cells were treated with zoledronic acid. It was therefore hypothesised that breast cancer cells would show similar behaviour when treated with zoledronic acid.

The work in this chapter focuses on the development of a SCFS setup to investigate the interaction between metastatic MDA-MB-231 breast cancer cells and both bone marrow endothelial (BME) cells and the 'osteoblast-like' Saos-2 cells. This was to model the site of extravasation to the bone with the BME cells and also to model the interaction between the metastatic cells with the bone microenvironment using the Saos-2 cells. The following sections describe the initial problems faced and the development of the experimental setup and methods to

be able to undertake these experiments.

6.2 Initial Experiments

Initial experiments used the Asylum MFP-3D setup without any development to ascertain whether it was possible to perform SCFS experiments to investigate the adhesive interaction between metastatic breast cancer cells (MDA-MB-231 cells) and confluent cells that represented the bone micro-environment at the site of bone metastasis in secondary breast cancer (such as the BME cells and Saos-2 ('osteoblast-like' cells). The MDA-MB-231 and BME cells were initially grown in separate 50 x 9 mm petri dishes. The MDA-MB-231 cells were plated in the dishes 24 h before AFM experiments and the BME cells were plated between two and five days prior to AFM experiments following the cells respective sub-cultivation protocols described in chapter 3. The AFM cantilevers used for these experiments were the 0.03 $N.m^{-1}$ MLCT levers. Before each experiment the cantilevers were washed in ethanol and dried in air before incubating in 5 $mg.mL^{-1}$ concanavalin-A (con-A, a carbohydrate binding protein) in PBS and incubated at RT for 10 min. The cantilever was then washed with PBS containing calcium and magnesium, to activate the con-A, and incubated at RT for a further 10 min. The cantilever was then attached to the cantilever holder and the AFM head was lowered until the cantilever was nearly in contact with the surface of the petri dish containing the MDA-MB-231 cells. An area of dish not containing cells was found to calculate the deflection sensitivity of the lever as described in previous sections of this thesis and the cantilever was then calibrated using the thermal tune method as also previously described (see chapter 2). After calibration a suitable single MDA-MB-231 cell was selected and the cantilever was lowered onto the cell so that the cell was positioned

directly behind the cantilever tip and held there with a force of approximately 1 nN for upto 30 seconds to allow the cell to bind to the functionalised cantilever as shown in figure 6.2(a). The AFM head was then retracted sharply to remove the cell from the petri dish surface. The cell was then allowed 10 min to fully bind to the cantilever surface. After attachment to the cantilever the AFM head was then retracted until the there was sufficient distance between the lever and dish to replace the petri dish containing MDA-MB-231 cells with the dish containing the BME cells. The breast cancer 'probe' was then lowered onto the confluent BME cells at a speed of 2 μm.s^{-1} over the full working distance of the z-piezo and retracted at the same speed to investigate the adhesion between the two cell types as shown in figure 6.2(b).

The initial findings from these preliminary experiments were that the z-piezo in the Asylum MFP-3D was not sufficient to fully separate the two cell types and so there was very little that could be extracted from the data. It was also found that during the changing of the petri dishes the capillary forces exerted on the cell attached to the cantilever when removing the lever from the media of one dish and submersing into the media of the second dish frequently damaged or removed the probe MDA-MB-231 cell from the cantilever which meant the experiment had to be restarted frequently. Considering this type of experiment is already labour intensive, as to generate sufficient data to form any statistically relevant conclusions a number of 'probe cells' have to be used to investigate the adhesion at a large number of sites, this problem was one which required a solution. The attachment of the MDA-MB-231 cell itself was also difficult. After being in the dishes for 24 h the cells were very adhered to the dishes which made it difficult to detach them. One solution to this would be to incubate the cells in these dishes for a shorter period of time before attachment to the cantilever. Another problem

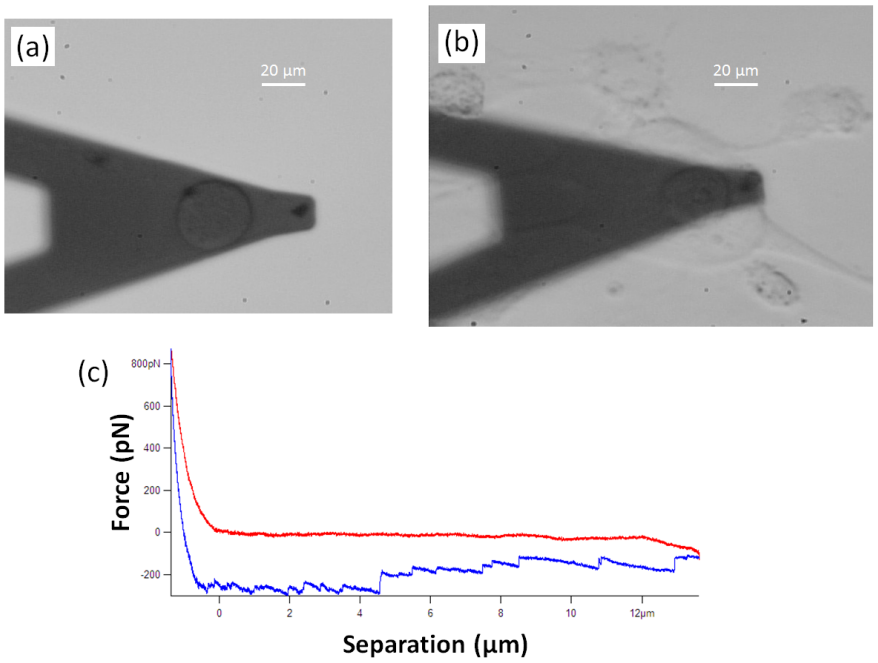

Figure 6.2: Bright field images of (a) an MDA-MB-231 cell attached to a 0.03 $N.m^{-1}$ cantilever, (b) is the MDA-MB-231 cell being used to 'probe' a confluent layer of BME cells. The BME cells are 'unhealthy' as they have began to 'round up' as can be seen in this image. (c) is a force-separation graph showing the adhesion between the two cell types. The blue curve is the retract data and the 'jumps' in the data represent individual unbinding events between the two cell types. It can be seen that the z stage limit is not great enough to fully dissociate these two cells even with the BME cells being relatively unhealthy.

faced from these initial experiments was the viability of the BME cells at room temperature. It was decided that the Saos-2 cells would be used initially instead since they were more adherent and therefore easier to grow onto the petri dishes.

Overall there was much to conclude from the initial experiments. The main finding was that the z-piezo did not have enough travel to fully dissociate the cells which were to be investigated. To overcome this a separate z-piezo (P-621.ZCL PIHera precision Z stage, Physik Instrumente) with travel of upto 100 μm was used in conjunction with the MFP-3D to perform these experiments. There were a number of issues with this setup that were first to be addressed before it could

be used to measure the adhesion forces between the different cell types.

6.3 Development of Instrumentation to Perform SCFS

6.3.1 Development of Extended Z-stage

The initial 'extended z-stage' setup is shown in figure 6.3. The z-piezo was powered

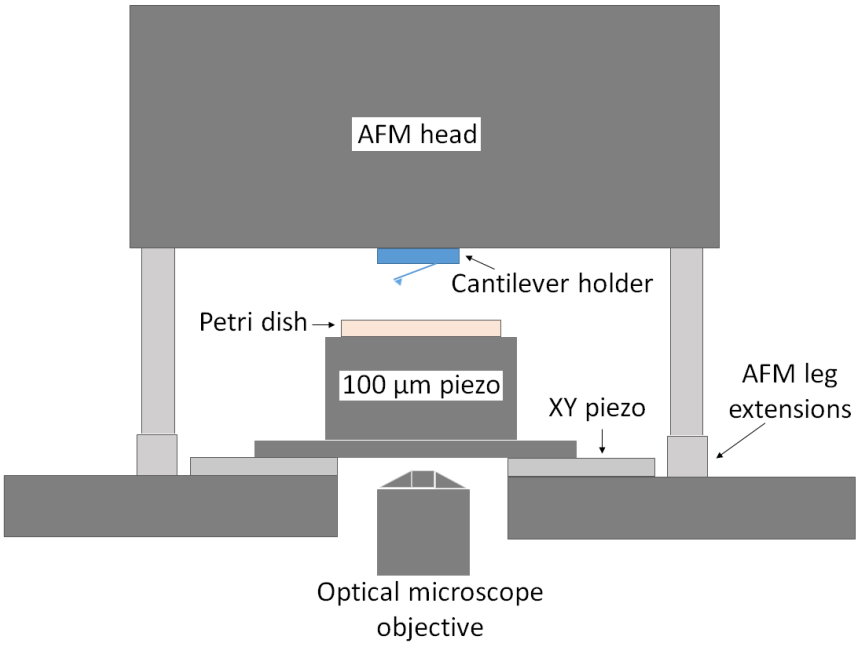

Figure 6.3: Schematic diagram showing the initial SCFS setup using the 100 μm z piezo in conjunction with the MFP-3D.

by a separate high voltage amplifier. The low voltage drive signal from the MFP-3D controller was input into a unity gain inverter based on an AD843 operational amplifier which inverted the drive signal. This was required because Asylum Research use a negative gain in their high voltage amplifier. The signal was then passed through a high voltage amplifier so that the signal which translated the

'normal' z-piezo 12 μm now had to move the extended z-piezo upto 100 μm. The inverter and original setup were originally put together by Dr. Nic Mullin. The main problem with this setup was that the extended z-piezo had no aperture which meant that the inverted optical microscope could not be used to select the cells and the resolution of the top optics of the AFM was not sufficient to perform the adhesion experiments. It would not have been possible to ensure the 'probe' cell was attached to the lever with these optics either. A second problem was that the stage was very susceptible to external mechanical noise which would significantly affect the accuracy of the data. A solution to the aperture problem would have been to purchase another 100 μm z-piezo and drive the two simultaneously with a glass platform joining them, on which the petri dishes could be attached. This would have allowed the inverted microscope to be used in conjunction with the AFM and allowed 100 μm of travel to fully dissociate the cells being investigated. Due to financial restrictions this option was not available to me and so the stage had to be adapted. A base plate was designed by myself and manufactured by the physics department workshop which was made to the same shape as the x-y-piezo stage so that there was an aperture in the centre through which the inverted microscope objective could be positioned and the whole extended stage could be moved using the x-y-stage. The extended z-piezo was attached to the left hand side of this base plate. A glass slide was then attached to the top of the z-piezo and overhung so that the far end of the glass slide could be fixed to the base plate with a vertical support as shown in figure 6.4. A lens extender was used to extend the height of the inverted microscope objective lens so that the cells in the petri dishes attached to the glass slide could be viewed in focus.

Since this setup was fixed at one end it had to be fully calibrated to ensure that any measurements made were accurate.

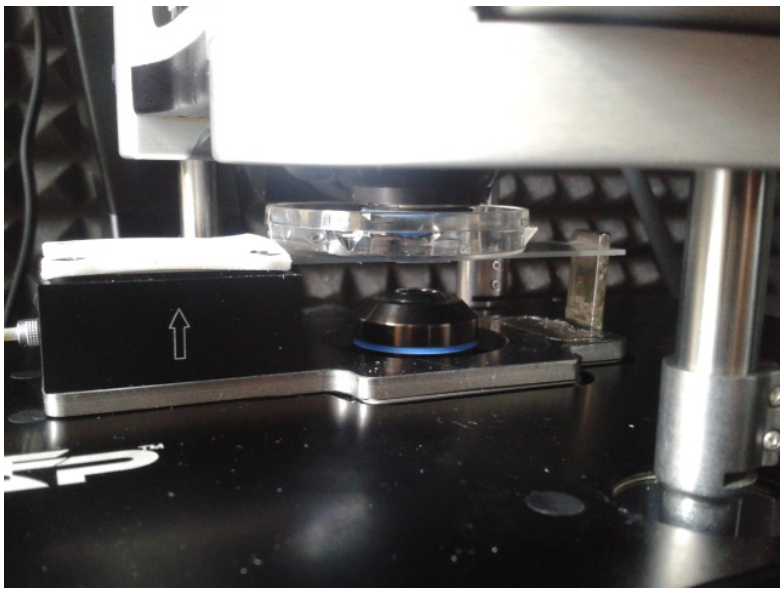

Figure 6.4: Image showing the extended z-piezo setup used in conjunction with the Asylum MFP-3D.

6.3.2 Calibration of Z-stage

The adapted z-stage setup first had to be calibrated before any adhesion measurements could be acquired from the live cell experiments. Before calibration of the setup I had an acoustic isolation chamber manufactured by the physics department workshop to reduce the mechanical noise in the experimental data (see figure 6.5). The stage first had to be calibrated to ensure that the distance travelled at the point the adhesion measurements were to be measured was accurately recorded. Without calibration the deflection sensitivity would be inaccurate and since the spring constant k depends on $\frac{1}{InvOLS^2}$, where InvOLS is the inverse of the optical lever sensitivity, it is really important for the z calibration to be accurate. Due to the adapted extended z-stage setup being fixed at one end the distance traversed at a particular point on the glass slide per volt applied to the stage varied according to that particular point's distance from the fixed end as shown in figure 6.6

Figure 6.5: Images showing the acoustic isolation chamber designed and constructed by the workshop to acoustically isolate the AFM to reduce mechanical noise in the experiments. The extended z-piezo setup was susceptible to mechanical noise and so this had to be reduced to improve the accuracy of the measurements.

To calibrate this extended z-stage setup a calibration grid with 200 nm deep wells was imaged across various points on the glass slide part of the stage where the petri dish would be attached. The z-piezo sensitivity setting in the software which controls the amount of z-piezo travel per volt applied was altered so that the calibration grid wells were accurately measured to be 200 nm. A typical calibration grid height image and cross section are shown in figure 6.7. Over the full area of glass slide that could be investigated by the AFM probe there was a 15% variation in the measured calibration grid well depth. The system was calibrated so that the wells were accurately measured at 200 nm as close to the z-piezo stack as possible to allow the maximum z-range possible from the setup. With the z-piezo sensitivity set at 230 nm.V^{-1} the maximum z-range of the system was approximately 37 μm and the wells were measured at 200 nm $\pm$ 4 nm. The tolerance on the calibration grid itself is $\pm$ 3%. By calibrating the system at this position it was important that all adhesion measurements were taken as close to this distance from the fixed and of the stage as possible, therefore the dishes were attached to the glass slide so that this position could be accessed by the probe.

As a check that the extended z-stage setup was accurately calibrated force

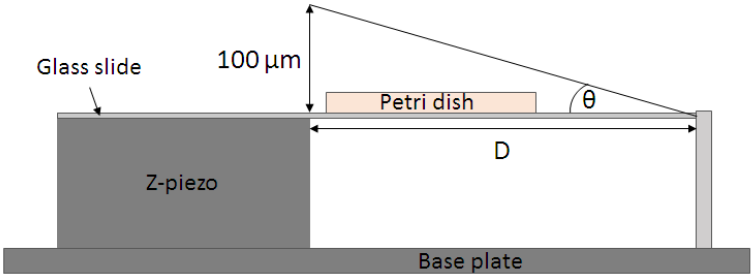

Figure 6.6: Schematic diagram showing that because of the fixed end of the glass slide the actual z displacement of the sample will be related to its distance from the fixed end. This meant that when calibrating the deflection sensitivity prior to each experiment the adhesion measurements were to be performed the same distance from the fixed end as the calibration was performed at to reduce any error in the measured separation. D in this diagram is the distance from the fixed end to the z-piezo. Since D >> 100 μm, this means that θ is very small and so the force measured does not need to be corrected.

indentation curves were acquired on the glass slide stage setup with the 'normal' AFM head setup and again with the extended z-piezo at the same voltage and using the same parameters. The deflection sensitivity of the 'normal' setup was then measured and compared with the extended z-stage setup. When taking force curves on the glass I noticed that there was a difference in slope between the approach and retract curves as shown in figure 6.8(a). After taking more

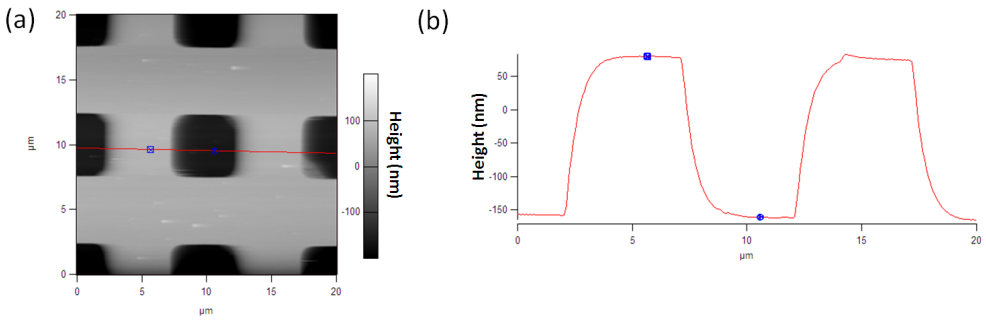

Figure 6.7: (a) is a contact mode height image of the calibration grid with 200 nm deep wells. The red line in the image shows the cross section which is graphed in (b). The two blue markers in (b) are then used to calculate the change in height.

force curves with a four second dwell of the cantilever deflection the retract curve then had the same gradient as the approach curve as shown in figure 6.8(b). This discrepancy was put down to a combination of creep and hysteresis in the extended z-piezo and from this observation it was decided when calibrating the deflection sensitivity of the cantilever to take measurements on the retract data after a dwell of the deflection to get an accurate value for the deflection sensitivity and correspondingly the spring constant value of the cantilever. The deflection sensitivity values measured from the 'normal' and 'adapted' stage setups were within 2% of each other with the z-piezo sensitivity of the extended z-stage set at 230 nm.V^{-1}.

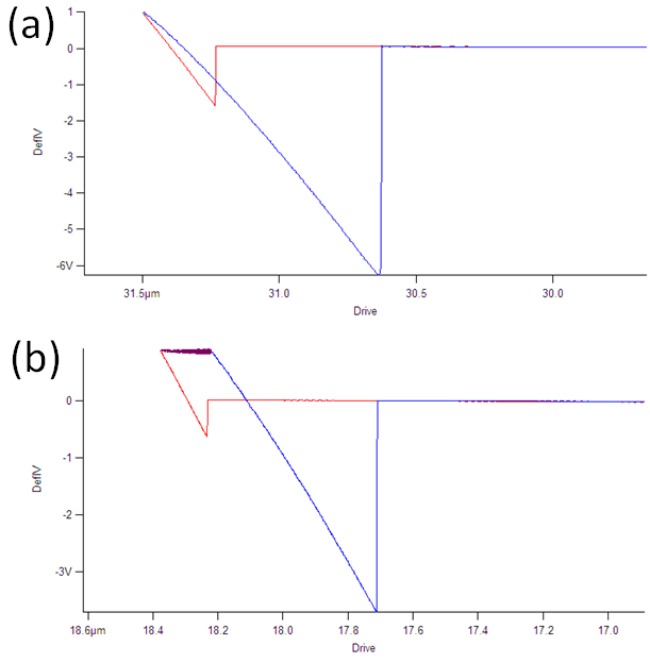

Figure 6.8: (a) A deflection versus z-piezo movement graph showing a force curve taken on the glass slide stage of the extended z-stage setup taken by moving the extended z-piezo as opposed to the 'normal' setup. (b) is a force curve taken the same way over the same point of the stage but with a two second dwell of the cantilever at the trigger point.

Now that the extended z-piezo stage had been calibrated the setup was used

to investigate the adhesion between the MDA-MB-231 cells and the Saos-2 cells.

6.4 MDA-MB-231 to Saos-2 Adhesion Experiments

6.4.1 Experimental Methods

For the AFM SCFS experiments to measure the adhesive interaction between MDA-MB-231 metastatic breast cancer cells and the 'osteoblast-like' Saos-2 cells the adapted extended z-stage setup described in the previous section was used throughout. The z-piezo sensitivity was set to 230 nm.V^{-1} for the duration of these experiments. The Saos-2 cells were grown in 50 x 9 mm petri dishes and sub-cultivated every 7 days at a ratio of 1:3 following the protocol in chapter 3. Cells used for adhesion experiments were grown for 7 days prior to adhesion experiments so that they had reached more than 80% confluency. The MDA-MB-231 cells were sub-cultivated following the protocol in chapter 3 and plated in 50 x 9 mm polystyrene dishes with a single 12 mm circular glass cover slip placed in the bottom of each dish before 2 mL of media and the cell suspension was added. This was to ensure the glass cover slip did not drift around the bottom of the dish. The MDA-MB-231 cells were plated up 20 h before the SCFS experiments were to take place. Prior to AFM experiments the 0.03 N.m^{-1} MLCT AFM cantilever was functionalised by washing in ethanol and drying in air as before and incubating in 5 mg.mL^{-1} con-A at RT, this time for 15 min. The cantilever was then washed and incubated in PBS containing calcium and magnesium for 15 min at RT. Whilst the cantilever was being functionalised the cells were simultaneously being prepared for SCFS experiments. The Saos-2 media was aspirated from the dish and the

cells washed once with 2 mL PBS before carefully removing the glass cover slip containing MDA-MB-231 cells from the MDA-MB-231 dish and placing it in the Saos-2 dish carefully so that it didn't slide around and detach the Saos-2 cells as shown in figure 6.9. The slide was then pressed down lightly with tweezers to 'fix' it in position on top of the Saos-2 cells before adding 3 mL of either fresh Saos-2 media, 3 mL of Saos-2 media containing 100 μg.mL^{-1} zoledronic acid, or 3 mL of Saos-2 media containing 20 μg.mL^{-1} of monoclonal anti-N-cadherin blocking antibody (Sigma-Aldrich) depending on the experiment being undertaken. Three experiments were performed at RT for each of the three treatments specified here to investigate the adhesion between the MDA-MB-231 and Saos-2 cells for untreated, zoledronic acid treated and anti-N-cadherin treated cells. The cells were incubated at RT for 30 min after the treatment was added prior to the dish being attached to the extended z-stage glass slide and the SCFS experiments performed.

Once the cantilever was functionalised, the cells had been incubated with their respective treatment and the dish was attached to the glass slide, the cantilever was lowered into the dish above the glass slide and a force curve with a 4 second dwell of the cantilever deflection was acquired on the glass slide to calculate the deflection sensitivity of the lever. The cantilever was then calibrated in the media using the thermal tune method described in chapter 2. After calibration a single MDA-MB-231 cell was then located and the lever lowered onto the cell so that the cell was positioned directly behind the tip of the cantilever until a small deflection was observed on the sum and deflection meter in the AFM software. The cantilever was then retracted swiftly and smoothly detaching the cell from the glass slide. The breast cancer cell was then allowed 10 min to adhere to the functionalised cantilever and equilibrate before the cantilever was then moved along the y-axis to a region of confluent Saos-2 cells in the dish as depicted in figure 6.9. Figure

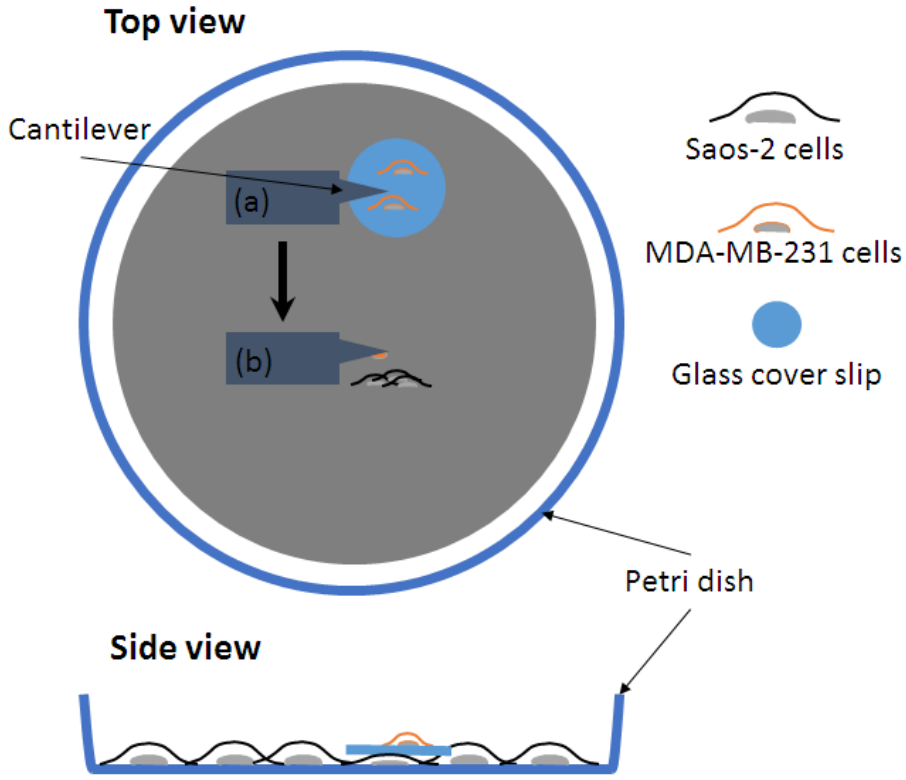

Figure 6.9: Schematic diagram showing the side and top view of the petri dish containing the MDA-MB-231 and Saos-2 cells. The MDA-MB-231 cells were grown on 12 mm glass cover slips for 20 h in 50 x 9 mm petri dishes and the Saos-2 cells were grown to a confluent monolayer in 50 x 9 mm petri dishes for 7 days. The top view schematic shows the position of the cantilever during deflection sensitivity force curve acquisition and cancer cell attachment at (a) and the position of the cantilever being somewhere below the glass cover slip where the adhesion measurements took place at (b).

6.10 shows brightfield images of the MDA-MB-231 cell attached to the lever and a cluster of Saos-2 cells to be probed. For each adhesion experiment performed a single MDA-MB-231 cell was used to probe 10 random locations of confluent Saos-2 cells in each dish. At each location a 4 x 4 point force map over a 10 μm^2 area was collected with a 5 $\mu m.s^{-1}$ approach and retract speed, 1 nN trigger point and an approach distance of 37 μm. These parameters were kept consistent throughout the experiments. In addition to these force maps, at the end of each

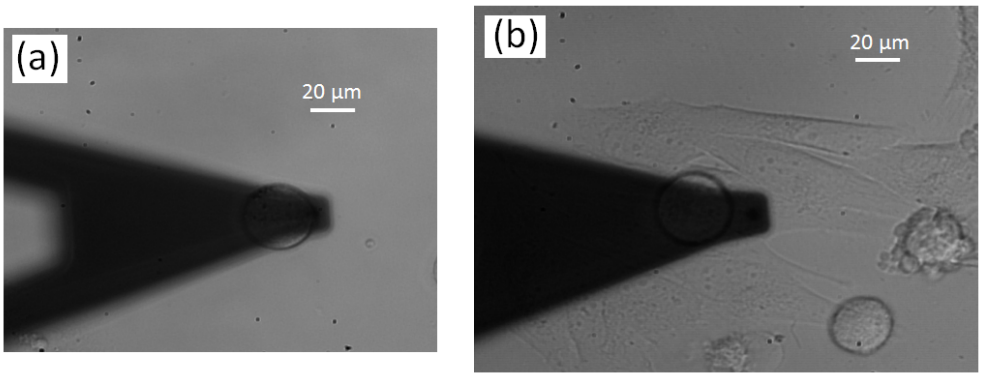

Figure 6.10: (a) is an optical microscope image of a single MDA-MB-231 breast cancer cell attached to a cantilever. (b) is an optical microscope image of the same MDA-MB-231 cell in contact with a confluent cluster of Saos-2 cells.

experiment an eleventh site was selected to investigate the adhesion dependency on dwell time. The z-piezo movement was dwelled after the trigger force of 1 nN was reached and ten force curves were collected for each of a range of dwell times (0 seconds, 1 second, 2 seconds, 5 seconds and 10 seconds). This was done at the end of each experiment which resulted in dwell dependency data for 3 different dwell sites for each of the 3 sets of treated cells (untreated, zoledronic acid treated and anti-N-cadherin treated). The ten curves for each dwell time were then averaged and plotted against dwell time. Viability of the probe cell was checked at the end of each experiment by lowering the cell to the substrate and moving the cantilever so that the attached cell was 'rolled' and was visible via the inverted microscope objective to ensure the cell membrane was intact and that the cell was not apoptotic.

6.4.2 Data Analysis

The adhesion data for each of the three treatments was analysed using the Asylum Research software in IgorPro. There are a number of ways in which the adhesion data can be analysed to extract information about the adhesive interaction be-

tween the cells. The most straight forward method is extracting the detachment force from the data. The detachment force is the maximum force required to separate the two cells from one another and is shown in figure 6.11. Another way of

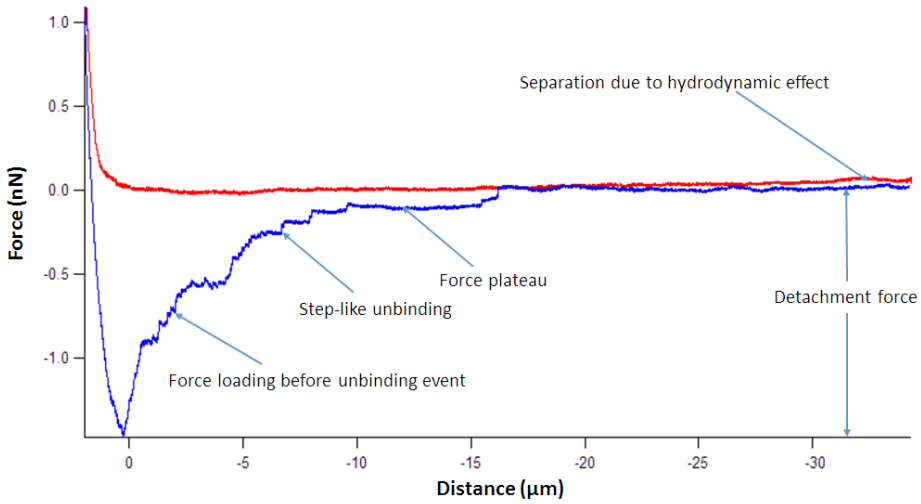

Figure 6.11: A typical adhesion data force curve showing how the detachment force was extracted from the data.

analysing the data is to integrate the area beneath the non-contact line to calculate the energy required to separate the two cells from each other. This is also known as the work done required to detach the two cells from each other [59]. This is more difficult to analyse due to the multiple number of events associated with the unbinding of two living cells as shown in figure 6.11. These individual unbinding events can also be characterised and measured to determine the different types of unbinding event and the size of each event. In figure 6.11 step like events can be seen as the two cells are separated. These steps either appear to have a small ramp feature indicating a loading force or a long plateau like feature which may represent a tether being pulled from the cell membrane with no increase in loading force. It is not possible to tell whether single or multiple unbinding events are taking place simultaneously which makes this form of analysis very difficult.

The size of these small events cannot be directly related to specific ligand-receptor unbinding since there is much more involved such as the attachment of the tethers to the cell membrane and the changing shape of the membranes of both cell types during separation. It is for this reason I have focused solely on the detachment force in this analysis.

The Asylum Research software calculates the detachment force by averaging the last ten points of the retract data and subtracting the minimum value of the retract data. This is why it is vital to ensure the two cells are fully detached otherwise the recorded detachment value is measured to be lower than the actual value.

The detachment force was measured for each individual force curve collected for each of the three different cell treatment experiments. The data was then represented as histograms showing the distribution of detachment forces for each of the three treatments. The data was also graphed against time to investigate any time dependent effect the treatments had on the detachment force. The dwell dependency data was also graphed to show how the detachment force varied with dwell time for the three individual treatments.

6.4.3 Results and Discussion

Once the detachment force was measured for each force curve the measurements were shown in the form of histograms for each treatment investigated. These histograms appeared to show a slightly positive skew in the data for each treatment. For this reason the average detachment force for each treatment was expressed as a median ± median absolute deviation as shown in table 6.1. The average detachment forces for the three treatments were 160 ± 49 pN, 140 ± 50 pN and 100 ± 27 pN for the untreated, anti-N-cadherin treated and zoledronic acid treated

cells respectively. A separate histogram for each treatment is shown in figure 6.12 and it can be clearly seen that the zoledronic acid treated cells show a significant decrease in detachment force shown by a shift to the left and the spread of the distribution is also visibly smaller than for the untreated and anti-N-cadherin treated cells. There is also a shift to the left in the anti-N-cadherin treated cells when comparing with the untreated.

Table 6.1: Comparison of the median detachment force required to separate MDA-MB-231 probe cells from Saos-2 cells for untreated, zoledronic acid treated and anti-N-cadherin treated cells. Results are shown as median ± median absolute deviation.

	Untreated	Anti-N-cadherin	Zoledronic acid
Detachment force (pN)	160 ± 49	140 ± 50	100 ± 27

The Wilcoxon rank test showed there was a statistically significant reduction in the detachment force for the zoledronic acid treated cells when compared with the untreated and anti-N-cadherin treated cells ($p<0.01$ for both comparisons). The Wilcoxon rank test also showed that the anti-N-cadherin treatment significantly reduced the detachment force required to separate the two cell types ($p<0.05$) compared with the untreated cells. These results show an overall value for the effects of the different treatments on the interaction between the two cell types, however the time dependent effect of the treatment response is not considered in this analysis. Any time dependent effect the treatment may have had on the cells was analysed by displaying the data for each individual experiment as a graph of the measured detachment force values against time. These are shown in figures 6.13, 6.14 and 6.15.

The detachment force versus time graphs show that the measured detachment forces for the untreated cells are consistent across the 3 experimental repeats.

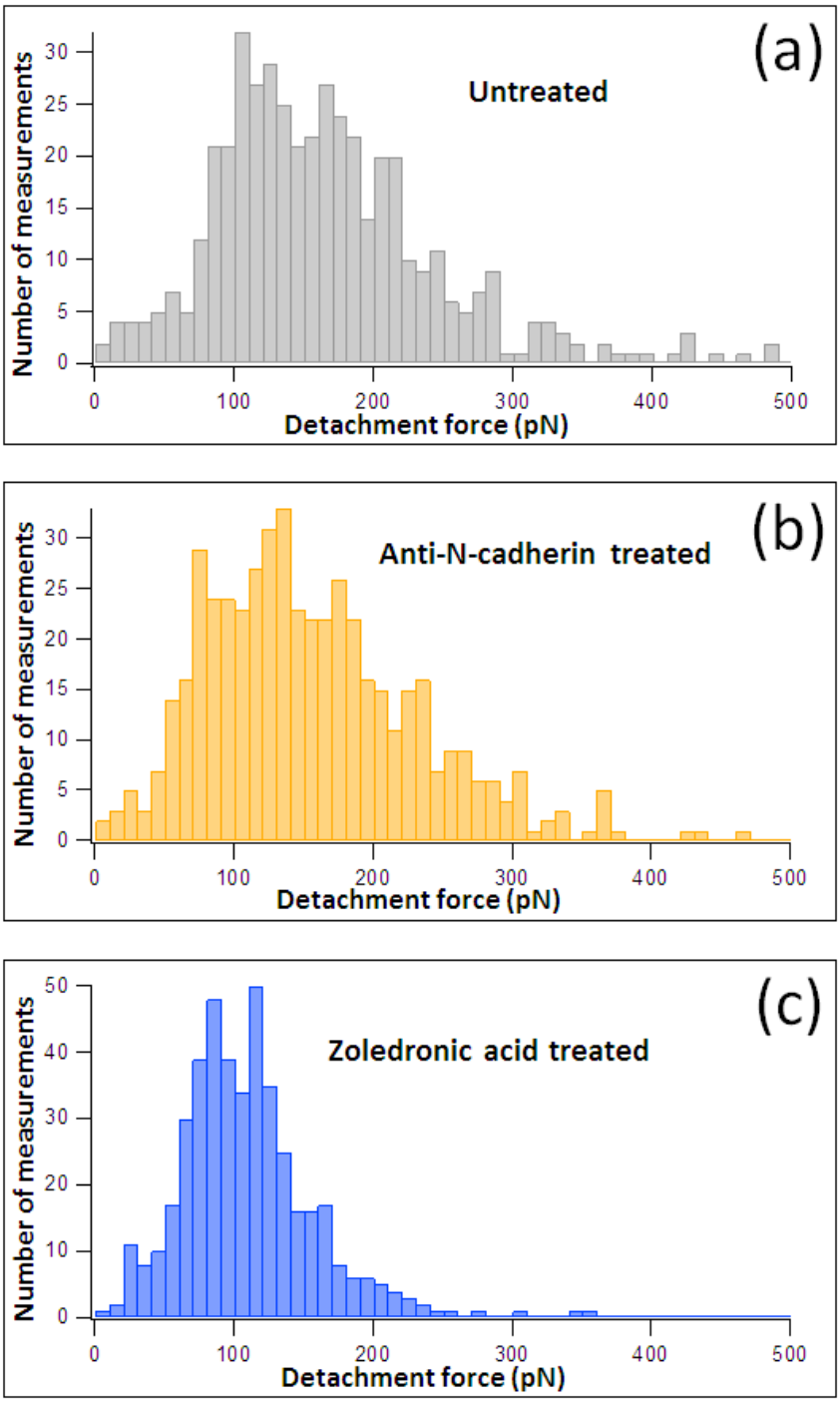

Figure 6.12: Multiple histograms showing the distribution of measured detachment forces required to separate single MDA-MB-231 probe cells from confluent Saos-2 cell monolayers for untreated, (a), anti-N-cadherin treated, (b), and zoledronic acid treated, (c), cells. It can be seen from the histograms that the zoledronic acid treated cells showed the largest decrease in detachment force during these experiments.

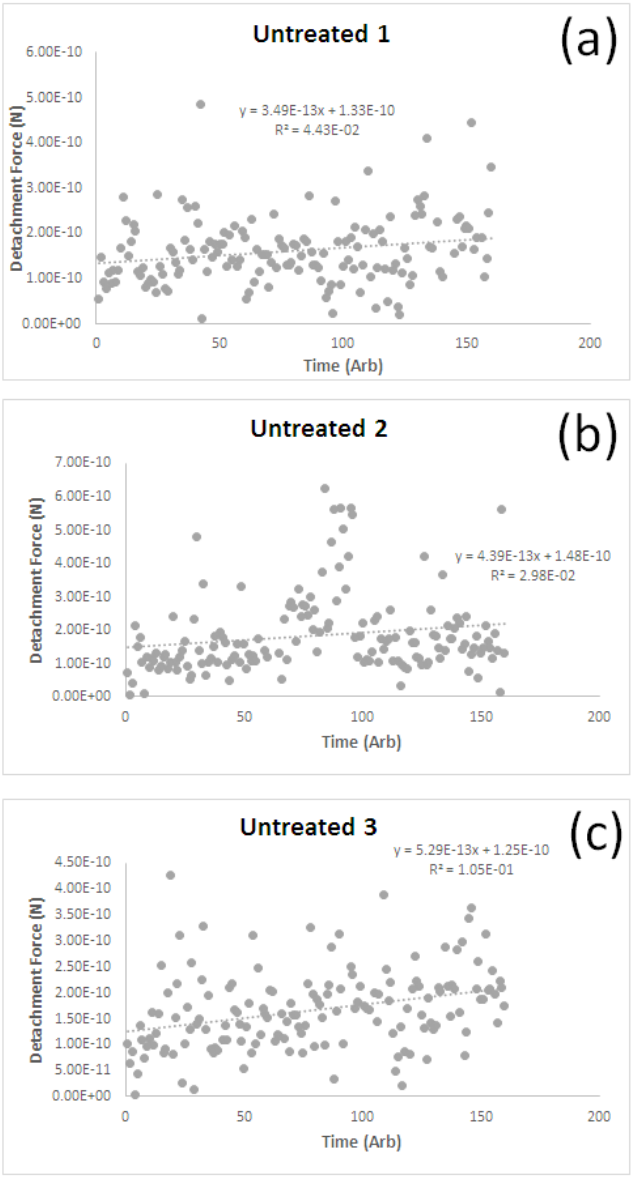

Figure 6.13: Graphs showing the detachment force measured as a function of time for the untreated cells. The detachment forces were plotted in the order they were acquired so the time is shown in arbitrary units. (a), (b) and (c) are the first, second and third experiments respectively. It can be seen that the detachment values for the untreated cells are initially around 150 pN and gradually rise to approximately 200 pN during the two hours it took to acquire the data.

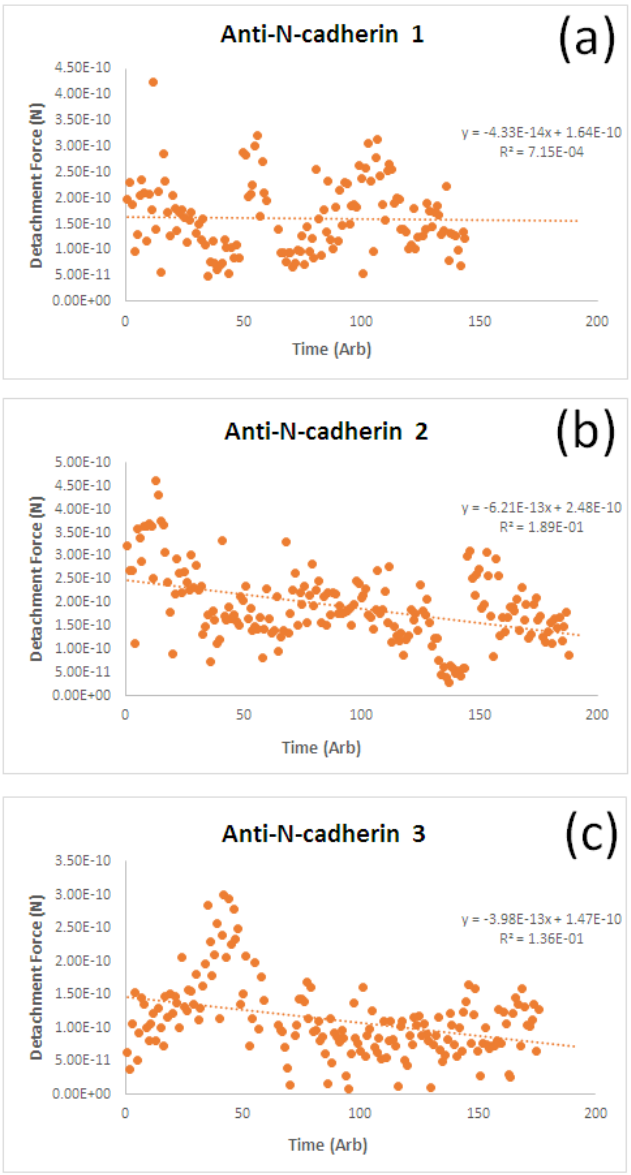

Figure 6.14: Graphs showing the detachment force measured as a function of time for the anti-N-cadherin treated cells. The detachment forces were plotted in the order they were acquired so the time is shown in arbitrary units. (a), (b) and (c) are the first, second and third experiments respectively. It can be seen that the detachment values for the anti-N-cadherin treated cells are initially around 150 pN in (a) and (c) however they are approximately at 250 pN in (b). All three graphs do appear to show a similar trend of decreasing detachment force values over time and after the two hours taken to acquire the data the detachment values are somewhere in the region between 100 pN and 150 pN.

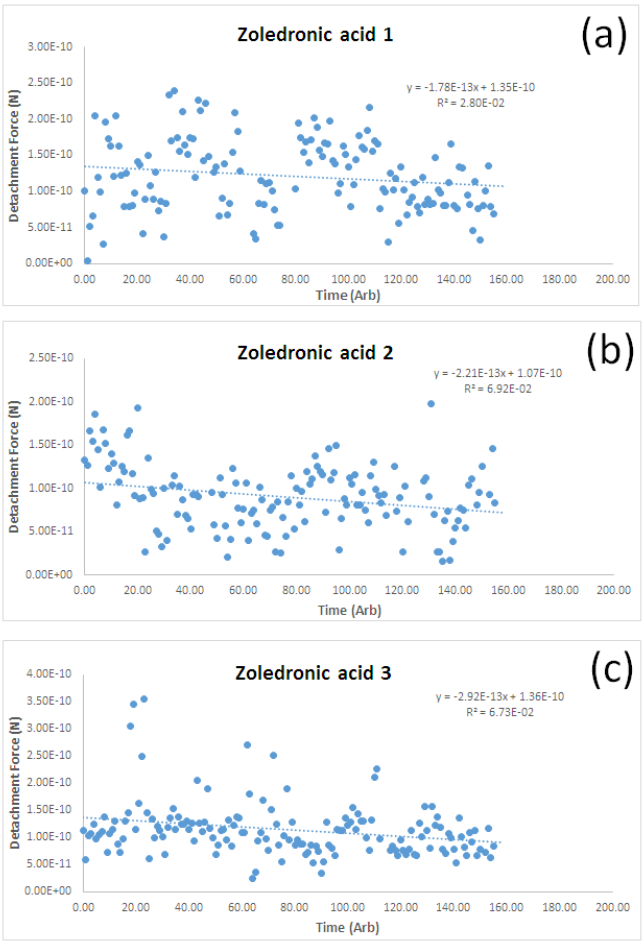

Figure 6.15: Graphs showing the detachment force measured as a function of time for the zoledronic acid treated cells. The detachment forces were plotted in the order they were acquired so the time is shown in arbitrary units. (a), (b) and (c) are the first, second and third experiments respectively. It can be seen that the detachment values for the zoledronic acid treated cells are initially around 120 pN for all graphs. All three graphs then show a similar trend of decreasing detachment force values over time and after the two hours taken to acquire the data the detachment values are somewhere in the region between 50 pN and 100 pN.

They each show a similar trend of increasing values throughout the two hours of force curve capture and the Wilcoxon rank test showed no significant difference between the three experiments ($p>0.05$) for all comparisons. This increase in detachment force as a function of time may have been due to a slight increase in temperature of the media due to the experimental setup during the experiments. For the zoledronic acid and anti-N-cadherin treated cells there is a gradual decrease in detachment force with time. At the start of these experiments it is important to note that the cells have already been incubated at room temperature in their respective treated media for 30 min plus an additional 15 min cantilever calibration and cell attachment and so the treatment will have started to take effect on the cells. At the start of the force curve acquisition the zoledronic acid treated cells appear to have the lowest detachment force values meaning at room temperature (approximately 29 °C in the AFM lab) the zoledronic acid treatment significantly reduced the detachment force of the two cells by a greater amount over the initial 45 min (approximately) than the anti-N-cadherin treatment. The anti-N-cadherin treatment, however, appeared to have a greater effect on the rate at which the detachment force decreased over the 2 h in which the force curve data was acquired. The anti-N-cadherin treated cells results also showed a lot of variation over the three experimental repeats. This may have been due to the concentration of anti-N-cadherin antibody used. The 20 μg.mL^{-1} concentration used was the recommended manufacturers concentration however further experiments to investigate if increasing concentrations of antibody reduces the detachment force further would be of use.

The dwell dependency data is shown in figure 6.16 in which typical force curves are shown for increasing dwell times over the same position in (a) and (b) shows the dwell dependency data for the three treatments. Each data point is an aver-

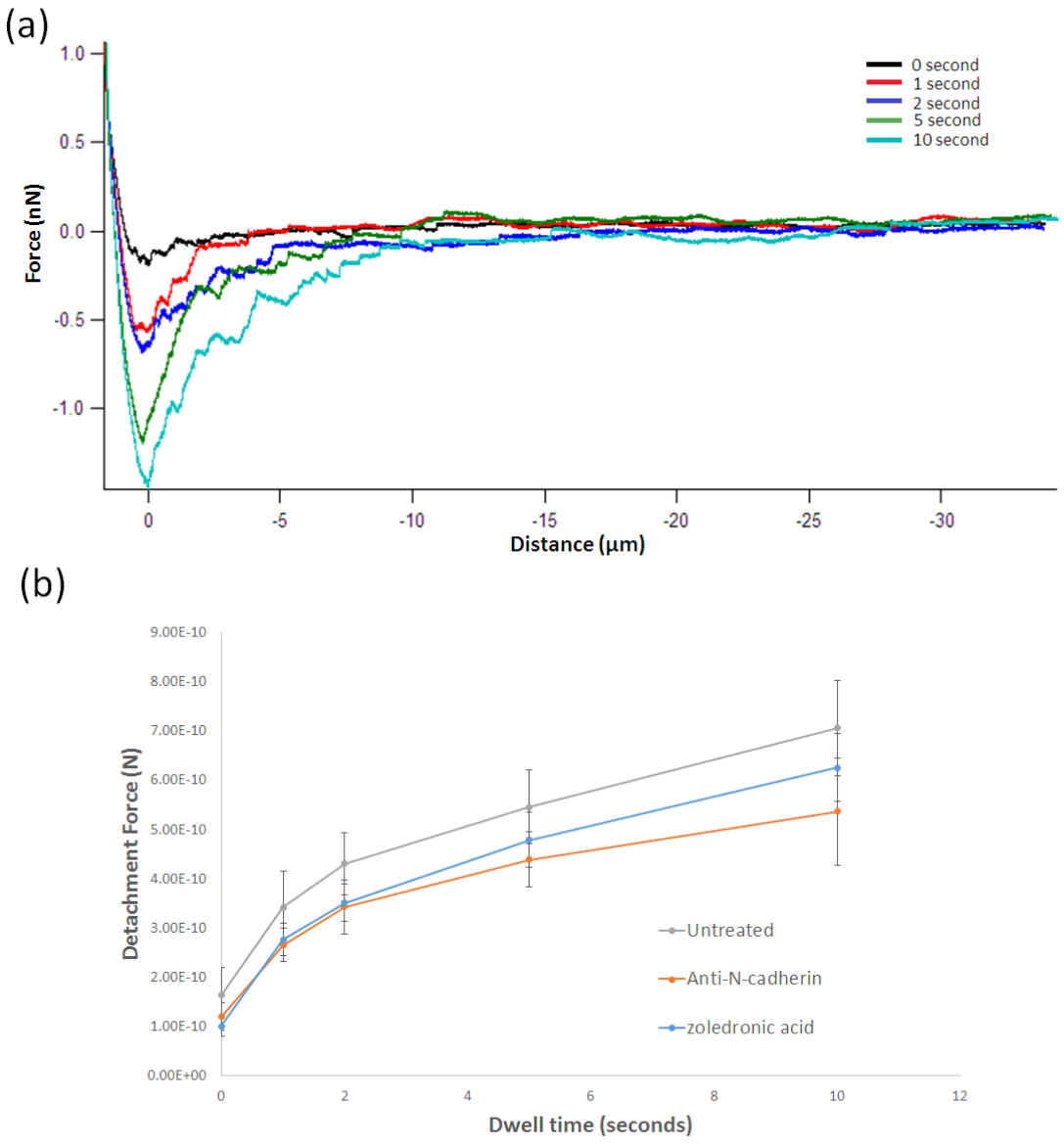

Figure 6.16: (a) Multiple force curves showing the increase in detachment force with increasing dwell times. (b) is a graph showing the dwell dependency results for the 3 cell treatments investigated.

age of 10 points for each of three experimental repeats for each dwell time. These measurements were performed at the end of each experiment so approximately three hours after the cells were treated. It is difficult to draw any statistical conclusions from such a small dataset since only 3 separate locations with 3 separate probe cells for each treatment have been measured here, however even with this small sample the treated cells average detachment forces both show a reduction in detachment force compared with the untreated for all dwell times investigated. These results also show that the detachment force increases with contact time. This could be due to the strengthening of the adhesion bonds between the two cell types over this time as well as an increase in contact area during this dwell as the cells 'relax'.

Overall the results show that zoledronic acid treatment of the MDA-MB-231 and Saos-2 cells significantly reduces the force required to detach these cells from one another. This is in agreement with previous studies which showed that zoledronic acid treatment significantly decreased the adhesive interaction between metastatic prostate cancer cells and bone marrow endothelial (BME) cells [125] highlighted earlier in this chapter. The anti-N-cadherin treated MDA-MB-231 and Saos-2 cells also showed a significant reduction in the force required to detach themselves from one another which is as expected since N-cadherin is known for its role in cell-cell adhesion and by inhibiting this specific binding it was expected that the detachment force would decrease.

6.4.4 Conclusion

It is clear from the results that the zoledronic acid and anti-N-cadherin treated cells show significantly reduced detachment forces and that these reductions are time dependent. They may also be dose dependent and these are two areas where

this work could be advanced. Due to time restraints I was unable to investigate the effect of different concentrations of these treatments on the cellular adhesion nor was I able to investigate how the detachment force changed over greater periods of time than have been shown here. It is possible that by investigating these interactions for longer periods of time (> 2 h) that the cells may show some kind of active response to the treatment and detachment forces may increase again as the cell 'recovers'.

These results also support the findings that zoledronic acid treatment has been shown to reduce bone resorption and bone metastases in breast cancer patients. The findings in this chapter highlight one of the possible mechanisms of this treatment. Zoledronic acid treatment appears to affect the cell signalling within the bone micro-environment via reduced cellular adhesion between metastatic breast cancer cells and osteoblast-like cells in this instance. It may be the case that this treatment affects metastatic breast cancer cells from signalling with other cells found in the bone micro-environment. Investigating the adhesive interaction between the MDA-MB-231 and BME cells would possibly give an insight into the extravasation stage of metastasis. The zoledronic acid treatment may reduce the metastatic cells chances of extravasation in which case it may have the potential to be used to prevent breast cancer metastasis.

6.5 Summary

This chapter has described the development of a single cell force spectroscopy (SCFS) AFM setup for use on the Asylum MFP-3D. The setup was developed so that the adhesive interaction between metastatic breast cancer cells and cells contained within the bone micro-environment could be investigated and quan-

tified. The interaction between metastatic MDA-MB-231 breast cancer cells and 'osteoblast-like' Saos-2 cells has been successfully characterised for untreated, zoledronic acid treated and anti-N-cadherin treated cells. In particular the results presented here may have highlighted one of the mechanisms by which adjuvant zoledronic acid treatment of breast cancer patients reduces bone resorption and metastases.

Chapter 7

Conclusions and Future Work

7.1 AFM Imaging of Living Breast Cancer Cells

In chapter 3 of this thesis experimental procedures were developed to image breast cancer cells in liquid using contact mode AFM imaging. A number of issues such as lateral forces exerted by the tip damaging the cells and tip artefacts due to cell height were addressed and it was found that by growing the cells on glass substrates as opposed to polystyrene, the cells became more 'spread' and were therefore easier to image using AFM. Used in conjunction with other imaging techniques such as fluorescence microscopy or confocal microscopy, AFM imaging is an important tool in the investigation of many cellular processes due to its ability to image living cells under near physiological conditions to high resolution. Imaging of cytoskeletal structures in thin spreading membrane regions of the breast cancer cells has been shown here. Topographical imaging of these intracellular components combined with force spectroscopy indentation techniques could be used to characterise the mechanical properties of individual cytoskeletal components and also potentially investigate the effects of specific treatments.

7.2 Biomechanical Characterisation of Breast Cancer Cells

In chapter 4 the mechanical properties of three breast cell lines were characterised using three separate mechanical contact models. The Hertz and Oliver Pharr models were two elastic models used and the third model was a viscoelastic extension of the Hertz model. The results of these characterisation experiments showed that the mechanical properties of the non-cancerous MCF-10A breast epithelial cells were significantly different from the two cancerous cell lines investigated (MCF-7 and MDA-MB-231 cell lines) with the MCF-10A cells being significantly 'stiffer' and significantly more viscous. This transformation in mechanical properties between non-cancerous and cancerous cells is believed to be part of a process called epithelial to mesenchymal transition (EMT) in which the cells lose expression of E-cadherin, which is essential to tissue homeostasis, and gain expression of N-cadherin, which is involved in mesenchymal cell migration. Once contact inhibition is lost in the primary site tumour cells are able to migrate and invade the vasculature before circulating the body and potentially arresting at a secondary site where some of the cells are able to form secondary tumours. The results of the mechanical characterisation experiments in this work support this theory in that the cancerous cells definitely appear to have particular mechanical advantages over non-cancerous cells in their ability to be deformed which could be an explanation as to how they are able to invade the vasculature and eventually form secondary tumours.

The mechanical characterisation experiments failed to show any correlation between the varying malignancies of the two breast cancer cell lines examined in this work. By that it is meant that it was hypothesised that due to the MDA-MB-231

cells increased metastatic potential when compared with the MCF-7 cells it was expected that the MDA-MB-231 cells mechanical properties would show increased deformability when compared with the MCF-7 cells. The fact that they did not in the results presented here does not rule out the hypothesis that metastatic potential correlates with mechanical deformability entirely. It may be the case that below a certain threshold value, regardless of how deformable the cells may be they are still able to become invasive. Their survival in circulation and ability to form secondary tumours at a distant site may then be down to other limiting factors such as their ability to survive and the expression of particular markers that allow attachment to the endothelium at specific secondary locations. This is supported by the Oliver Pharr model results showing no significant difference between the two cell lines mechanical properties. This particular model is currently being used by one group developing a diagnostic AFM tool to be able to diagnose cancerous tissue from non-cancerous tissue in breast biopsies using AFM indentation techniques similar to those presented here [41]. This example highlights the importance of these experiments in the understanding of mechanical properties of cancerous and non-cancerous cells and shows a useful and important application of research into the mechanical characterisation of living cells. In the case of use in a diagnostic device for the identification of cancerous tissue the Oliver Pharr model gives more of an elastic measurement than the Hertz model and the time taken to acquire and analyse experimental data is much less than it would be for an investigation into the viscoelastic properties making it a useful contact model to use for this specific application.

Developing the fluorescence microscope used in conjunction with the AFM to capture confocal images would increase the spatial resolution of the fluorescence data captured which would give an important insight into the dissipation of forces

applied by indentation studies and also the cytoskeletal restructuring that is undergone during such measurement techniques. This would also allow us to visualise the regions of living cells being indented during the mechanical characterisation experiments so that the most appropriate contact model could be used to extract the cellular mechanical properties from the data.

7.3 Biomechanical Characterisation of Breast Cancer Stem Cells

In chapter 5 sub-populations of 'stem-like' ALDH^{high} MDA-MB-231 cells were identified *in vitro* and were shown to possess increased metastatic potential over 'non-stem-like' ALDH^{low} MDA-MB-231 cells using functionality assays. The mechanical properties of these sub-populations of MDA-MB-231 cells were then investigated using the force spectroscopy techniques developed in chapter 4. The results showed that there was no significant difference between the different sub-populations in all but the Hertz model results, which appeared to show the ALDH^{high} sub-population being significantly more deformable than the ALDH^{low}/ 'normal' sub-population. It was concluded from this study that although increased ALDH expression appears to be associated with increased metastatic capacity in breast cancer cells, it does not appear to correlate with the mechanical properties of the cells. ALDH expression is therefore hypothesised to be involved in the survival of cells in circulation which would explain why cells with high ALDH expression have been shown to be significantly more likely to form secondary tumours *in vivo* [102] and show significant resistance to chemotherapy and radiation treatments [104].

7.4 Single Cell Force Spectroscopy

Chapter 6 described the development of a SCFS setup to investigate the interaction between breast cancer cells and cells from the bone micro-environment. The force required to detach metastatic MDA-MB-231 cells from 'osteoblast-like' Saos-2 cells was measured for untreated, zoledronic acid treated and anti-N-cadherin treated cells. Both treatments showed a significant reduction in the force required to detach the two cell lines for the particular loading/unloading speed and triggered loading force used in the experiments. These results highlight one mechanism by which adjuvant zoledronic acid treatment may reduce bone resorption and metastases in breast cancer patients. The reduction in detachment force after treating the cells with anti-N-cadherin antibodies also shows that N-cadherin is one of the adhesion molecules involved in the interaction between metastatic breast cancer cells and osteoblasts in the bone micro-environment. This result shows how SCFS can be used to identify the involvement of specific adhesion molecules involved in cell-cell adhesion. Further experiments could be performed on these cell lines to identify a number of other cell adhesion molecules involved in cellular signalling between these cell types.

This setup could also be used to investigate the adhesive interaction between the MDA-MB-231 cells and the BME cells to simulate the extravasation stage of metastasis at the secondary site to identify adhesion molecules involved in the attachment of circulating tumour cells to the endothelial cells in the bone. By identifying molecules involved in this attachment stage and the resulting interactions within the bone micro-environment it may be possible to use this information in developing diagnostic and therapeutic regimes to address the problems of metastasis and hopefully one day prevent tumour cells from metastasising to bone and other secondary sites.

7.5 Concluding Remarks

Throughout this thesis Atomic Force Microscopy has been used as a tool to investigate mechanisms of breast cancer metastasis. Methods were initially developed to image live cells in aqueous conditions using contact mode AFM. Force spectroscopy indentation type experiments were then developed to extract mechanical force versus indentation data from a range of breast cell lines and three mechanical contact models were used to analyse the data. By comparing three different analytical models it has been shown how important it is to consider what mechanical properties are being extracted from the live cells before choosing the appropriate analytical model.

The development of a SCFS setup using the Asylum MFP-3D AFM has allowed adhesion measurements between two separate cells to be quantified with high enough force resolution to identify significant differences between cells that have undergone specific treatments.

I feel that the work presented in this thesis provides a contribution to the development of techniques and experimental protocol used to investigate living cells, particularly breast cancer cells, and that the results from the AFM experiments presented in this thesis enhance existing knowledge on the mechanical characterisation of living cells and SCFS experiments as well as an improved understanding of the interaction between breast cancer cells and cells within the bone microenvironment during breast cancer metastasis.

Chapter 8

Appendices

8.1 Appendix 1: IgorPro Code

8.1.1 Calculating Sample Height from the Contact Point

Below is the code adapted by Ross Carter from the Asylum Research code used in all height maps throughout this thesis to determine the height from the contact point of indentation as opposed to the triggered depth of indentation.

```
Function FMapCalcContactPoint2(Data,DataB,ParmWave)
        Wave Data                                   //Raw (z displacement)
        Wave/Z DataB                          //Deflection
        Wave/Z ParmWave          //not used


        variable surfindex = FindSurfaceIndex(DataB,Data,10)


        return(-Data[surfindex])
End


Function/S FMapCalcContactPoint2Info()

        String Output = "DataType:Raw;Section:Ext;DataTypeB:Defl;ParmWave:None;CalcType:Height;"
        return(output)
End
```

8.1.2 Extracting Stiffness Data from Force Mapping

The next piece of code is a function written by myself to extract the stiffness from the data. The code fits a straight line to the data and returns a value for the stiffness in N m^{-1}.

```
Function FMapCalcStiffness(Data,DataB,ParmWave)
        Wave Data
        Wave/Z DataB
        Wave/Z ParmWave


        Variable Output = 1/SlopeCurveFuncJake(Data,DataB) // changed to 1/
        if (Output<0)
                Output = 0.02                                           // Execute if condition is TRUE

                                                                // Optionally execute if condition is FALSE
        endif
        return(Output)


End //FMapCalcInvols


Function/S FMapCalcStiffnessInfo()

        String Output = "DataType:Force;Section:Ret;DataTypeB:Ind;ParmWave:None;CalcType:Invols;"
        return(output)

End //FMapCalcInvolsInfo


Function SlopeCurveFuncJake(YData,XData)
        Wave YData, XData
        //Gutted version of HertzCurveFunc, that can be used on a FP by FP basis (for use with map calcing).


        String FPname = NameOfWave(YData)
        String DataFolder = GTS("FMapAnalyzeInput")


        String BaseName, Suffix, DataType, SectionStr
        ExtractForceWaveName(FPname,BaseName,Suffix,DataType,SectionStr)


        Variable LowRatio = .10
        Variable HighRatio = .90


        //OK, we need to get the correct section


        Variable FMax, Value, Index0, Index1, StartIndex, StopIndex, FMin

        FMax = WaveMax(YData)


        StrSwitch (SectionStr)
                case "Ext":
                        WaveStats/M=1/Q/R=[0,10] YData
                        break

                case "Ret":
                Default:
                        WaveStats/M=1/Q/R=[DimSize(YData,0)-10,DimSize(YData,0)-1] YData
                        break
        endswitch


        FMin = V_AVg

        Value = (FMax-FMin)*LowRatio+FMin
        FindLevel/B=5/P/Q/R=[0,DimSize(YData,0)-1] YData,Value
        Index0 = round(V_LevelX)

        Value = (FMax-FMin)*HighRatio+FMin
        FindLevel/B=5/P/Q/R=[0,DimSize(YData,0)-1] YData,Value
        Index1 = round(V_LevelX)

        if (IsNan(Index1))
                WaveStats/Q YData
                Index1 = round(x2pnt(YData,V_maxloc))
        endif



        StartIndex = Min(Index0,Index1)
        StopIndex = Max(Index0,Index1)

        Variable Slope, Intercept
        Poly1Fit(YData,XData,StartIndex,StopIndex,Slope,Intercept)

//      if (IsNan(Slope))
//              print Slope
```

```
//      endif

        return(Slope)
End //SlopeCurveFunc
```

8.1.3 Extracting Exponential Fit Coefficients From Force Mapping to Calculate Apparent Viscosity

The subsequent functions were written by myself to fit an exponential curve to the stress relaxation data and extract the coefficients of this fit. Three functions were required for each of the three parameters to be extracted as shown below.

```
Function FMapCalcExpTAU(Data,DataB,ParmWave)
        Wave Data
        Wave/Z DataB
        Wave/Z ParmWave


        Variable Output = expFuncTAUJake(Data,DataB)
        return(Output)


End //FMapCalcInvols


Function/S FMapCalcExpTAUInfo()

        String Output = "DataType:Force;Section:Ext;DataTypeB:Time;ParmWave:None;CalcType:Invols;"
        return(output)

End //FMapCalcInvolsInfo


Function expFuncTAUJake(YData,XData)
        Wave YData, XData
        //Gutted version of HertzCurveFunc, that can be used on a FP by FP basis (for use with map calcing).


        String FPname = NameOfWave(YData)
        String DataFolder = GTS("FMapAnalyzeInput")


        String BaseName, Suffix, DataType, SectionStr
        ExtractForceWaveName(FPname,BaseName,Suffix,DataType,SectionStr)

        //OK, we need to get the correct section

        Variable FMax, FMin

        CurveFit/M=2/W=0 exp_XOffset, YData [0,4000] /X= XData[0,4000]/D

        Wave W_Coef

        return W_Coef[2]


End



Function FMapCalcExpY0(Data,DataB,ParmWave)
        Wave Data
        Wave/Z DataB
        Wave/Z ParmWave
```

```
        Variable Output = expFuncY0Jake(Data,DataB)
        return(Output)


End //FMapCalcInvols


Function/S FMapCalcExpY0Info()

        String Output = "DataType:Force;Section:Ext;DataTypeB:Time;ParmWave:None;CalcType:Invols;"
        return(output)

End //FMapCalcInvolsInfo



Function expFuncY0Jake(YData,XData)
        Wave YData, XData
        //Gutted version of HertzCurveFunc, that can be used on a FP by FP basis (for use with map calcing).


        String FPname = NameOfWave(YData)
        String DataFolder = GTS("FMapAnalyzeInput")


        String BaseName, Suffix, DataType, SectionStr
        ExtractForceWaveName(FPname,BaseName,Suffix,DataType,SectionStr)

        //OK, we need to get the correct section

        Variable FMax, FMin
        SetAxis/A
        CurveFit/M=2/W=0 exp_XOffset, YData [0,4000] /X= XData[0,4000]/D

        Wave W_Coef

        return W_Coef[0]



End



Function FMapCalcExpA(Data,DataB,ParmWave)
        Wave Data
        Wave/Z DataB
        Wave/Z ParmWave


        Variable Output = expFuncAJake(Data,DataB)
        return(Output)


End //FMapCalcInvols


Function/S FMapCalcExpAInfo()

        String Output = "DataType:Force;Section:Ext;DataTypeB:Time;ParmWave:None;CalcType:Invols;"
        return(output)

End //FMapCalcInvolsInfo



Function expFuncAJake(YData,XData)
        Wave YData, XData
        //Gutted version of HertzCurveFunc, that can be used on a FP by FP basis (for use with map calcing).


        String FPname = NameOfWave(YData)
        String DataFolder = GTS("FMapAnalyzeInput")


        String BaseName, Suffix, DataType, SectionStr
        ExtractForceWaveName(FPname,BaseName,Suffix,DataType,SectionStr)

        //OK, we need to get the correct section

        Variable FMax, FMin

        CurveFit/M=2/W=0 exp_XOffset, YData [0,4000] /X= XData[0,4000]/D

        Wave W_Coef

        return W_Coef[1]
```

End

8.2 Appendix 2: Extended Z-stage Linearity

The linearity of the extended z-stage (P-621.ZCL PIHera precision Z stage, Physik Instrumente) was initially checked using a signal generator. The signal generator was used to drive the extended z-piezo with a 500 mV peak to peak sine wave at a frequency of 5 Hz. The 'normal' AFM head was then used to image the oscillating extended stage over a 0 μm scansize at a rate of 1 Hz so that multiple sine waves were captured in each scan line. An image was captured for a range of DC offset voltages over the whole of the scanners voltage range. The images were then flattened and the peak to peak height of the sine wave images was recorded and an average value calculated for each offset voltage.

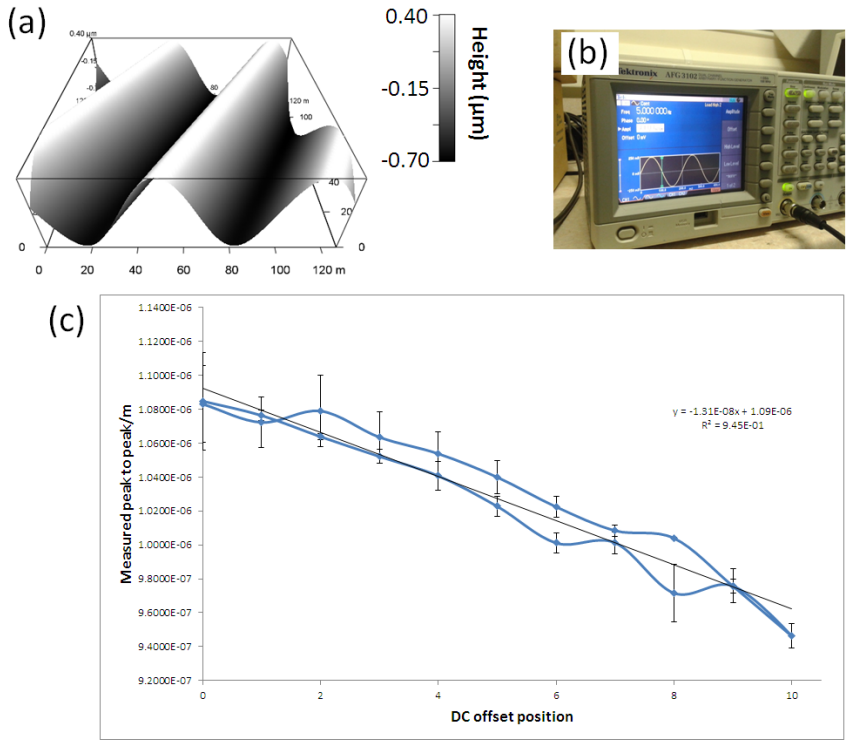

Figure 8.1: Images showing how the linearity of the scanner was tested. (a) is the contact mode image of the oscillating extended z-stage. (b) is the signal generator used to drive the extended z-stage and (c) is a graph showing the measured peak to peak height of the sine wave over the range of 110V.

Bibliography

[1] M. Knowles and P. Selby, *Cellular and Molecular Biology of Cancer*. Oxford: Oxford University Press, fourth ed., 2005.

[2] J. Muller, *On the Nature and Structural Characteristics of Cancer*. London: Sherwood, Gilbert and Piper, 1836.

[3] D. Hanahan and R. A. Weinberg, "Hallmarks of cancer: the next generation.," *Cell*, vol. 144, pp. 646–74, Mar. 2011.

[4] C. J. Sherr and F. McCormick, "The RB and p53 pathways in cancer.," *Cancer cell*, vol. 2, pp. 103–12, Aug. 2002.

[5] D. L. Burkhart and J. Sage, "Cellular mechanisms of tumour suppression by the retinoblastoma gene.," *Nature reviews. Cancer*, vol. 8, pp. 671–82, Sept. 2008.

[6] M. Collado and M. Serrano, "Senescence in tumours: evidence from mice and humans.," *Nature reviews. Cancer*, vol. 10, pp. 51–7, Jan. 2010.

[7] A. Swat, I. Dolado, J. M. Rojas, and A. R. Nebreda, "Cell density-dependent inhibition of epidermal growth factor receptor signaling by p38alpha mitogen-activated protein kinase via Sprouty2 downregulation.," *Molecular and cellular biology*, vol. 29, pp. 3332–43, June 2009.

[8] T. Okada, M. Lopez-Lago, and F. G. Giancotti, "Merlin/NF-2 mediates contact inhibition of growth by suppressing recruitment of Rac to the plasma membrane.," *The Journal of cell biology*, vol. 171, pp. 361–71, Oct. 2005.

[9] M.-H. Lee, P.-H. Wu, J. R. Staunton, R. Ros, G. D. Longmore, and D. Wirtz, "Mismatch in mechanical and adhesive properties induces pulsating cancer cell migration in epithelial monolayer.," *Biophysical journal*, vol. 102, pp. 2731–41, June 2012.

[10] J. Xu, S. Lamouille, and R. Derynck, "TGF-beta-induced epithelial to mesenchymal transition.," *Cell research*, vol. 19, pp. 156–72, Feb. 2009.

[11] S. Nakajima, R. Doi, E. Toyoda, T. Shoichiro, W. Michihiko, K. Masayuki, S. T. Sidhartha, I. Daisuke, K. Kazuhiro, M. Tomohiko, K. Yoshiya, F. Koji, H. Ryo, and I. Masayuki, "N-Cadherin Expression and Epithelial-Mesenchymal Transition in Pancreatic Carcinoma," *Clinical Cancer Research*, vol. 10, pp. 4125–4133, 2004.

[12] R. A. Gatenby, K. Smallbone, P. K. Maini, F. Rose, J. Averill, R. B. Nagle, L. Worrall, and R. J. Gillies, "Cellular adaptations to hypoxia and acidosis during somatic evolution of breast cancer.," *British journal of cancer*, vol. 97, pp. 646–53, Sept. 2007.

[13] X. Xu, B. Wang, C. Ye, C. Yao, Y. Lin, X. Huang, Y. Zhang, and S. Wang, "Overexpression of macrophage migration inhibitory factor induces angiogenesis in human breast cancer.," *Cancer letters*, vol. 261, pp. 147–57, Mar. 2008.

[14] K. J. Luzzi, I. C. MacDonald, E. E. Schmidt, N. Kerkvliet, V. L. Morris, A. F. Chambers, and A. C. Groom, "Multistep nature of metastatic inefficiency: dormancy of solitary cells after successful extravasation and limited survival of early micrometastases.," *The American journal of pathology*, vol. 153, pp. 865–73, Sept. 1998.

[15] Y. Hüsemann, J. B. Geigl, F. Schubert, P. Musiani, M. Meyer, E. Burghart, G. Forni, R. Eils, T. Fehm, G. Riethmüller, and C. A. Klein, "Systemic spread is an early step in breast cancer.," *Cancer cell*, vol. 13, pp. 58–68, Jan. 2008.

[16] C. Zhu, G. Bao, and N. Wang, "Cell Mechanics: Mechanical Response, Cell Adhesion, and Molecular Deformation," *Annual Review of Biomedical Engineering*, vol. 02, pp. 189–226, 2000.

[17] T. P. Butler and P. M. Gullino, "Quantitation of Cell Shedding into Efferent Blood of Mammary Adenocarcinoma Quantitation of Cell Shedding into Efferent Blood of Mammary," pp. 512–516, 1975.

[18] G. P. Gupta and J. Massagué, "Cancer metastasis: building a framework.," *Cell*, vol. 127, pp. 679–95, Nov. 2006.

[19] P. E. Porporato, V. L. Payen, J. Pérez-Escuredo, C. J. De Saedeleer, P. Danhier, T. Copetti, S. Dhup, M. Tardy, T. Vazeille, C. Bouzin, O. Feron, C. Michiels, B. Gallez, and P. Sonveaux, "A Mitochondrial Switch Promotes Tumor Metastasis," *Cell Reports*, pp. 1–13, July 2014.

[20] J. Kim, W. Yu, K. Kovalski, and L. Ossowski, "Requirement for specific proteases in cancer cell intravasation as revealed by a novel semiquantitative PCR-based assay.," *Cell*, vol. 94, pp. 353–62, Aug. 1998.

[21] A. F. Chambers, A. C. Groom, and I. C. MacDonald, "Dissemination and growth of cancer cells in metastatic sites.," *Nature reviews. Cancer*, vol. 2, pp. 563–72, Aug. 2002.

[22] S. Paget, "The distribution of secondary growths in cancer of the breast.," *Lancet*, vol. 1, pp. 571–573, 1889.

[23] D. Barkan, J. E. Green, and A. F. Chambers, "Extracellular matrix: a gatekeeper in the transition from dormancy to metastatic growth.," *European journal of cancer (Oxford, England : 1990)*, vol. 46, pp. 1181–8, May 2010.

[24] P. Mehlen and A. Puisieux, "Metastasis: a question of life or death.," *Nature reviews. Cancer*, vol. 6, pp. 449–58, June 2006.

[25] Cancer Research UK, "Breast cancer statistics," 2014.

[26] Cancer Research UK, "Statistics on the risk of developing cancer," 2012.

[27] L. J. Suva, R. J. Griffin, and I. Makhoul, "Mechanisms of bone metastases of breast cancer.," *Endocrine-related cancer*, vol. 16, pp. 703–13, Sept. 2009.

[28] R. E. Coleman, "Metastatic bone disease: clinical features , pathophysiology and treatment strategies," *Cancer tratment reviews*, vol. 27, pp. 165–176, 2001.

[29] J. G. Schneider, S. R. Amend, and K. N. Weilbaecher, "Integrins and bone metastasis: integrating tumor cell and stromal cell interactions.," *Bone*, vol. 48, pp. 54–65, Jan. 2011.

[30] M. Al-Hajj, M. S. Wicha, A. Benito-Hernandez, S. J. Morrison, and M. F. Clarke, "Prospective identification of tumorigenic breast cancer cells.," *Proceedings of the National Academy of Sciences of the United States of America*, vol. 100, pp. 3983–8, Apr. 2003.

[31] G. Binnig, C. F. Quate, and C. Gerber, "Atomic Force Microscope," *Physical Review Letters*, vol. 56, no. 9, p. 930, 1986.

[32] H.-J. Butt, B. Cappella, and M. Kappl, "Force measurements with the atomic force microscope: Technique, interpretation and applications," *Surface Science Reports*, vol. 59, pp. 1–152, Oct. 2005.

[33] J. L. Hutter and J. Bechhoefer, "Calibration of atomic-force microscope tips," *Review of Scientific Instruments*, vol. 64, no. 7, p. 1868, 1993.

[34] R. Proksch, T. E. Schäffer, J. P. Cleveland, R. C. Callahan, and M. B. Viani, "Finite optical spot size and position corrections in thermal spring constant calibration," *Nanotechnology*, vol. 15, pp. 1344–1350, Sept. 2004.

[35] H.-J. Butt and M. Jaschke, "Calculation of thermal noise in atomic force microscopy," *Nanotechnology*, vol. 1, pp. 1–7, 1995.

[36] K. D. Costa, "Single-cell elastography: Probing for disease with the atomic force microscope," *Disease Markers*, vol. 19, no. 2-3, pp. 139–154, 2003.

[37] Q. S. Li, G. Y. H. Lee, C. N. Ong, and C. T. Lim, "AFM indentation study of breast cancer cells.," *Biochemical and biophysical research communications*, vol. 374, pp. 609–13, Oct. 2008.

[38] E. G. Herbert, G. M. Pharr, W. C. Oliver, B. N. Lucas, and J. L. Hay, "On the measurement of stressstrain curves by spherical indentation," *Thin Solid Films*, vol. 398-399, pp. 331–335, Nov. 2001.

[39] M. Loparic, D. Wirz, A. U. Daniels, R. Raiteri, M. R. VanLandingham, G. Guex, I. Martin, U. Aebi, and M. Stolz, "Micro- and Nanomechanical Analysis of Articular Cartilage by Indentation-Type Atomic Force Microscopy: Validation with a Gel-Microfiber Composite," *Biophysical Journal*, vol. 98, pp. 2731–2740, June 2010.

[40] M. Stolz, R. Raiteri, A. U. Daniels, M. R. VanLandingham, W. Baschong, and U. Aebi, "Dynamic elastic modulus of porcine articular cartilage determined at two different levels of tissue organization by indentation-type atomic force microscopy.," *Biophysical journal*, vol. 86, pp. 3269–83, May 2004.

[41] M. Plodinec, M. Loparic, C. A. Monnier, E. C. Obermann, R. Zanetti-Dallenbach, P. Oertle, J. T. Hyotyla, U. Aebi, M. Bentires-Alj, R. Y. H. Lim, and C.-A. Schoenenberger, "The nanomechanical signature of breast cancer.," *Nature nanotechnology*, vol. 7, pp. 757–65, Nov. 2012.

[42] W. Oliver and G. Pharr, "An improved technique for determining hardness and elastic modulus using load and displacement sensing indentation experiments," *Journal of Materials Research*, vol. 7, no. 6, pp. 1564–1583, 1992.

[43] I. N. Sneddon, "The relation between load and penetration in the axisymmetric boussinesq problem for a punch of arbitrary profile," *International Journal of Engineering Science*, vol. 3, no. 638, pp. 47–57, 1965.

[44] K. L. Johnson, K. Kendall, and A. D. Roberts, "Surface Energy and the Contact of Elastic Solids," *Proceedings of the Royal Society of London. A. Mathematical and Physical Sciences*, vol. 324, pp. 301–313, Sept. 1971.

[45] B. Derjaguin, V. Muller, and Y. Toporov, "Effect of contact deformations on the adhesion of particles," *Journal of Colloid and Interface Science*, vol. 53, pp. 314–326, Nov. 1975.

[46] A. N. Ketene, E. M. Schmelz, P. C. Roberts, and M. Agah, "The effects of cancer progression on the viscoelasticity of ovarian cell cytoskeleton structures.," *Nanomedicine : nanotechnology, biology, and medicine*, vol. 8, pp. 93–102, Jan. 2012.

[47] E. M. Darling, S. Zauscher, and F. Guilak, "Viscoelastic properties of zonal articular chondrocytes measured by atomic force microscopy.," *Osteoarthritis and cartilage / OARS, Osteoarthritis Research Society*, vol. 14, pp. 571–9, June 2006.

[48] S. G. Shroff, D. R. Saner, and R. Lal, "Dynamic micromechanical atria1 myocytes measured properties of cultured rat by atomic force microscopy," *American Journal of Physiology*, no. 269, pp. 286–292, 1995.

[49] J. Rother, H. Nöding, I. Mey, and A. Janshoff, "Atomic force microscopy-based microrheology reveals significant differences in the viscoelastic response between malign and benign cell lines.," *Open biology*, vol. 4, May 2014.

[50] S. Moreno-Flores, R. Benitez, M. D. Vivanco, and J. L. Toca-Herrera, "Stress relaxation microscopy: imaging local stress in cells.," *Journal of biomechanics*, vol. 43, pp. 349–54, Jan. 2010.

[51] S. Moreno-Flores, R. Benitez, M. dM Vivanco, and J. L. Toca-Herrera, "Stress relaxation and creep on living cells with the atomic force microscope: a means to calculate elastic moduli and viscosities of cell components.," *Nanotechnology*, vol. 21, p. 445101, Nov. 2010.

[52] M. Radmacher, J. P. Cleveland, M. Fritz, H. G. Hansma, and P. K. Hansma, "Mapping interaction forces with the atomic force microscope.," *Biophysical journal*, vol. 66, pp. 2159–65, June 1994.

[53] B. Drake, C. B. Prater, A. L. Weisenhorn, S. A. Gould, T. R. Albrecht, C. F. Quate, D. S. Cannell, H. G. Hansma, and P. K. Hansma, "Imaging crystals, polymers, and processes in water with the atomic force microscope," *Science*, vol. 243, pp. 1586–1589, Mar. 1989.

[54] E. Henderson, P. G. Haydon, and D. S. Sakaguchi, "Actin filament dynamics in living glial cells imaged by atomic force microscopy," *Science*, vol. 257, pp. 1944–1946, Sept. 1992.

[55] W. Häberle, J. K. Hörber, F. Ohnesorge, D. P. Smith, and G. Binnig, "In situ investigations of single living cells infected by viruses.," *Ultramicroscopy*, vol. 42-44 (Pt, pp. 1161–7, July 1992.

[56] M. Fritz, M. Radmacher, and H. E. Gaub, "Granula motion and membrane spreading during activation of human platelets imaged by atomic force microscopy.," *Biophysical journal*, vol. 66, pp. 1328–34, May 1994.

[57] P. K. Hansma, J. P. Cleveland, M. Radmacher, D. A. Walters, P. E. Hillner, M. Bezanilla, M. Fritz, D. Vie, H. G. Hansma, C. B. Prater, J. Massie, L. Fukunaga, J. Gurley, and V. Elings, "Tapping mode atomic force microscopy in liquids," *Applied Physics Letters*, vol. 64, no. 13, p. 1738, 1994.

[58] E. L. Florin, V. T. Moy, and H. E. Gaub, "Adhesion forces between individual ligand-receptor pairs," *Science*, vol. 264, pp. 415–417, Apr. 1994.

[59] J. Friedrichs, K. R. Legate, R. Schubert, M. Bharadwaj, C. Werner, D. J. Müller, and M. Benoit, "A practical guide to quantify cell adhesion using single-cell force spectroscopy.," *Methods (San Diego, Calif.)*, vol. 60, pp. 169–78, Apr. 2013.

[60] G. U. Lee, L. A. Chrisey, and R. J. Colton, "Direct measurement of the forces between complementary strands of DNA," *Science*, vol. 266, pp. 771–773, Nov. 1994.

[61] N. J. Tao, S. M. Lindsay, and S. Lees, "Measuring the microelastic properties of biological material," *Biophysical journal*, vol. 63, pp. 1165–9, Oct. 1992.

[62] A. Weisenhorn, M. Khorsandi, S. Kasas, V. Gotzos, and H.-J. Butt, "Deformation and height anomaly of soft surfaces studied with an AFM," *Nanotechnology*, vol. 4, pp. 106–113, 1993.

[63] M. Radmacher, R. Tillmann, and H. Gaub, "Imaging viscoelasticity by force modulation with the atomic force microscope," *Biophysical Journal*, vol. 64, pp. 735–742, Mar. 1993.

[64] R. G. Bailey, R. D. Turner, N. Mullin, N. Clarke, S. J. Foster, and J. K. Hobbs, "The Interplay between Cell Wall Mechanical Properties and the Cell Cycle in Staphylococcus aureus," *Biophysical Journal*, vol. 107, pp. 2538–2545, Jan. 2015.

[65] N. Kodera, D. Yamamoto, R. Ishikawa, and T. Ando, "Video imaging of walking myosin V by high-speed atomic force microscopy.," *Nature*, vol. 468, pp. 72–6, Nov. 2010.

[66] J. Dalous, E. Burghardt, A. Müller-Taubenberger, F. Bruckert, G. Gerisch, and T. Bretschneider, "Reversal of cell polarity and actin-myosin cytoskeleton reorganization under mechanical and chemical stimulation.," *Biophysical journal*, vol. 94, pp. 1063–74, Feb. 2008.

[67] M. Radmacher, M. Fritz, C. Kacher, J. Cleveland, and P. Hansma, "Measuring the viscoelastic properties of human platelets with the atomic force microscope," *Biophysical Journal*, vol. 70, pp. 556–567, Jan. 1996.

[68] C. M. Lo, H. B. Wang, M. Dembo, and Y. L. Wang, "Cell movement is guided by the rigidity of the substrate.," *Biophysical journal*, vol. 79, pp. 144–52, July 2000.

[69] M. Lekka, P. Laidler, D. Gil, J. Lekki, Z. Stachura, and A. Z. Hrynkiewicz, "Elasticity of normal and cancerous human bladder cells studied by scanning force microscopy.," *European biophysics journal : EBJ*, vol. 28, pp. 312–6, Jan. 1999.

[70] J. Straehla, F. T. Limpoco, N. Dolgova, B. Keselowsky, W. Sawyer, and S. Perry, "Nanomechanical Probes of Single Corneal Epithelial Cells: Shear Stress and Elastic Modulus," *Tribology Letters*, vol. 38, no. 2, pp. 107–113, 2010.

[71] A. Simon, T. Cohen-Bouhacina, M. C. Porté, J. P. Aimé, J. Amédée, R. Bareille, and C. Baquey, "Characterization of dynamic cellular adhesion of osteoblasts using atomic force microscopy.," *Cytometry. Part A : the journal of the International Society for Analytical Cytology*, vol. 54, pp. 36–47, July 2003.

[72] S. E. Cross, Y.-S. Jin, J. Rao, and J. K. Gimzewski, "Nanomechanical analysis of cells from cancer patients.," *Nature nanotechnology*, vol. 2, pp. 780–3, Dec. 2007.

[73] E. C. Faria, N. Ma, E. Gazi, P. Gardner, M. Brown, N. W. Clarke, and R. D. Snook, "Measurement of elastic properties of prostate cancer cells using AFM.," *The Analyst*, vol. 133, pp. 1498–500, Nov. 2008.

[74] S. Leporatti, D. Vergara, A. Zacheo, V. Vergaro, G. Maruccio, R. Cingolani, and R. Rinaldi, "Cytomechanical and topological investigation of MCF-7 cells by scanning force microscopy.," *Nanotechnology*, vol. 20, p. 055103, Feb. 2009.

[75] L. Bastatas, D. Martinez-Marin, J. Matthews, J. Hashem, Y. J. Lee, S. Sennoune, S. Filleur, R. Martinez-Zaguilan, and S. Park, "AFM nano-mechanics and calcium dynamics of prostate cancer cells with distinct metastatic potential.," *Biochimica et biophysica acta*, vol. 1820, pp. 1111–20, July 2012.

[76] J. Helenius, C.-P. Heisenberg, H. E. Gaub, and D. J. Muller, "Single-cell force spectroscopy.," *Journal of cell science*, vol. 121, pp. 1785–91, June 2008.

[77] Y. F. Dufrêne, E. Evans, A. Engel, J. Helenius, H. E. Gaub, and D. J. Müller, "Five challenges to bringing single-molecule force spectroscopy into living cells.," *Nature methods*, vol. 8, pp. 123–7, Feb. 2011.

[78] D. L. Holliday and V. Speirs, "Choosing the right cell line for breast cancer research.," *Breast cancer research : BCR*, vol. 13, p. 215, Jan. 2011.

[79] R. Cailleau, M. Olivé, and Q. V. Cruciger, "Long-term human breast carcinoma cell lines of metastatic origin: preliminary characterization.," *In Vitro*, vol. 14, pp. 911–915, 1978.

[80] H. Soule, J. Vazquez, A. Long, S. Albert, and M. Brennan, "A human cell line from a pleural effusion derived from a breast carcinoma.," *National Cancer Institute*, vol. 51, pp. 1409–1413, 1973.

[81] C. K. Osborne, K. Hobbs, and J. M. Trent, "Biological differences among MCF-7 human breast cancer cell lines from different laboratories.," *Breast cancer research and treatment*, vol. 9, pp. 111–21, Jan. 1987.

[82] S. B. Rodan, Y. Imai, M. A. Thiede, G. Wesolowski, D. Thompson, Z. Bar-shavit, S. Shull, K. Mann, and G. A. Rodan, "Characterization of a Human Osteosarcoma Cell Line (Saos-2) with Osteoblastic Properties," *Cancer research*, vol. 47, pp. 4961–4966, 1987.

[83] L. J. Scott, N. W. Clarke, N. J. George, J. H. Shanks, N. G. Testa, and S. H. Lang, "Interactions of human prostatic epithelial cells with bone marrow endothelium: binding and invasion.," *British journal of cancer*, vol. 84, pp. 1417–23, May 2001.

[84] H. X. You, J. M. Lau, S. Zhang, and L. Yu, "Atomic force microscopy imaging of living cells: a preliminary study of the disruptive effect of the cantilever tip on cell morphology.," *Ultramicroscopy*, vol. 82, pp. 297–305, Feb. 2000.

[85] M. Lekka, D. Gil, K. Pogoda, J. Duliska-Litewka, R. Jach, J. Gostek, O. Klymenko, S. Prauzner-Bechcicki, Z. Stachura, J. Wiltowska-Zuber, K. Oko, and P. Laidler, "Cancer cell detection in tissue sections using AFM.," *Archives of biochemistry and biophysics*, vol. 518, pp. 151–6, Feb. 2012.

[86] E. M. Darling, S. Zauscher, J. A. Block, and F. Guilak, "A thin-layer model for viscoelastic, stress-relaxation testing of cells using atomic force microscopy: do cell properties reflect metastatic potential?," *Biophysical journal*, vol. 92, pp. 1784–91, Mar. 2007.

[87] S. Moreno-Flores, R. Benitez, M. dM Vivanco, and J. L. Toca-Herrera, "Stress relaxation and creep on living cells with the atomic force microscope:

a means to calculate elastic moduli and viscosities of cell components.," *Nanotechnology*, vol. 21, p. 445101, Nov. 2010.

[88] R. E. Mahaffy, C. K. Shih, F. C. MacKintosh, and J. Käs, "Scanning probe-based frequency-dependent microrheology of polymer gels and biological cells.," *Physical review letters*, vol. 85, pp. 880–3, July 2000.

[89] R. E. Mahaffy, S. Park, E. Gerde, J. Käs, and C. K. Shih, "Quantitative analysis of the viscoelastic properties of thin regions of fibroblasts using atomic force microscopy.," *Biophysical journal*, vol. 86, pp. 1777–93, Mar. 2004.

[90] H. Schillers, M. Wälte, K. Urbanova, and H. Oberleithner, "Real-time monitoring of cell elasticity reveals oscillating myosin activity.," *Biophysical journal*, vol. 99, pp. 3639–46, Dec. 2010.

[91] O. Klymenko, M. Lekka, and W. M. Kwiatek, "Energy Dissipation in the AFM Elasticity Measurements," *Acta Physica Polonica A*, vol. 115, no. 2, pp. 548–551, 2009.

[92] Y. R. Silberberg, A. E. Pelling, G. E. Yakubov, W. R. Crum, D. J. Hawkes, and M. A. Horton, "Mitochondrial displacements in response to nanomechanical forces.," *Journal of molecular recognition : JMR*, vol. 21, no. 1, pp. 30–6, 2008.

[93] H. Blaser, M. Reichman-Fried, I. Castanon, K. Dumstrei, F. L. Marlow, K. Kawakami, L. Solnica-Krezel, C.-P. Heisenberg, and E. Raz, "Migration of zebrafish primordial germ cells: a role for myosin contraction and cytoplasmic flow.," *Developmental cell*, vol. 11, pp. 613–27, Nov. 2006.

[94] M. Nikkhah, J. S. Strobl, E. M. Schmelz, and M. Agah, "Evaluation of the influence of growth medium composition on cell elasticity.," *Journal of biomechanics*, vol. 44, pp. 762–6, Feb. 2011.

[95] M. J. Jaasma, W. M. Jackson, and T. M. Keaveny, "The effects of morphology, confluency, and phenotype on whole-cell mechanical behavior.," *Annals of biomedical engineering*, vol. 34, pp. 759–68, May 2006.

[96] Y. M. Efremov, A. A. Dokrunova, D. V. Bagrov, K. S. Kudryashova, O. S. Sokolova, and K. V. Shaitan, "The effects of confluency on cell mechanical properties.," *Journal of biomechanics*, vol. 46, pp. 1081–7, Apr. 2013.

[97] R. Kassies, K. O. van der Werf, A. Lenferink, C. N. Hunter, J. D. Olsen, V. Subramaniam, and C. Otto, "Combined AFM and confocal fluorescence microscope for applications in bio-nanotechnology.," *Journal of microscopy*, vol. 217, pp. 109–16, Jan. 2005.

[98] M. Krause, J. te Riet, and K. Wolf, "Probing the compressibility of tumor cell nuclei by combined atomic forceconfocal microscopy," *Physical Biology*, vol. 10, p. 065002, Dec. 2013.

[99] A. K. Croker and A. L. Allan, "Cancer stem cells: implications for the progression and treatment of metastatic disease.," *Journal of cellular and molecular medicine*, vol. 12, pp. 374–90, Apr. 2008.

[100] W. Jelski and M. Szmitkowski, "Alcohol dehydrogenase (ADH) and aldehyde dehydrogenase (ALDH) in the cancer diseases.," *Clinica chimica acta; international journal of clinical chemistry*, vol. 395, pp. 1–5, Sept. 2008.

[101] M. R. Alison, N. J. Guppy, S. M. L. Lim, and L. J. Nicholson, "Finding cancer stem cells: are aldehyde dehydrogenases fit for purpose?," *The Journal of pathology*, vol. 222, pp. 335–44, Dec. 2010.

[102] A. K. Croker, D. Goodale, J. Chu, C. Postenka, B. D. Hedley, D. A. Hess, and A. L. Allan, "High aldehyde dehydrogenase and expression of cancer stem cell markers selects for breast cancer cells with enhanced malignant and metastatic ability.," *Journal of cellular and molecular medicine*, vol. 13, pp. 2236–52, Aug. 2009.

[103] E. Charafe-Jauffret, C. Ginestier, F. Iovino, C. Tarpin, M. Diebel, B. Esterni, G. Houvenaeghel, J.-M. Extra, F. Bertucci, J. Jacquemier, L. Xerri, G. Dontu, G. Stassi, Y. Xiao, S. H. Barsky, D. Birnbaum, P. Viens, and M. S. Wicha, "Aldehyde dehydrogenase 1-positive cancer stem cells mediate metastasis and poor clinical outcome in inflammatory breast cancer.," *Clinical cancer research : an official journal of the American Association for Cancer Research*, vol. 16, pp. 45–55, Jan. 2010.

[104] A. K. Croker and A. L. Allan, "Inhibition of aldehyde dehydrogenase (ALDH) activity reduces chemotherapy and radiation resistance of stem-like ALDHhiCD44 human breast cancer cells.," *Breast cancer research and treatment*, vol. 133, pp. 75–87, May 2012.

[105] C. van den Hoogen, G. van der Horst, H. Cheung, J. T. Buijs, J. M. Lippitt, N. Guzmán-Ramírez, F. C. Hamdy, C. L. Eaton, G. N. Thalmann, M. G. Cecchini, R. C. M. Pelger, and G. van der Pluijm, "High aldehyde dehydrogenase activity identifies tumor-initiating and metastasis-initiating cells in human prostate cancer.," *Cancer research*, vol. 70, pp. 5163–73, June 2010.

[106] S. Nishikawa, M. Konno, A. Hamabe, S. Hasegawa, Y. Kano, K. Ohta, T. Fukusumi, D. Sakai, T. Kudo, N. Haraguchi, T. Satoh, S. Takiguchi, M. Mori, Y. Doki, and H. Ishii, "Aldehyde dehydrogenase high gastric cancer stem cells are resistant to chemotherapy.," *International journal of oncology*, vol. 42, pp. 1437–42, Apr. 2013.

[107] S.-y. Liu and P.-s. Zheng, "High aldehyde dehydrogenase activity identifies cancer stem cells in human cervical cancer:," *Oncotarget*, vol. 4, no. 12, pp. 2462–2475, 2013.

[108] T. J. Mitchison and L. P. Cramer, "Actin-based cell motility and cell locomotion.," *Cell*, vol. 84, pp. 371–9, Mar. 1996.

[109] V. M. Laurent, S. Kasas, A. Yersin, T. E. Schäffer, S. Catsicas, G. Dietler, A. B. Verkhovsky, and J.-J. Meister, "Gradient of rigidity in the lamellipodia of migrating cells revealed by atomic force microscopy.," *Biophysical journal*, vol. 89, pp. 667–75, July 2005.

[110] V. Vasioukhin, C. Bauer, M. Yin, and E. Fuchs, "Directed actin polymerization is the driving force for epithelial cell-cell adhesion.," *Cell*, vol. 100, pp. 209–19, Jan. 2000.

[111] L. H. Cisneros and T. J. Newman, "Quantifying metastatic inefficiency: rare genotypes versus rare dynamics.," *Physical biology*, vol. 11, p. 046003, July 2014.

[112] K. Reeves, J. G. Albon, C. Eaton, and N. Brown, "Breast cancer cell homing to bone in vivo is modulated by zoledronic acid (676.6)," *The FASEB Journal*, vol. 28, Apr. 2014.

[113] A. D. Bershadsky, N. Q. Balaban, and B. Geiger, "Adhesion-dependent cell mechanosensitivity.," *Annual review of cell and developmental biology*, vol. 19, pp. 677–95, Jan. 2003.

[114] P.-H. Puech, K. Poole, D. Knebel, and D. J. Muller, "A new technical approach to quantify cell-cell adhesion forces by AFM.," *Ultramicroscopy*, vol. 106, no. 8-9, pp. 637–44, 2006.

[115] W. Kozlow and T. A. Guise, "Breast cancer metastasis to bone: mechanisms of osteolysis and implications for therapy.," *Journal of mammary gland biology and neoplasia*, vol. 10, pp. 169–80, Apr. 2005.

[116] R. E. Coleman, E. Rathbone, and J. E. Brown, "Management of cancer treatment-induced bone loss," *Nat Rev Rheumatol*, vol. 9, pp. 365–374, June 2013.

[117] R. E. Coleman, "Clinical features of metastatic bone disease and risk of skeletal morbidity.," *Clinical cancer research : an official journal of the American Association for Cancer Research*, vol. 12, pp. 6243s–6249s, Oct. 2006.

[118] R. Coleman, R. de Boer, H. Eidtmann, A. Llombart, N. Davidson, P. Neven, G. von Minckwitz, H. P. Sleeboom, J. Forbes, C. Barrios, A. Frassoldati, I. Campbell, O. Paija, N. Martin, A. Modi, and N. Bundred, "Zoledronic acid (zoledronate) for postmenopausal women with early breast cancer receiving adjuvant letrozole (ZO-FAST study): final 60-month results.," *Annals of oncology : official journal of the European Society for Medical Oncology / ESMO*, vol. 24, pp. 398–405, Feb. 2013.

[119] A. J. Schech, A. A. Kazi, R. A. Gilani, and A. H. Brodie, "Zoledronic acid reverses the epithelial-mesenchymal transition and inhibits self-renewal of breast cancer cells through inactivation of NF-κB.," *Molecular cancer therapeutics*, vol. 12, pp. 1356–66, July 2013.

[120] C.-K. Lee, Y.-M. Wang, L.-S. Huang, and S. Lin, "Atomic force microscopy: determination of unbinding force, off rate and energy barrier for protein-ligand interaction.," *Micron (Oxford, England : 1993)*, vol. 38, pp. 446–61, Jan. 2007.

[121] X. Zhang, E. P. Wojcikiewicz, and V. T. Moy, "Dynamic adhesion of T lymphocytes to endothelial cells revealed by atomic force microscopy.," *Experimental biology and medicine (Maywood, N.J.)*, vol. 231, pp. 1306–12, Sept. 2006.

[122] M. Tulla, J. Helenius, J. Jokinen, A. Taubenberger, D. J. Müller, and J. Heino, "TPA primes alpha2beta1 integrins for cell adhesion.," *FEBS letters*, vol. 582, pp. 3520–4, Oct. 2008.

[123] R. Omidvar, M. Tafazzoli-Shadpour, M. A. Shokrgozar, and M. Rostami, "Atomic force microscope-based single cell force spectroscopy of breast cancer cell lines: An approach for evaluating cellular invasion.," *Journal of biomechanics*, pp. 1–7, Aug. 2014.

[124] A. G. Végh, C. Fazakas, K. Nagy, I. Wilhelm, J. Molnár, I. A. Krizbai, Z. Szegletes, and G. Váró, "Adhesion and stress relaxation forces between melanoma and cerebral endothelial cells.," *European biophysics journal : EBJ*, vol. 41, pp. 139–45, Feb. 2012.

[125] K. J. Reeves, J. Hou, S. E. Higham, Z. Sun, J. P. Trzeciakowski, G. A. Meininger, and N. J. Brown, "Selective measurement and manipulation of adhesion forces between cancer cells and bone marrow endothelial cells using atomic force microscopy," *Nanomedicine*, vol. 8, pp. 921–934, Dec. 2012.